2-3-2014

Electronic Structure Characterization of Hybrid Materials

Zhi Li
University of South Florida, zhili@mail.usf.edu

Electronic Structure Characterization of Hybrid Materials

by

Zhi Li

A dissertation submitted in partial fulfillment
of the requirements of the degree of
Doctor of Philosophy
Department of Electrical Engineering
College of Engineering
University of South Florida

Major Professor: Rudy Schlaf, Ph.D.
Arash Takshi, Ph.D.
Matthias Batzill, Ph.D.
Jing Wang, Ph.D.
Wenjun Cai, Ph.D.

Date of Approval:
February 3, 2014

Keywords: photoemission spectroscopy, electrospray,
charge injection barrier, work function, dipole

DEDICATION

This dissertation is dedicated to my beloved wife Jie Li, and my parents, who supported me through the entire period. Thank you for all you have done and sacrificed for me. Without your unconditional encouragement, support and love, I could not finish this dissertation.

ACKNOWLEDGMENTS

First and foremost, I would like to thank Dr. Rudy Schlaf for his guidance and support throughout my entire PhD period. I appreciate his kind and professional commitment in supervising.

I also would like to express gratitude to my supervisory committee for their help and advice on how to improve my work.

Furthermore, I would like to thank Dr. Luscombe and her students at University of Washington for providing me the materials I need in my dissertation and valuable research involvements.

Last but not the least, I would like to thank all the members of the Surface Science Lab at University of South Florida for their help.

TABLE OF CONTENTS

LIST OF FIGURES

ABSTRACT

In this dissertation, the studies aim to characterize the electronic structure at the internal interface of hybrid materials. The characterization challenge is originating from the spectral superposition of hybrid constituents. A characterization protocol based on photoemission spectroscopy (PES) was developed and applied to investigate the orbital alignment at the internal interface of the oligothiophene-TiO_2 and ArS-CdSe hybrid materials by characterizing the individual constituents and the assembly hybrids respectively. Electrospray deposition technique was used to deposit targeting materials which enabled preparation of thin films in vacuum minimizing ambient contaminations while transmission electron microscopy (TEM) was used to investigate the morphology and the particle size of the pure nanoparticles and the hybrids. Ultraviolet-visible (UV-vis) spectroscopy was also used in the estimation of the optical band gap of the pure nanoparticles and the HOMO-LUMO gap of the organic ligands.

One of the hybrid materials studied in this dissertation is oligothiophene-TiO_2 nanoparticle hybrids in which the oligothiophene ligands are bonded to the surface of TiO_2 nanoparticles covalently. This hybrid system was used to develop and demonstrate a measurement protocol to characterize the orbital alignment at the internal interface. Low intensity X-ray photoemission spectroscopy (LIXPS) was used to determine the work function of the oligothiophene ligands and the TiO_2 nanoparticles. In combination with the highest occupied molecular orbital (HOMO) cutoff and the valence band maximum (VBM) measured by ultraviolet photoemission spectroscopy (UPS), the ionization energies (IE) of these two

constituents were determined. X-ray photoemission spectroscopy (XPS) was used to characterize the core level emissions of the constituents and the hybrid assembly, which were used to determine the charge injection barriers at the internal interface.

The results showed that there was an interface dipole at the internal interface between organic and inorganic constituents of the hybrid. The dipole was determined to be 0.61 eV and the hole injection barrier at the internal interface amounted to 0.73 eV. The electron injection barrier was estimated by taking into account the gap between highest occupied and lowest unoccupied molecular orbitals (HOMO, LUMO). The procedure followed only suggested the presence of an insignificant barrier in the oligothiophene-TiO_2 nanoparticle hybrids.

Arylthiol functionalized Cadmium Selenide (ArS-CdSe) is a novel hybrid material which can be used in hetero-junction solar cells. The ArSH ligands are bonded on the surface of the CdSe nanoparticles covalently through sulfur atoms serving as anchors. The internal interface in the ArS-CdSe hybrids between the organic constituent and the inorganic constituent was studied by the same characterization protocol developed in this dissertation. Furthermore, a physisorbed interface between the ArSH ligands and the CdSe nanoparticles was created through multi-step in-vacuum deposition procedure. The electrospray deposition technique enabled the formation of a well-defined physisorbed interface which was characterized by LIXPS, UPS and XPS for each deposition step. Accordingly, the orbital alignment at the physisorbed interface was determined.

Based on the results obtained, detailed orbital alignments at the ArSH/CdSe physisorbed interface and the internal interface in the ArS-CdSe hybrid materials were delineated and discussed. The hole injection and electron injection barrier at the physisorbed ArSH/CdSe interface are 0.7 eV and 1.0 eV respectively. An interface dipole of 0.4 eV was observed at the interface. In the ArS-CdSe hybrid materials, the electronic system of the ArSH component shifts

down due to the charge transfer induced by the covalent hybridization. The hybridization also shifts the electronic system of the CdSe constituent to a lower energy level due to saturation of the unoccupied bonds of the Cd atoms on the surface. The hole injection barrier and electron injection barrier were determined to be 0.5 eV and 1.2 eV respectively. A small interface dipole (0.2 eV) was observed at the internal interface as a result of the presence of covalent bonds.

CHAPTER 1: MOTIVATION AND INTRODUCTION

1.1: Motivation and Outline of this Dissertation

Due to the current rising concerns regarding environmental hazards associated with the massive use of fossil fuels, there has been a great shift toward developing alternative environmentally sustainable sources of energy [1]. Back in 1959 when Richard Feynman declared the tremendous potential of nanotechnology with his famous statement that "There's plenty of Room at the Bottom", revolutionary developments in nano-scale technology have brought about dramatic changes to every aspect of the human life [2]. The use of nano-scale technology has been more dominant in the field of energy where nanotechnology offers better tools that can be used in the development of new environmentally friendly energy generation solutions such as solar economy, hydrogen economy and sustainable electricity storage [3]. In the core of nanotechnology, materials with nano-scale dimensions are an intriguing essence due to their novelty and enhanced properties compared to traditional materials [4, 5]. Nano-scale materials differ from traditional materials not only in terms of their characteristic scale, but also in regard to their new physical properties which offer new possibilities that can be realize various technological applications.

In the field of photovoltaic devices, nano-materials are increasingly attractive due to their tunable band gap which can be achieved through size adjustment as well as their excellent carrier transportation ability and solution processable fabrication [6-8]. Photovoltaic process converts sunlight directly into electricity by absorbing solar energies which match the optical band gap of

the materials. The basic design principle is to use materials with suitable optical band gap enhancing the light absorption as well as to create an interface with desirable charge injection barriers. TiO_2 nanoparticles with a wide band gap are used in the application of dye-sensitized solar cells in which organic molecules act as redox dyes. Such devices have achieved acceptable high power conversion efficiency of above 12% [9]. CdSe nanoparticles are another attractive nanomaterial with high carrier mobility and suitable band gap that can be applied in the field of photovoltaic devices [10]. In particular, the properties of CdSe nano-materials can be refined during the procedure of synthesis by adjusting their size and shape [11]. By mixing CdSe nanoparticles with low band gap polymer, bulk-hetero-junction solar cells can be fabricated with solution-based roll-to-roll process [12].

In the photovoltaic process of converting absorbed sunlight into electricity, *Frenkel excitons* with large binding energies (0.4 to 1.0 eV) and short diffusion lengths (5 to 20 nm) are generated in organic/nanoparticle based solar cells [13, 14]. The key of dissociating excitons into free charges is to create a hetero-junction with suitable energy band offsets and an environment that allows fast diffusion of excitons to the interface [15, 16]. Further advanced research on nano-materials focuses on the development of more complex molecular structures. In these structures, the core nano-material is capped with an outer organic layer which serves multiple functional purposes in order to break a longstanding bottle neck on the path of achieving higher power conversion efficiency [17, 18]. A novel hybrid nanomaterial which consists of two or more covalently-linked and electronically-coupled semiconductor components is developed to fully utilize the advantages brought by the both constituents. Figure 1 shows the schematic of a proposed hybrid structure in which the inorganic nanoparticle is bonded with organic ligand through covalent bonds.

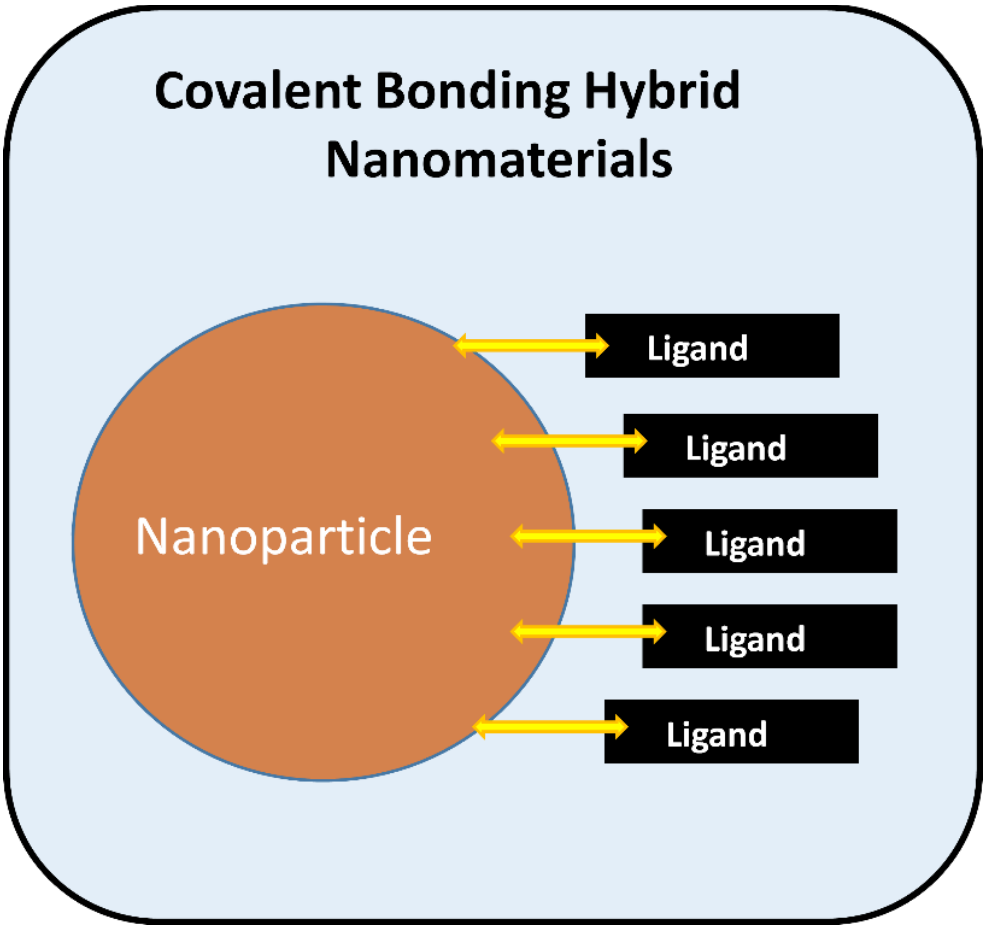

Figure 1: Schematic of a hybrid structure. The hetero-junction interface is realized through covalent bonds. The inorganic nanoparticle can be various semiconductor nanoparticles with desired properties. The organic constituent is not limited to small molecules. Polymers with a lower band gap and better charge mobility are ideal for the hybrid structure.

The surface and internal interface properties of hybrid nano-materials are essential for the device performance. To determine and understand the orbital alignment in the hybrid materials makes great contributions in the development of the novel hybrid materials with desired electronic properties. Photoemission spectroscopy (PES) is a powerful and popular tool to characterize the surface and interface properties [19, 20]. Low intensity x-ray photoemission spectroscopy (LIXPS) uses low photon flux to measure secondary electrons which can provide

valuable information of sample work function. X-ray photoemission spectroscopy (XPS) probes the deep core-level emission features from which valuable information about chemical interaction can be extracted. Ultraviolet photoemission spectroscopy (UPS) measures the density of states in valence bands (VB)/ highest occupied molecular orbitals (HOMO) of the targeting sample directly [21, 22]. In combination of PES measurements with in-vacuum electrospray deposition technique, the surface and interface characterization of hybrid nano-materials can be achieved.

This dissertation focuses on the development of a PES based characterization protocol to measure the internal orbital alignment of hybrid nano-materials. The first part of the dissertation addresses the challenge with hybrid internal interface characterization due to the bonded parts in hybrid materials cannot be deposited individually resulting in a superimposed spectrum of both densities of state. A sequence of experiments is meticulously designed to obtain electronic information from individual parts and the bonded hybrid assembly.

The second part of this dissertation applies the developed characterization protocol to different hybrid materials. The first hybrid system studied is oligothiophene-TiO_2 hybrid materials in which the oligothiophene ligands are bonded to the surface of TiO_2 nanoparticles covalently using carboxyl groups as anchors. Experimental data with regarding to the electronic structure of oligothiophene ligands, TiO_2 nanoparticles and oligothiophene-TiO_2 hybrids were collected and used to characterize the internal orbital alignment in hybrids. The second hybrid material is ArS-CdSe hybrid materials in which the organic ArSH ligands are bonded with CdSe nanoparticles through sulfur atoms covalently. By applying the same protocol, the internal orbital alignment of ArCdSe hybrids was determined and discussed. Furthermore, a physisorbed

interface between the ArSH ligands and the CdSe nanoparticles were created via multi-step in-vacuum deposition and characterized to compare with the internal interface.

1.2: Properties of Semiconductor Nanoparticles

In the early 1980s, semiconductor particles with sizes in nano-scale have received much attention. The material system relies on the transition regime from the bulk solid to molecules. It is a fascinating material system for researching and studying novel properties which are attributed to size-quantization effect. Atomic orbitals are well known fingerprints of atoms. For a single atom the orbital energies are attributed to the ground-state electron configuration. Figure 2 shows the evolution of the electronic structure from an atom to bulk materials. The density of states (DOS) within a band is typically related to the number of atoms. The combination of several atoms creates small molecules in which the anti-bonding and bonding states are related to orbital electron spinning. In a molecule electron orbitals are shared between atoms. However, only the lowest energy levels are occupied. The electronic structure of nanoparticles strongly depends on the size and shape due to the quantum confinement effects. The confinement arises as a result of changes density of states. For a free particle or a particle in bulk semiconductor material, both of the energy and momentum can be precisely defined and determined. However, for a defined particle in nano-scale, only the energy may still be well defined. Since the momentum cannot be well defined, the superposition of momentum states gives rise to a compression of energy states by quantum confinement [23].

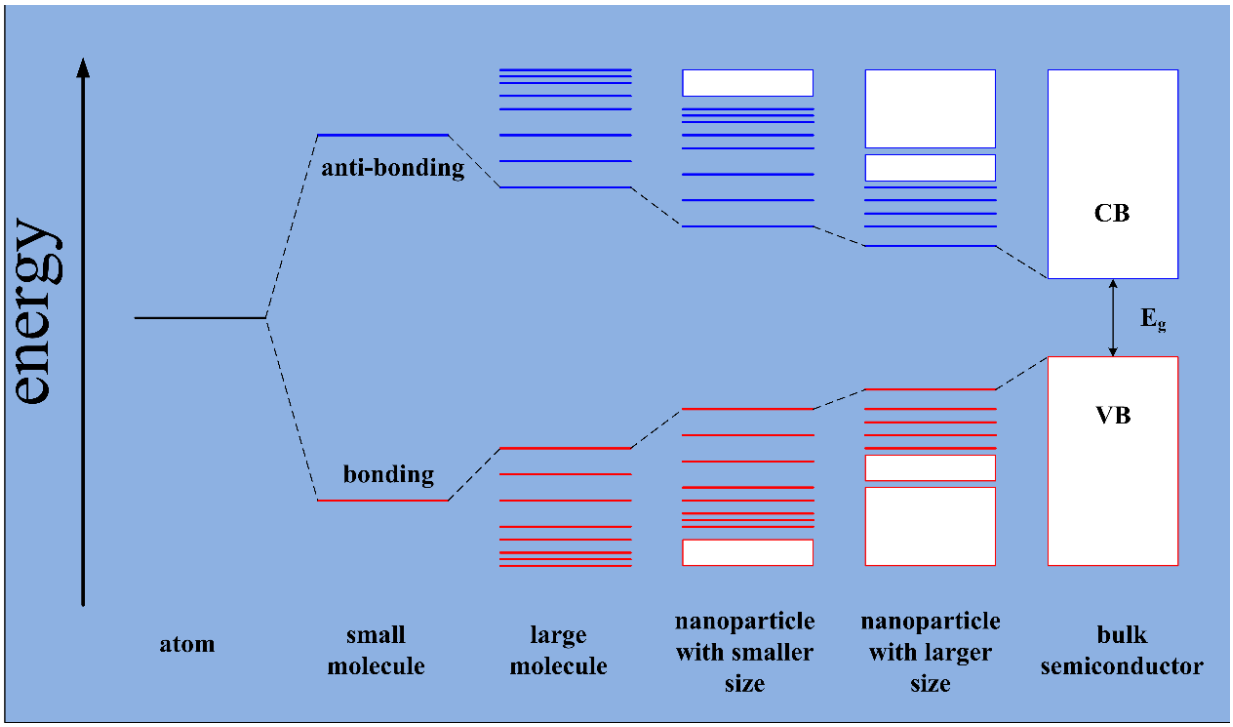

Figure 2: Evolution of the electronic structure from a single atom to bulk semiconductor. As for a single atom, the electrons stay at confined orbitals. With the increase of atom number, the discrete band structure becomes continued. The band gap energy decreases from nano-materials to bulk materials.

An electron excited from valence bands by absorbing a photon with quantized energy moves to conduction bands and a hole is left behind. The electron-hole pairs are still confined by attractive Coulomb forces resulting in the formation of *Wannier excitons*. The paired exciton system can be described by a two-particle Hamiltonian since it is similar as a hydrogen atom. The diameter of the *Wannier excitons* depends on the effective masses of electrons and holes as well was the high-frequency dielectric constant, as shown in Equation (1).

$$d = \frac{\hbar^2 \varepsilon}{e^2} \left[\frac{1}{m_e^*} + \frac{1}{m_h^*} \right] \quad (1)$$

However, as for a nanoparticle, the particle diameter is comparable to the diameter of the exciton in bulk material. As a result, the continuous band structure is split into discrete levels as illustrated in Figure 2. It shows that with decreasing particle size the energy of the lowest excited state, which is known as conduction bands minimum, increases resulting in the increase of band gap. Thus, the major consequence of the quantum confinement effect on semiconductor nanoparticles is the particle size dependence of the band gap. The band gap increases as the particle size decreases while the energy states are quantized. The size dependence has been demonstrated by the dramatic color change of the CdSe colloidal solutions with different particle sizes, shown in Figure 3.

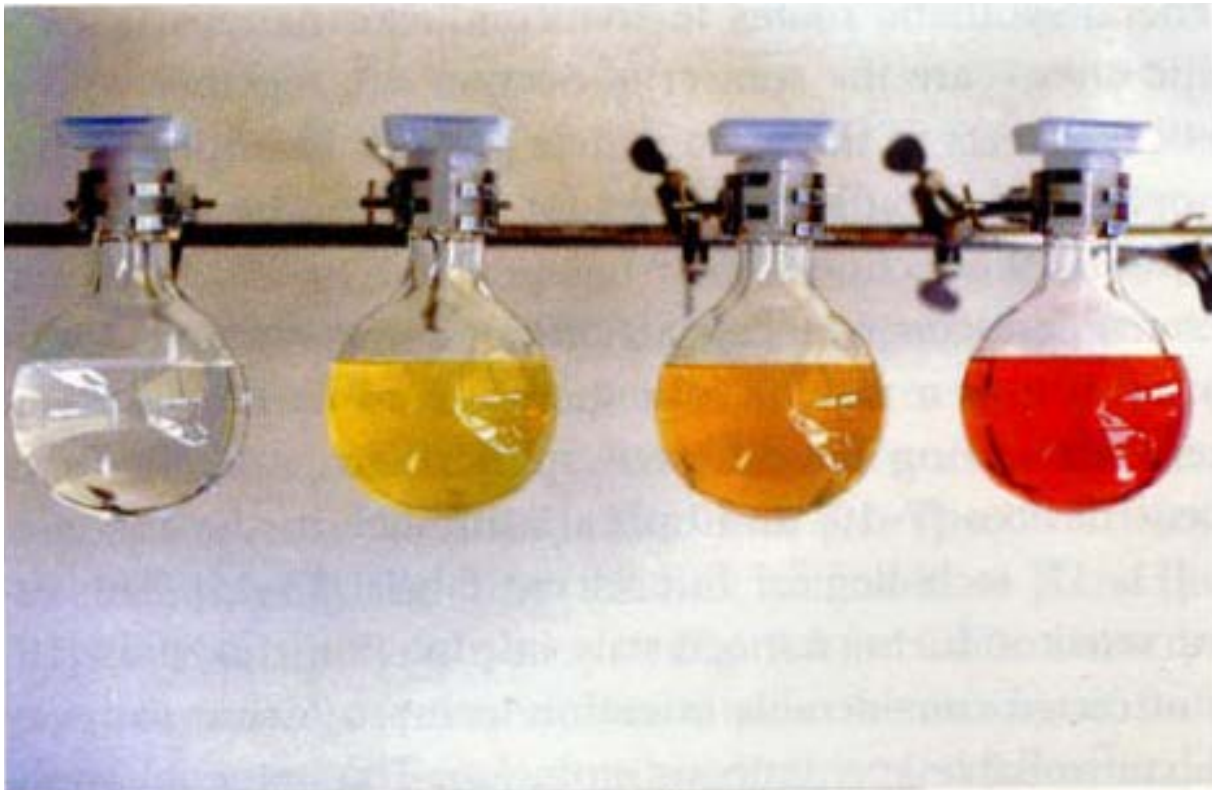

Figure 3: Experimental demonstration of the band gap dependence on the particle size. The CdSe nanoparticle size changes 1.5 to 4.5 nm from left to right [24].

Besides the phenomenal orbital structures, large surface area to volume ratio is another key property of nanoparticles. In bulk materials, atoms on the surface only represent a negligible fraction of the total number of atoms. Nevertheless, with the decrease of particle size, the ratio of the surface atom number to the total number increases dramatically. The large surface area to volume ratio has significant effects on the properties of nanoparticles in isolation as well as the interaction with other materials. It is a crucial factor in the performance of catalysis and electrodes whose improvements are directly related to the technology development [25, 26]. The large ratio also enhances the interaction in intermixed nanocomposites, leading improved strength and chemical/heat resistivity [27, 28]. The high surface area to volume ratio can be crucial to in dye-sensitized solar cells and nanoparticle/organic hybrid solar cells since a large interfacial contact area facilitates the charge separation and transportation [29, 30].

1.3: Organic/Inorganic Hybrid Solar Cells

Solar energy is a clean, abundant and renewable energy source which can be converted into electricity by photovoltaic devices. For conventional solar cells, the efficiency has climaxed up to 44.7% through the use of expensive materials and complex stacking technology. In order to fabricate large scale and low cost solar cells, new technologies are required. To date, a broad range of photovoltaic technologies is in development, such as dye-sensitized solar cells, polymer/fullerene bulk hetero-junction solar cells, small molecule thin films solar cells, organic/inorganic hybrid solar cells, et al. [31-34].

Hybrid solar cells are generally a mixture of both organic and inorganic materials. Therefore, the unique properties of inorganic semiconductor nanoparticles and the properties of organic materials are combined in such devices. Organic-inorganic hybrid solar cells which are based upon physically blending conjugated polymer and nanoparticles have attracted a lot of

attention [33]. The basis of such solar cells is the bulk hetero-junction concept. These hybrid active layers have combined the advantages from nanoparticles and conjugated polymers, such as tunable band gap, large surface to volume ratio, excellent charge carrier mobility, solution processability and good environmental stability [35-37]. Physically blending organic polymers with inorganic nanoparticles is a simple fabrication process. However, the physisorbed interface impedes the charge separation and transportation due to the incompatible organic/inorganic interface, the insulating capping ligands and small interfacial area [38, 39].

Basically, a solar cell is a device which can convert solar energy into electricity by absorbing photons. For a conventional inorganic semiconductor based solar cell, electrons in the valence band (VB) are excited up to the conduction band (CB) when the energy of incident photons is matching to the band structure for absorption [40, 41]. The photon generated free electrons and holes will diffuse to the corresponding collection electrodes resulting a photocurrent which can be used as energy source. However, in an organic-inorganic materials based hybrid solar cell, an incident photon will generate an exciton which is an electron-hole pair bound by strong Coulomb force, as shown in Figure 4. The typical binding energy of this electron-hole pair is ~0.1-0.5 eV which is larger than the thermal energy. Thus, the photon generated excitons cannot be dissociated in the absorbing layer. The excitons have to diffuse to the donor-acceptor interface at which the energy offset between the organic donor LUMO and the inorganic acceptor conduction band minimum can dissociate excitons into free charges [42]. These free charges are then transported within the materials and collected by corresponding electrodes. The state-of-the-art in this hybrid solar cell is that excitons can also be generated in the inorganic acceptor. The excitons generated in the inorganic acceptor which is nanoparticles in this dissertation are bound by Coulomb force as well [43, 44]. The dissociation of these

excitons also requires higher energy than thermal energies. In order to get free charge carriers, these excitons have to rely on the band energy offset at the interface.

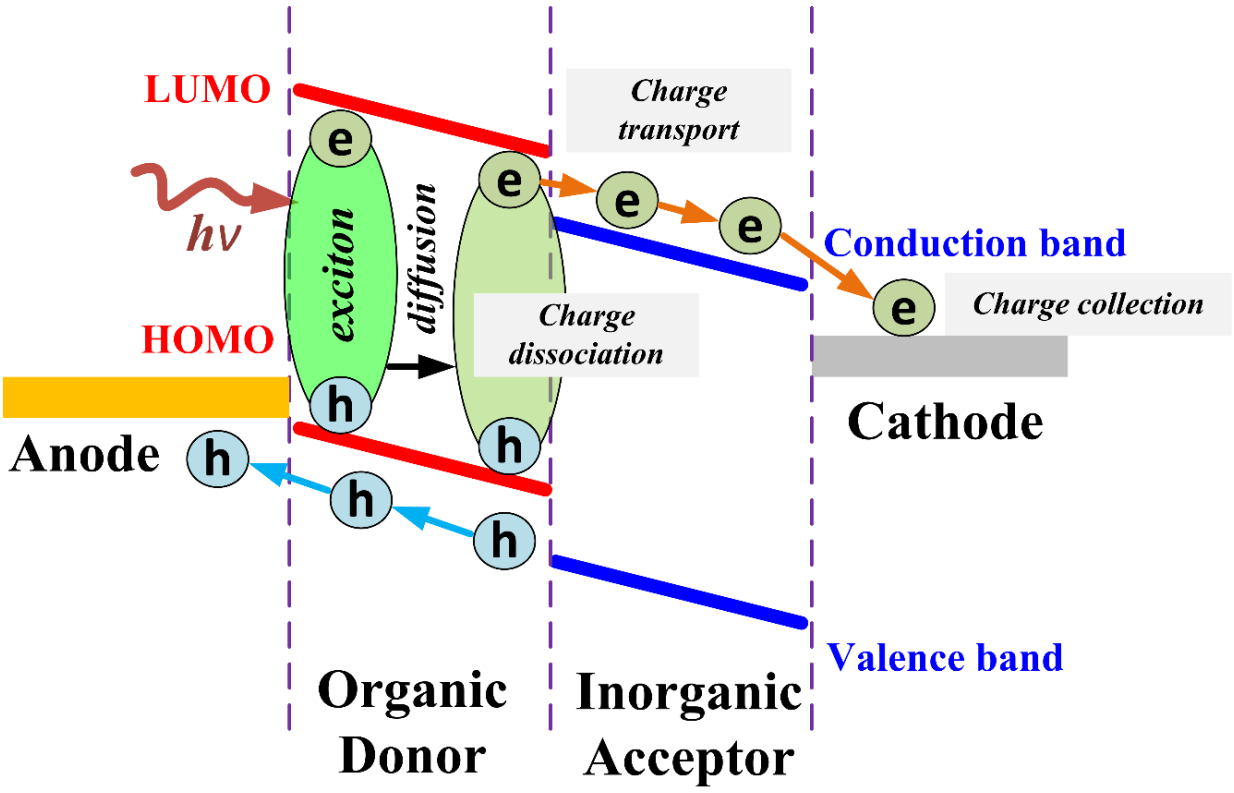

Figure 4: Schematic demonstration of the working mechanism of hybrid solar cells with organic materials as donors and inorganic materials as acceptors.

The advantages of hybrid strategy are significant and related to the combined properties of inorganic and organic materials. The inorganic acceptors can have high absorption coefficients which enable the light absorption of both parties. Within the synthesis process, the doping level of nanoparticles can be changed easily so that the charge transfer between donors and acceptors can be studied systematically. The band gap in inorganic nanoparticles can be tuned easily through size modification, realizing novel tandem architectures in which same

materials with different band gaps can be obtained. Furthermore, the large surface to volume ratio of inorganic nanoparticles provides a substantial interfacial area for exciton-dissociation and charge-transfer.

The power conversion efficiency of hybrid solar cells strongly depends on orbital alignments of the donor and acceptor at the interface. Many efforts have been made to control the film morphology and interfacial area [45, 46]. However, simply be physically blending donors and acceptors makes challenges to achieve efficient charge dissociation and transportation. In this perspective, a promising strategy is to realize covalent contacts between donors and acceptors to reduce the diffusion length of excitons and creating larger interfacial area.

1.4: Orbital Alignment at Semiconductor Interfaces

The main objective and focus of this dissertation is to determine of the internal orbital alignment in hybrid materials. The electronic structure of semiconductors can be illustrated in band diagrams. Figure 5 (A) shows a typical band structure of a n-type semiconductor i.e., the Fermi level is close to the conduction band due to the excessive of electrons. The work function Ψ is defined as the energy difference between the Fermi level and vacuum level i.e., the minimum energy required to remove an electron from the solid surface [47]. The valence band maximum (VBM) or highest occupied molecular orbital (HOMO) cutoff refers to the energy difference from the Fermi level to $E_{VB/HOMO}$.

As in a metal, all energy states are filled with electrons up to the Fermi level. In comparison to metals, semiconductors are defined by their unique band structure. The band structure is associated with the quantum states of electrons. Therefore, the work function of semiconductors is not the same as the electron affinity (χ) in metals which is the energy

difference between the conduction band minimum and vacuum level. For a semiconductor, the ionization energy is the energy difference between the valence band maximum and vacuum level. The semiconductors can be doped to adjust the conductivity and band structure. Meanwhile the electronic structure at the surface is different as it in the bulk. A great amount of defects are on the surface of semiconductors. The resulted surface states can change the orbital alignment on the surface dramatically. Thus it is crucial to understand and investigate the surface state of semiconductors.

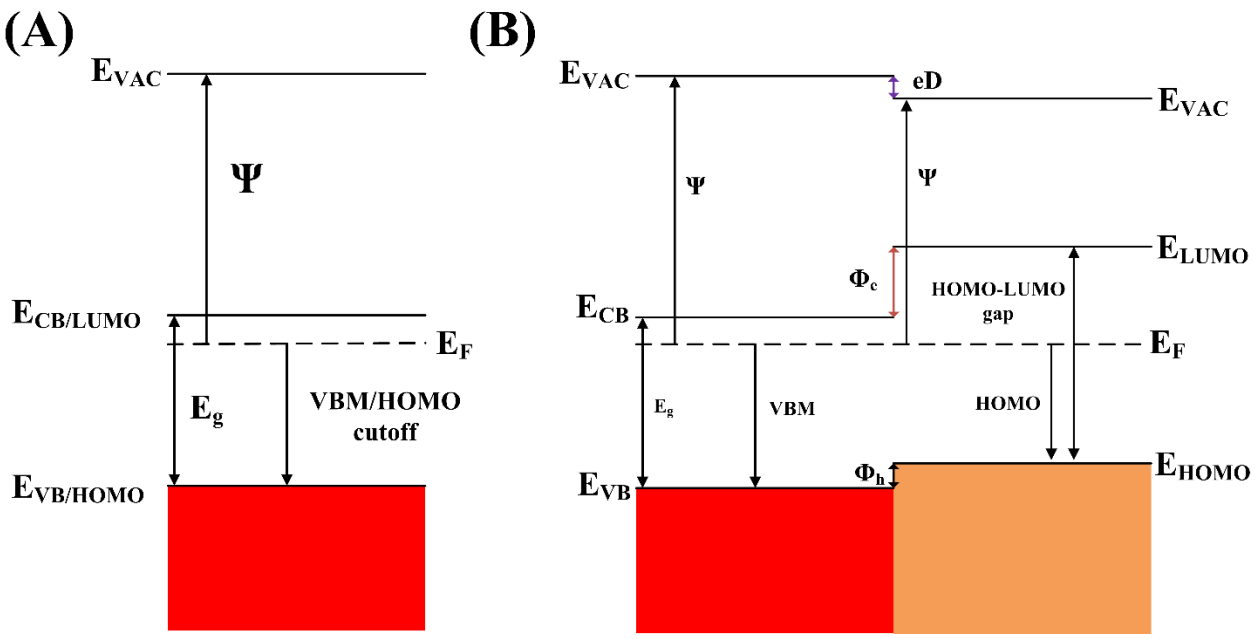

Figure 5: Semiconductor electronic structure, (A) a typical band structure, (B) orbital alignment at semiconductor interface.

When two different semiconductors make contact, a hetero-junction will be formed resulting in an orbital realignment at the interface according to the different electron affinity. The orbital alignment at a hetero-junction interface can be illustrated in Figure 5 (B). The first band alignment model was developed by Schottky to describe band offsets at the interface between

metals and semiconductors [48]. Then this model was developed and extended by Anderson to describe hetero-interfaces between semiconductors in 1962 [49]. Typically the orbital alignment at hetero-junction interfaces depends on the alignment of vacuum level. As the alignment of vacuum levels, bands offsets i.e., charge injection barriers are formed at hetero interfaces. When an electron is excited from the valence band into the conduction band, this electron can move freely in the conduction band. Thus the band offset between two conduction bands refers to the electron injection barrier shown as Φ_e in Figure 5 (B). The valence band offset is termed as the hole injection barrier (Φ_e) to describe the energy needed for holes to overcome during the transportation. However, the Anderson model explains band offsets from the viewpoint of bulk properties of semiconductors. It fails to consider the surface states and physico-chemical phenomena at the interface due to the chemical environment changes. In experimental studies, an interface dipole (eD) is usually observed as a result of charge transfer at the interface [50, 51]. Thus, neither the Schottky model nor the Anderson model can be applied to describe hetero interfaces because interface dipoles are not considered in these models.

At semiconductor hetero interfaces, thermal equilibrium is achieved through charge transfer due to the different work function. When many surface states are concentrated within the band gap, the Fermi level is required to be equalized i.e. Fermi level pinning happens cross the interface [52]. As a result of Fermi level pinning, energy states out of band gap give rise to an interface dipole as an offset at vacuum level. Accordingly, the orbital alignment based on this concept is illustrated in Figure 5 (B) taking the interface dipole into account as a consequence of Fermi level pinning effects.

Specifically, the orbital alignment at organic/inorganic interfaces do not follow the Anderson model due to the physico-chemical interaction at the interface which results in the

formation of interface dipoles. As for organic-inorganic hybrid materials, the covalent bonds which connect organic molecules to inorganic materials have non negligible influences on the orbital alignment. However, such influences are still unclear due to the characterization challenge. In this dissertation, the orbital alignment at the organic/inorganic interface is presented with examples of oligothiophene/TiO_2 and ArSH/CdSe hybrid materials to study the influence of hybridization through covalent reactions.

CHAPTER 2: EXPERIMENTAL METHODOLOGY

The samples used in the study that this dissertation is based on were prepared by *in situ* electrospray deposition technique. This technique enables direct deposition of various molecules onto a substrate in the vacuum chamber minimizing ambient contaminations while maintaining complete chemical structures. The details of this deposition technique will be discussed in this chapter. Sputter cleaned Au slides and highly ordered pyrolytic graphite (HOPG) were used as sample substrates. The Au substrate was sputter cleaned in a preparation chamber before transferred into the deposition chamber. The HOPG substrates were prepared in a home-made glove box which was connected with the main analysis chamber. The electronic structure of the targeting sample was characterized with photoemission spectroscopy (PES). Thus, theories and setup of PES measurements including X-ray photoemission spectroscopy (XPS) and ultra-violet photoemission spectroscopy (UPS) will be introduced in this chapter in details.

2.1: Electrospray Deposition Technique

The newly developed applications based on macromolecular materials require suitable and indestructible film deposition techniques. Typically, these materials can be deposited using spin-coating, dip-coating and ink-jet printing techniques [29, 53, 54]. The advantage of these techniques is that they can be performed easily in ambient atmosphere. However, the disadvantage of these techniques is also obvious. Exposing contaminations from ambient atmosphere can induce unknown factors to surface characterizations and device performances. Molecule evaporation is a deposition technique which can be used to deposit macromolecules in

vacuum. However, it requires high temperature to be applied in order to evaporate macromolecules from solid phase to gas phase. Since macromolecules can be easily dissociated under high temperature, it is not an ideal way to deposit macromolecule thin films [55]. Therefore, a deposition method which can make macromolecules deposition directly in vacuum without any contaminations and damages is needed.

A solution to this challenge relies on electrospray deposition technique which enables the indestructible deposition of various materials from solution into vacuum. Conjugated polymers, nanoparticles, biomolecules, living cells and other macromolecules have been deposited successfully by this technique [56-61]. In this indestructible deposition method, the solution containing the targeted material is injected from a capillary. A high voltage is used to nebulize and ionize the aerosol phase solution which is further drawn into a vacuum chamber through a tunnel orifice. The targeted material will be deposited onto a prepared clean substrate in the chamber. The entire deposition process is thermal free and avoids ambient contaminations as the best.

The electrospray deposition technique is originated from electrospray ionization mass spectrometry (ESIMS) which was developed by Fenn et al. to characterize large molecules [62]. The molecules are sprayed in their gas phase and ionized in a preset electric field to realize charge separation. This deposition method can be integrated with a multi-chamber photoemission spectroscopy (PES) system as a powerful tool in surface and interface characterization. An *in-situ* material deposition followed by PES measurements enables multi-step investigations on the film while the film thickness can be controlled with a sub-monolayer level [63].

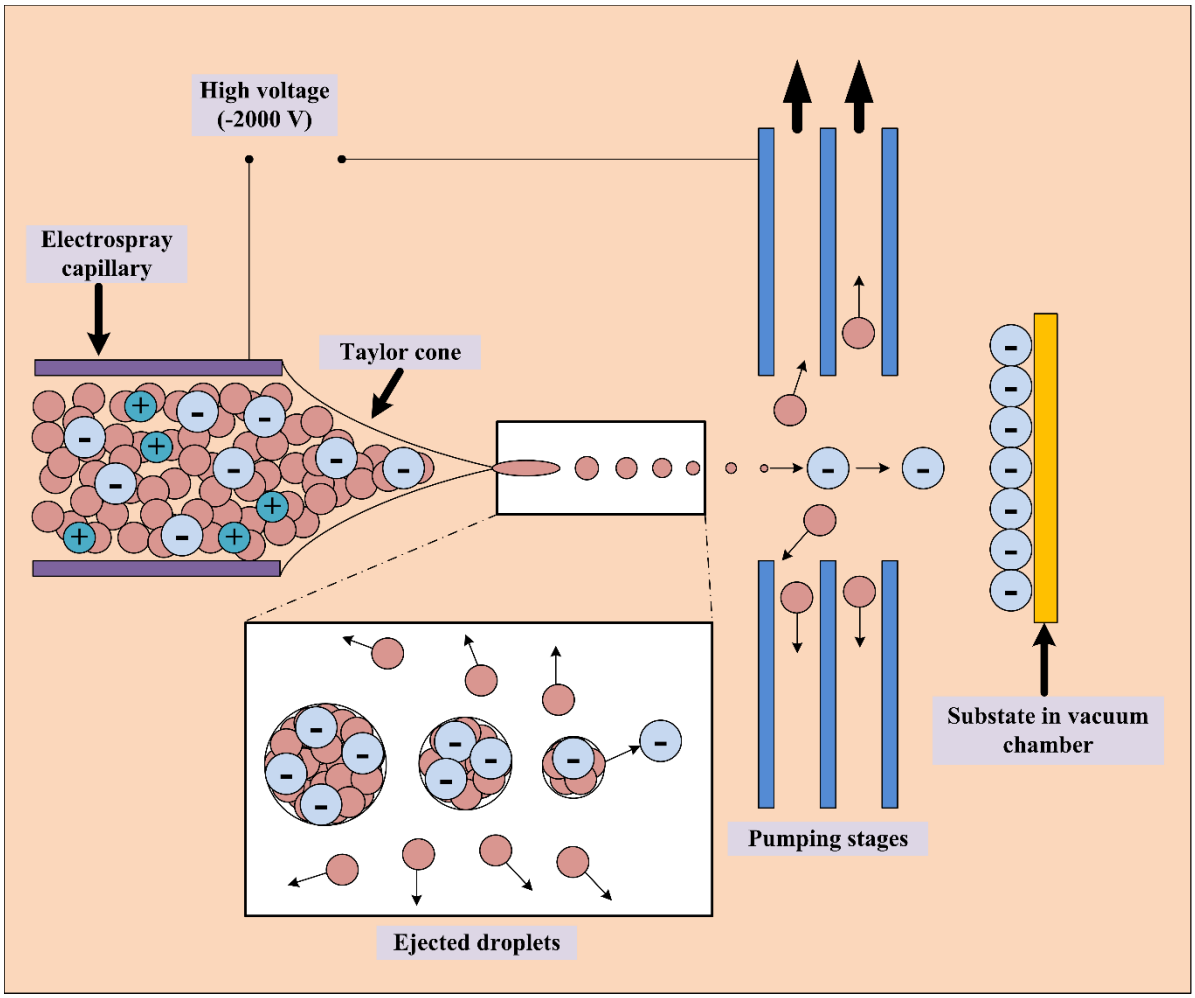

Figure 6: Schematic of the electrospray deposition technique and the mechanism. Ejected droplets are ionized by a high voltage across the capillary and substrate. Solvent molecules are separated from the targeted molecules through coulomb explosions and extracted out of the system by vacuum pumps.

The mechanism of an electrospray deposition process is illustrated in Figure 6. The solution containing targeting materials is prepared with a certain concentration (in mg/mL range) and loaded into a syringe with an injection capillary. The capillary tip is made of stainless iron on which a high voltage is applied to provide required electric field during the deposition. In the experiments presented here, a negative 2000 voltages was applied. The molecules in the solution

are nebulized and ionized in this applied electric field. The generated anions will be accelerated in the field while the cations will be expulsed away after they leave the capillary tip. To be specific, the injected solution forms a Taylor-cone which will dissociate into a three dimensional plume at the tip of the capillary [64]. The plume consists of small solution droplets which will be extracted from the Taylor-cone and ionized by the applied high potential. An N_2 environment is provided around the orifice to prevent ambient contaminations. After the droplets enter the orifice, solvent molecules will evaporate with assistance from the differential pumping stages during the flight. As the droplets shrink, the charge density will increase to a point where the Coulomb forces can overcome the surface tension. Then Coulomb explosions are induced to further separate the targeted material from the solvent. The substrate in the vacuum chamber is grounded. The potential difference between the capillary tip and the substrate can provide enough electrostatic forces to drive the injected liquids flying towards the substrate. Eventually, a thin film of the targeting material can be formed uniformly.

2.2: Photoemission Spectroscopy

Photoemission spectroscopy (PES) is the main characterization method used in this dissertation. In PES measurements, the occupied states of electrons in a sample are investigated by exposing the sample to a specialized radiation. The incident radiation excites electrons from the ground state to the final state resulting in the generation of photoelectrons which can be captured and analyzed through an analyzer. This characterization technique originates from the photoelectric effect which was first observed by Hertz in 1887 [65]. In 1905, Einstein explained this phenomenon with the famous photoelectric effect theory [66]. In 1950s, a high resolution photoelectron spectrometer was made by Siegbahn and his co-workers [67]. Up to date PES

system has improved resolution below 1 eV and is used as a powerful characterization method in various fields.

2.2.1: The Physical Principle of Photoemission Spectroscopy

Different radiation sources, such as a gas-discharge lamp, an X-ray tube or a synchrotron-radiation setup, can be used to generate monochromatic radiation in PES measurements. The incident photons are transported and absorbed by the material to excite electrons into unoccupied states. If the final state of photoelectrons is above the vacuum level, the photoelectrons can be emitted out of the material into vacuum. Einstein's photoelectric equation can be used to describe the kinetic energy E_{kin} of the emitted electrons:

$$E_{kin} = h\nu - E_B - \Phi \tag{2}$$

in which, $h\nu$ is the energy of the incident photon, E_B is the binding energy of the pre-excited electron and Φ is the work function of the material. The energy level of a sample and its corresponding PES spectrum are shown in Figure 7. The energy level of the sample consists of the valence bands and the core levels with characteristic emission features as shown on the bottom left in Figure 7. If the material investigated is a metal, the Fermi level will be located at the same energy level as the valence band onset, indicating that there is no band gap in the electronic structure. The energy difference between the Fermi level and the vacuum level is called work function and termed as Φ which refers to the minimum energy needed to remove electrons from the material surface. As manifesting in the spectrum, the secondary edge originating from secondary electrons which lose kinetic energy during inelastic collisions can be used to calculate the work function. If a photoelectron is excited and emitted from a core level or a valence state without suffering any inelastic collisions, it is called a prime electron and its

kinetic energy E_{kin} can be measured by a spherical electron analyzer. The number of photoelectrons with the same kinetic energy is counted. Then a spectrum can be plotted as the number of photoelectrons vs. various kinetic energies. Typically, both of the prime photoelectrons and the secondary electrons can be seen in the spectrum as shown in Figure 7.

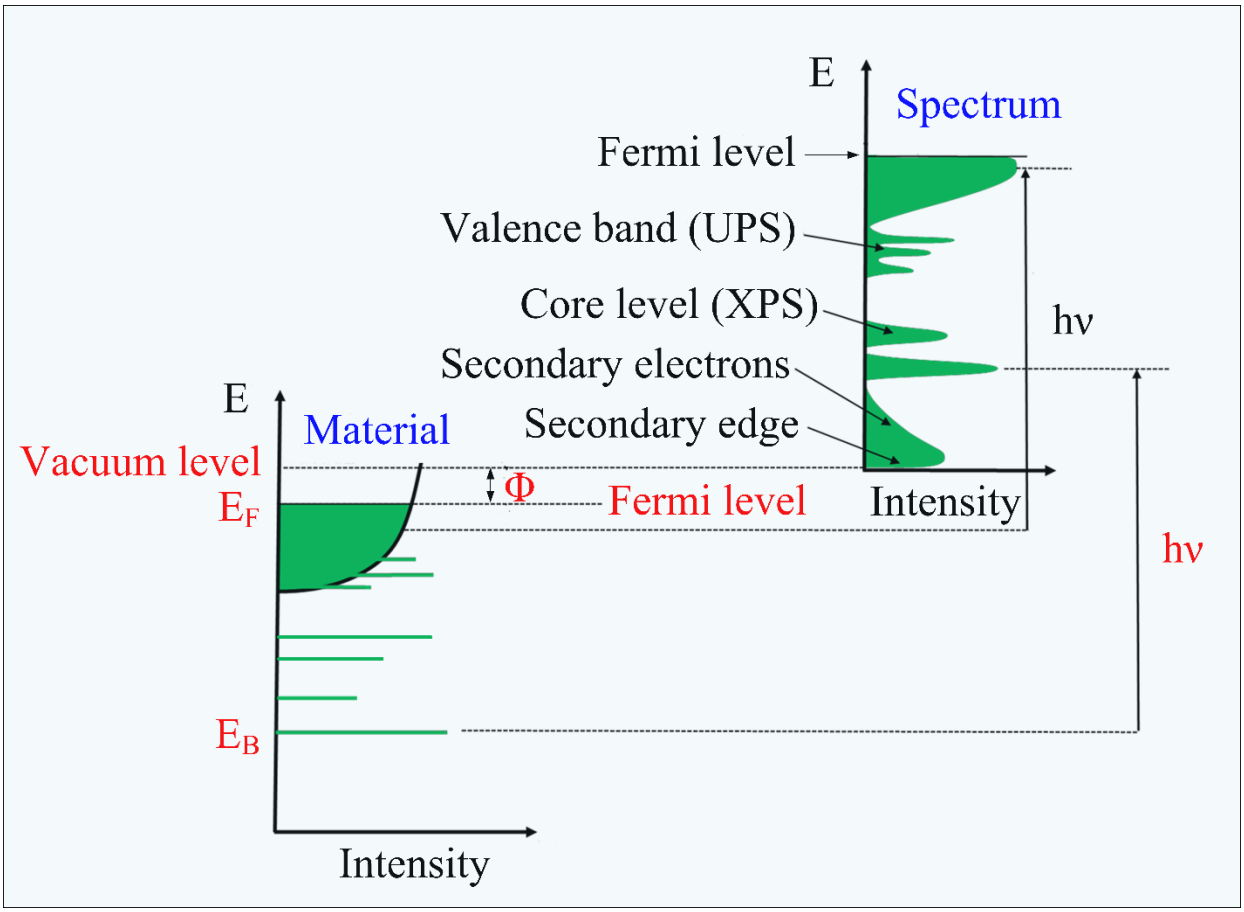

Figure 7: The energy levels of a sample obtained from PES measurements. The relation between the energy of incident photons and the kinetic energy of emitted electrons is illustrated.

The ionization cross section is an important factor in PES measurements because it relates to the possibility of electrons to be excited out of the locating orbital by incident photons. The ionization cross section varies from orbitals and elements and depends on the energy of

incident photons as well [68]. The intensity and noise to signal ratio of a spectrum are strongly depended on the ionization cross section. Therefore, it is important to keep it in mind while performing PES measurements.

The penetration depth of incident photons is in the range of microns and varies from material to material. However, the excited photoelectrons can only travel within a material before their kinetic energy are consumed completely by inelastic collisions with other electrons or nucleus during the travelling. The path for excited electrons without suffering inelastic collisions is defined as an inelastic mean free path λ which is only in the range of angstroms. Figure 8 shows the universal plot of the electron mean free path as a function of the kinetic energy. In the range of 10 to 2000 eV which is the range where PES measurements are carried out, the electron mean free path is only a few Å. This means that PES can only detect the density states from a very thin layer even though the electrons within a thick layer can be excited. It is worthy to mention that the mean free path is material dependent and related to the material bonding structure. Theoretically, the mean free path for different materials can be calculated. But it is mostly determined by empirical experiments. The fact that excited photoelectrons can only travel a few Å without suffering any inelastic collisions makes PES a powerful characterization method to study surface properties.

Once an electron is excited from its ground state to its final state escaping from the material surface, the neutral atom turns to be ionized leaving a photo-generated hole behind. However, the positive charging environment near the left-over nucleus is energetically unfavorable. As a result, the remaining electrons have to be in a relaxed situation in order to screen the positive charges from each other. This is called final state effects. During PES measurements, the photoemission process is slower than the relaxation process in approximately

one magnitude. Therefore, PES measurements are sensitive to final state effects. The recorded PES spectra are characteristics of the excited electrons in their final states in which the polarization energy impacts the binding energy of detected electrons [69].

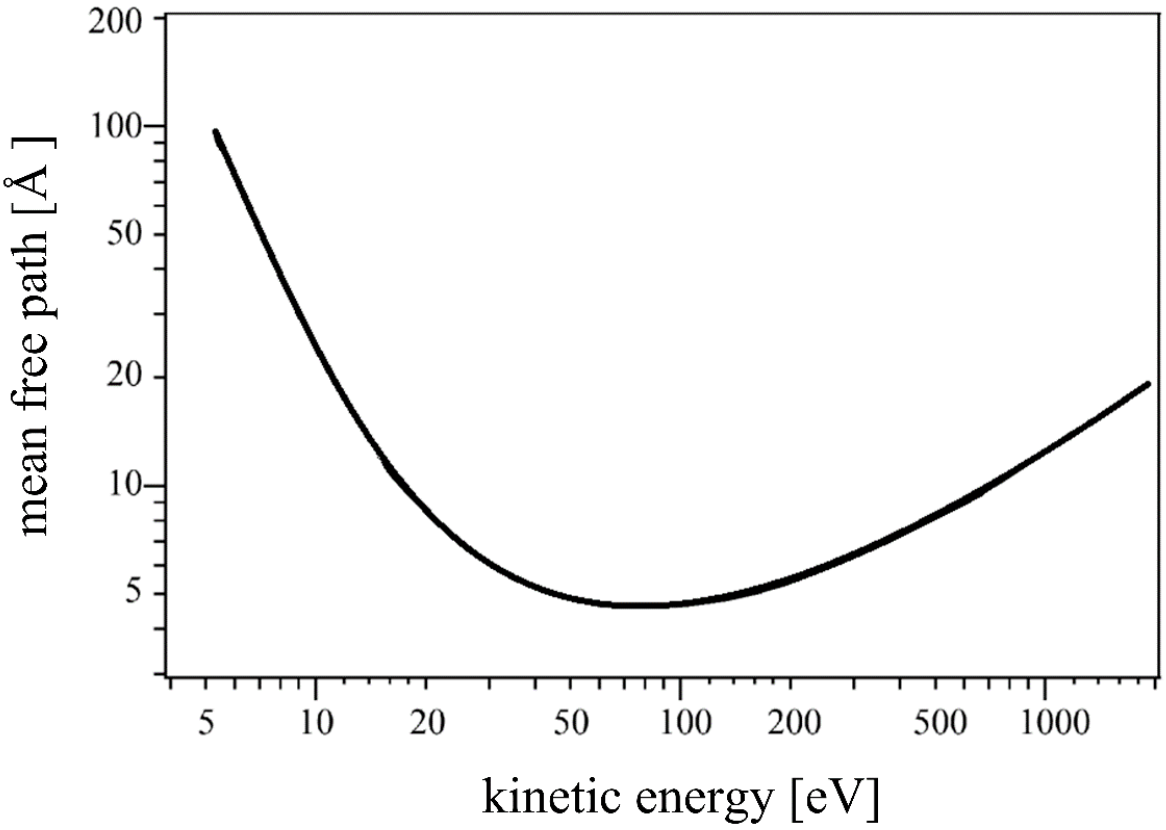

Figure 8: The universal plot of the electron mean free path as a function of the kinetic energy [70].

2.2.2: X-ray Photoemission Spectroscopy (XPS)

X-ray photoemission spectroscopy (XPS) is a type of PES which is used to probe material core levels by incident photons in X-ray range. The general X-ray source is Mg $K_{\alpha 1,2}$ line with 1253.6 eV photon energy created by electrons colliding with a Mg anode. The electrons in core-level states are excited and collected by an analyzer. The core-level electrons have

important information on the elemental composition which can be identified by plotting the counted number of photoelectrons (intensity) vs. binding energy. An example of XPS spectrum is shown in Figure 9. It is a typical XPS survey spectrum of a sputter cleaned Au. The emission features corresponding to core-level states can be identified clearly as characteristics for Au. As for a wide-scan survey spectrum, it serves as the basis for the determination of the elemental composition of a targeting sample. It has a higher peak intensity than a high-resolution scan at the expense of losing resolution by using higher pass energy mode.

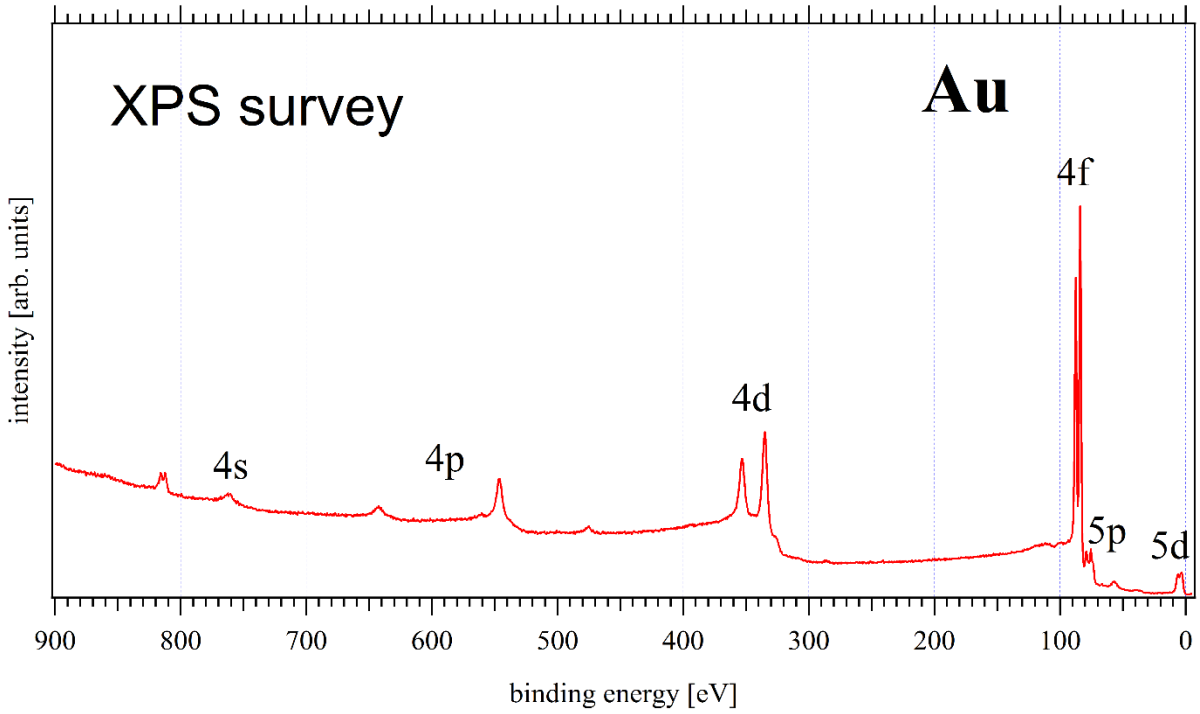

Figure 9: XPS survey spectrum of a sputter cleaned Au. Emission features are from corresponding core levels.

The binding energy of core levels depends on the chemical environment of an atom. By changing the local bonding environment, the binding energy of core levels can shift accordingly.

The chemical shift refers to the difference in binding energies between different chemical states of an atom. The shift direction depends on the attractive potential of the nucleus and the repulsive interaction with the surrounding electrons in the material. Figure 10 shows a high resolution XP-spectrum of the O 1s core level obtained from a thin film of TiO_2 nanoparticles. Besides a main O^{2-} core level which originates from the bulk oxide, a shoulder at higher binding energy is also shown. This shoulder represents the emissions from OH groups which are mostly on the surface of the TiO_2 nanoparticles [71]. The chemical shift observed in this spectrum is a result of the chemical environment change of the oxygen atoms i.e. the chemical environment in the bulk is different from the environment on the surface. The higher binding energy of the OH group indicates that it is more difficult to remove electrons from the surface than from the bulk.

The thickness of a thin film deposited on a substrate can be estimated by using the core level emissions from the substrate. The electrons excited from the substrate need to travel through the deposited thin film. During the passing through, the intensity of core level emissions decreases due to the increased probability of scattering. The attenuation of the intensity is a function of the thin film thickness. Therefore, the thickness of the deposited thin film can be calculated based on Lambert-Beer law

$$d = -\lambda \times \left(ln \frac{I}{I_0} \right) \tag{3}$$

in which d is the thickness of the film, λ is the electron mean free path in the film, I is the intensity of the core level emission from the substrate measured after the thin film deposition and I_0 is the intensity before the deposition. This estimation method is based on an assumption that the deposited thin film is homogenous since the intensities measured are averaged through the whole excited spot. Any existing pinholes, discontinued islands or other film defects can increase

the intensity of the core level from the substrate, resulting an underestimated thickness of the deposited thin film.

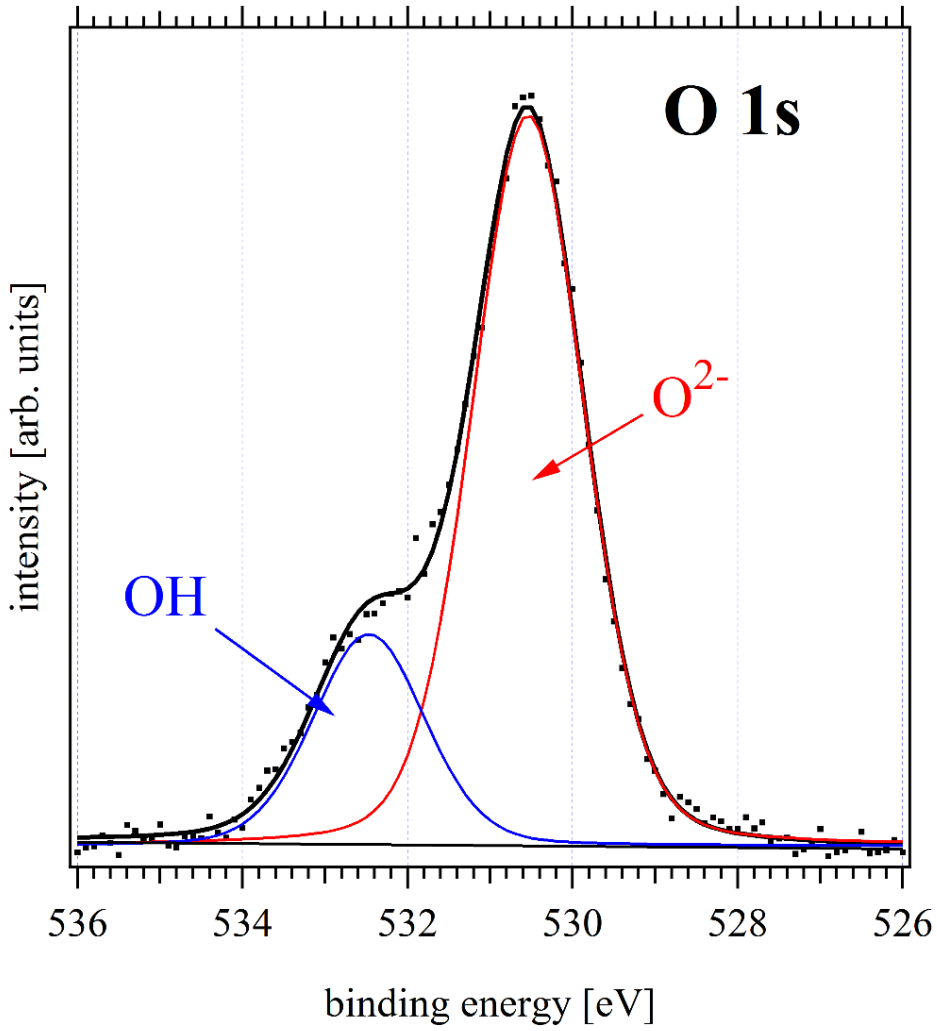

Figure 10: A high resolution XPS spectrum of the O 1s emission obtained from TiO_2 nanoparticles.

In XPS, core level emissions are described by the nomenclature nl_j in which n is the principle quantum number, l is the angular momentum quantum number and j is the total angular

momentum quantum number. Except for S levels, all the other orbital levels show doublet with two different energy states. These two different energy states have different binding energies. This is known as spin-orbit splitting [72]. For photoelectrons from p, d and f orbitals, the intensity ratio of the two spin orbital peaks are 1:2, 2:3 and 3:4, respectively. Figure 11 shows an example of a Ti 2p doublet measured from a thin film of TiO_2 nanoparticles. The peak intensity ratio between the $2p_{1/2}$ and $2p_{3/2}$ is 1:2.

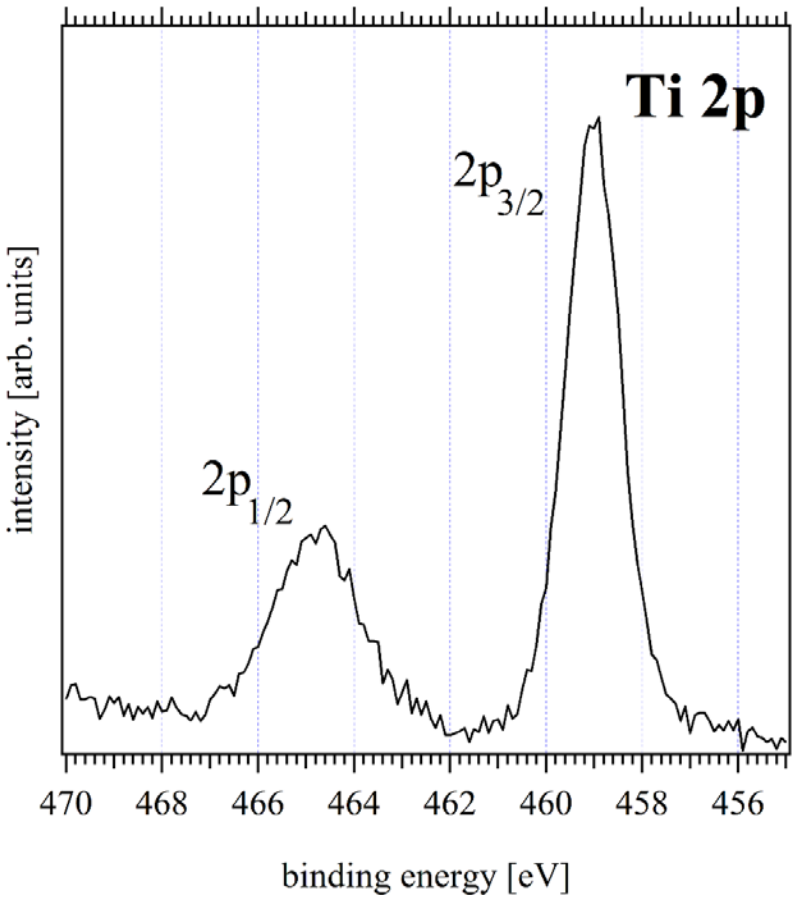

Figure 11: A high resolution Ti 2p core level with spin-orbit splitting doublet.

2.2.3: Ultraviolet Photoemission Spectroscopy (UPS)

Ultraviolet photoemission spectroscopy (UPS) is a type of PES using ultraviolet light as radiation source, such as He I emission line with photon energy of 21.2182 eV. With lower energy photons compared to XPS, UPS can be used to probe the valence band structure by exciting valence electrons out of the atomic outer shell. These electrons have lower binding energy (0-10 eV) which can be excited by x-ray as well. The advantage of UPS relies on the fine line width of an atomic transition in gas phase (10 meV). It gives UPS a much better resolution which enables to probe detailed valence structures of materials.

Figure 12 shows an example UP-spectrum measured from a thin film of TiO_2 nanoparticles. The secondary edge in the spectrum can be used to determine the sample work function which is the minimum energy required for electrons to escape from the surface. At this point, scattered secondary electrons barely have enough kinetic energy to escape from the surface. The surface conditions of materials have significant influence on the surface work function since the electrons have very short mean free path. Even a very thin layer of contaminations can change the surface work function dramatically. Therefore, ultra-high vacuum testing environment is required to obtain solid measurement data. Valence band emissions can provide valuable information from the density of states of the sample surface. The valence bands maximum (VBM) of inorganic materials or the highest occupied molecular orbital (HOMO) of organic materials obtained from UPS are crucial in the determination of charge injection barriers at a hetero-junction interface.

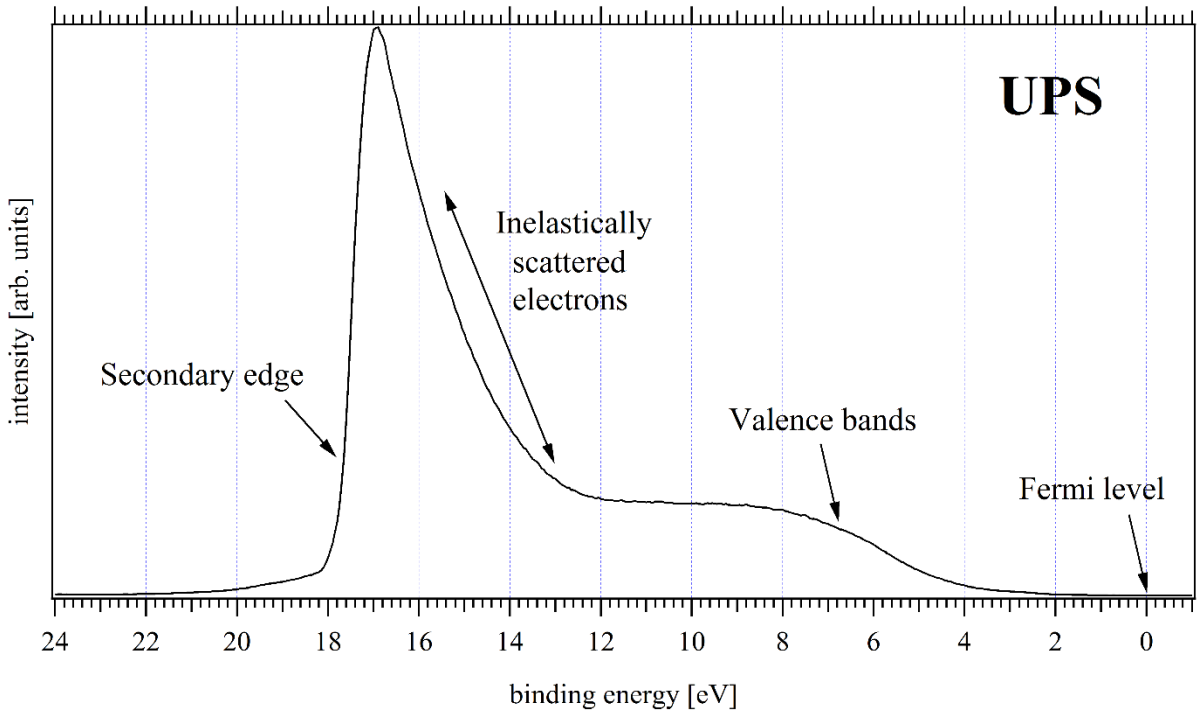

Figure 12: The characteristic UP-spectrum of TiO_2 nanoparticles. The whole spectrum is consisted of four main features which are secondary edge, inelastically scattered electrons, valence bands and Fermi level.

However, during UPS measurements the sample surface is modified by UV radiation resulting in two major artifacts. The first one is the build-up of positive charge during the measurement as a result of the incomplete replenishment of the emitted photoelectrons. The second artifact is related the surface photochemical reactions induced by the UV radiation. Both of these artifacts can shift the secondary electron cutoff and therefore change the measured work function significantly. The measurement challenge with regard to the charging artifacts can be circumvented by using low intensity X-ray photoemission (LIXPS), which is performed before UPS measurements when the sample surface is still free of charging effects. The photochemical reactions induced by the UV radiation requires the involvement of surface oxygen defects and

the presence of water [73]. This process is called hydroxylation. Therefore, to characterize oxide materials using UPS needs to be cautious.

2.2.4: Low Intensity X-ray Photoemission Spectroscopy (LIXPS)

Low intensity X-ray photoemission spectroscopy (LIXPS) was developed to determine the true work function of sample surface. When UPS measurements are performed on oxide materials, the sample surface can be modified through photochemical reactions [74]. As a result, the work function of the sample surface is changed. LIXPS measurements can measure the accurate work function by using low intensity of radiation which barely have significant influences of surface modifications. By applying LIXPS prior to the UPS measurement, the true work function can be determined. If the sample surface is modified by radiations with high intensity photon flux (UV or x-ray), the change of the work function can be observed from the LIXPS performed after the UPS instantaneously.

The reliability of LIXPS measurements has been proved by comparing it with Kelvin probe measurements, also known as surface potential microscopy [75]. Beerbom et al. performed both of LIXPS and Kelvin probe measurements on a solvent cleaned ITO surface before UPS measurements. Then the work function of the sample was measured with both techniques again after UPS measurements. The UV radiation induced work function changes were observed in their experiments. They conclude that LIXPS is able to detect the work function change caused by the UV radiation and provides the true work function of the sample surface. Figure 13 shows the normalized secondary edges measured from LIXPSa (before the UPS measurement), UPS, and LIXPSb (after the UPS measurement) on the thin film of TiO_2 nanoparticles. A significant shift of the secondary edge can be seen after the UPS measurement. This shift indicates the

formation of a permanent surface dipole as a result of the photochemical reactions induced by the UV radiation during the measurement.

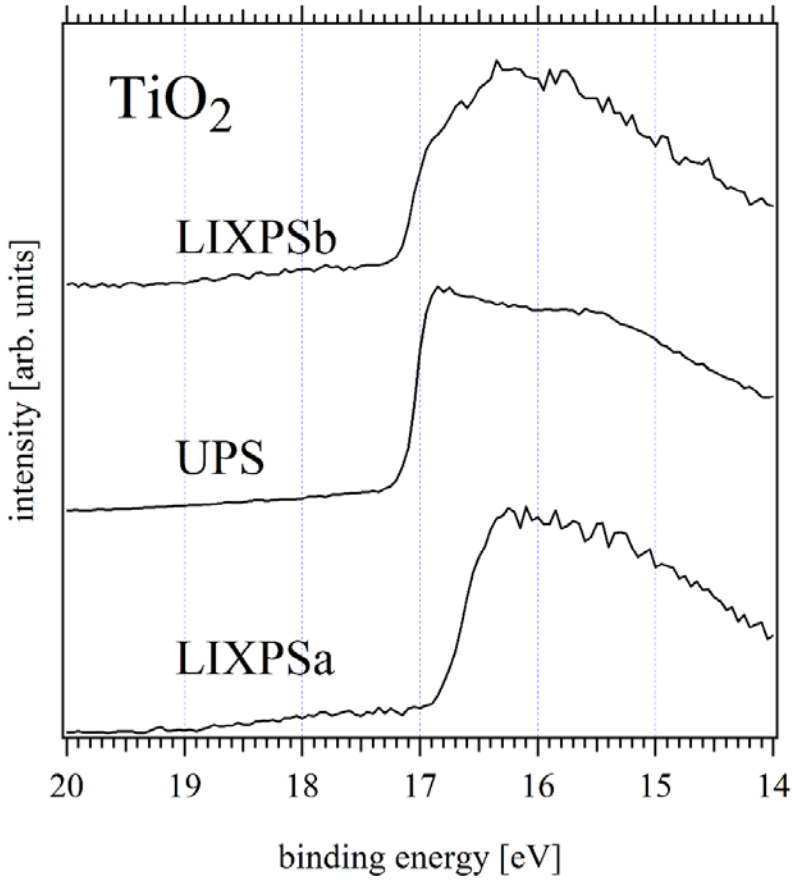

Figure 13: Secondary edge measured by LIXPS and UPS on a thin film of TiO_2 nanoparticles. The LIXPSa refers to the LIXPS measurement before the UPS measurement. The LIXPSb spectrum was obtained from the measurement after the UPS measurement.

2.3: Ultraviolet-visible Spectroscopy (UV-vis)

Ultraviolet-visible spectroscopy is one particular type of absorption spectroscopy in the ultraviolet-visible range (200-800 nm). The photon wavelength can be converted into the photon energy by using the following equation:

$$E = \frac{h\lambda}{c} \quad (4)$$

In this equation h refers to Plank constant and c is the speed of light. Therefore, the excitation energy in the ultraviolet-visible range is from 6.2 to 1.5 eV.

The photons with energy higher than the band gap of materials can be absorbed while the others with lower energy will pass through. Therefore, UV-vis spectroscopy is a useful tool to estimate the optical band of various materials.

2.4: Experimental Setup

Orbital alignment characterization requires highly clean sample preparation and measurement environment due to the sensitivity of surface science. The experiments described in this dissertation were carried out in a multi-chamber UHV system in which the sample preparation and characterization were performed *in-situ*, preventing ambient contaminations to the best.

2.4.1: Multi-chamber UHV System

A commercial multi-chamber setup was used to deposit targeting materials and to characterize electronic structures of samples. The base pressure of this system was 2 x 10^{-10} mbar. Figure 14 shows the top view of this system which consists of three main chambers connected via an *in-situ* transfer system. The electrospray chamber was outfitted with a customized electrospray deposition system which enabled direct thin film deposition on a substrate in the vacuum chamber. In the transfer chamber, substrates can be sputtered with Ar+ ions (SPECS IQE 11/35 ion source) to get rid of surface contaminations. The analysis chamber was equipped with an X-ray source (SPECS XR50) and a UV source (SPECS UVS 10/35) to perform PES measurements. The emitted photoelectrons were captured and counted by a hemispherical energy analyzer (SPECS PHOIBOS 100).

A customized glove box was attached to the system through a fast entry lock from which samples can be transferred directly from the glove box into the UHV system. The glove box was kept in N_2 rich environment under a slight overpressure to protect sample surfaces. A diaphragm pump was connected in series with two filters in which active carbon and Drierite drying agent were filled in order to get rid of contaminations in the glove box.

In the electrospray deposition, a bias voltage of -2 kV was applied by a Keithley high voltage power supply (248). A Cole-Parmer syringe pump (WU-74900-00) was used and the pumping speed was set at 4 mL/h. Hamilton stainless steel cone tip needles (7785-01) and Hamilton syringes (22194-U) with a volume of 5 mL were used and purchased from Sigma Alrich.

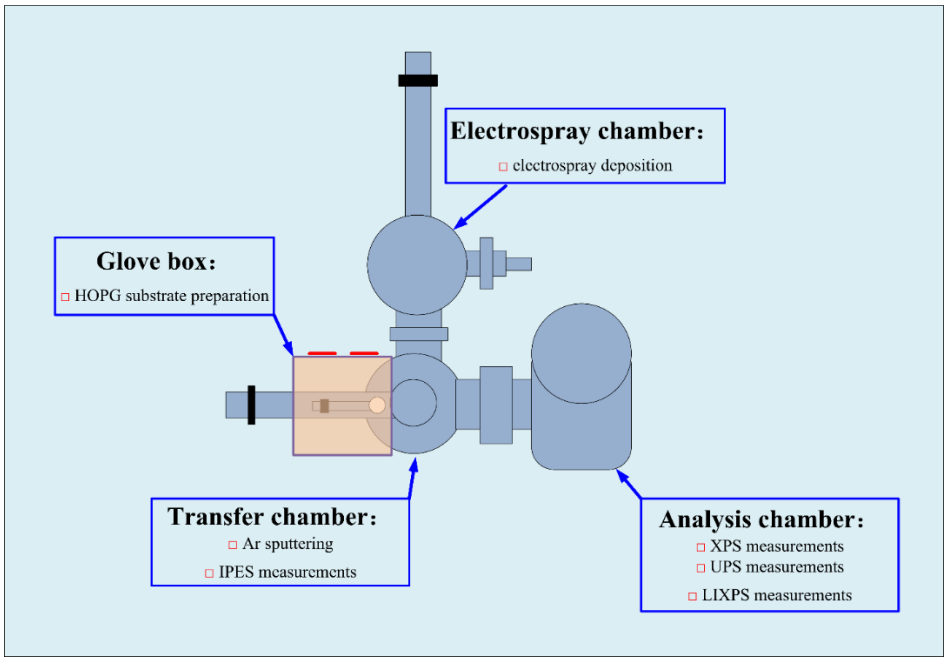

Figure 14: The multi-chamber deposition and characterization system. The system consists of four major parts. Samples can be loaded either from the glove box or the fast entry lock.

2.4.2: Substrate Preparation

The particular substrate used in different experiments is introduced in the corresponding chapter and section. The substrates of a 100 nm thick Au thin film on glass slides coated with Ti thin film were purchased from EMF Corp. (Ithaca, NY). After cutting the substrates into 1 cm × 1 cm pieces, they were mounted on customized sample holders with two mounting screws providing a good electrical contact between the Au surface and the sample holder to prevent the presence of charging effects. Then they were rinsing cleaned with acetone, methanol, isopropanol, and deionized water and dried with the nitrogen flow before they were loaded into the chamber. After loading, the Au substrates were sputtered with Ar+ ions for 40 min to get rid of the surface contaminations.

Highly ordered pyrolytic graphite (HOPG) substrates (Mikromasch, USA, "ZYA" quality) were prepared in the glove box. The HOPG was glued on the sample holder via conductive silver epoxy providing good electrical contact. The HOPG substrate with a pristine surface was prepared by cleaving several top layers off using a scotch tape in the glove box before it was loaded into the chamber.

2.4.3: Measurements and Data Analysis

The prepared samples were characterized by LIXPSa, UPS, LIXPSb, and XPS in sequence. This measurement sequence was specifically designed to evaluate the surface modification by the UV radiation and the influence of surface charging artifacts. LIXPS measurements were performed by using the stand-by mode of the X-ray gun (Mg Kα, 1253.6 eV, 0.1 mA emission current). The He I (21.2182 eV) line was used in UPS measurements by adjusting the applied voltage to 450 V. For standard XPS measurements, the X-ray gun was operated under operation mode (Mg Kα, 1253.6 eV, 20 mA emission current). The analyzer was

calibrated using a sputter cleaned Au sample to yield the Fermi level at 0 eV and Au $4f_{7/2}$ at 84 eV.

A -10 V bias voltage was applied to the sample during all LIXPS and UPS measurements in order to separate the sample secondary edge from the analyzer secondary edge and increase the yield of secondary electrons. This bias potential was corrected during the data analysis. The data analysis was completed with the Igor Pro software (WaveMetrics, Inc.).

CHAPTER 3: INTERNAL ORBITAL ALIGNMENT IN OLIGOTHIOPHENE-TIO_2 NANOPARTICLE HYBRIDS

This chapter focuses on the measurement of the internal orbital alignment in the oligothiophene-TiO_2 nanoparticle hybrids by applying a PES base characterization protocol. The charge injection barriers and the internal interface dipole are determined through a series of meticulously designed experiments. The influences of covalent bonds in the hybrids are discussed. [1]

3.1: Introduction

Compared to the underlying principles of conventional solar cells, the fundamental mechanisms of organic photovoltaic cells mostly are dependent on the properties of the interfaces rather than the bulk properties of the materials used to fabricate these devices [76, 77]. Because the energy conversion efficiency from photons to electricity strongly depends on the efficiency of charge separation in organic and hybrid solar cells. In comparison to the generating process of free carriers in conventional solar cells, the charge separation in novel cells requires to dissociate relatively strongly bound excitons into free carriers [78]. The dissociation efficiency of excitons is largely determined by the orbital line-up at the interface between the donor material and the acceptor material in the active layer. By mixing organic materials with inorganic

[1] This chapter has already been published in the Journal of Physical Chemistry C (Li, Z., H. Berger, K. Okamoto, Q. Zhang, C. K. Luscombe, G. Cao and R. Schlaf (2013). "Measurement of the Internal Orbital Alignment of Oligothiophene-TiO2 Nanoparticle Hybrids." The Journal of Physical Chemistry C 117(27): 13961-13970.). Permission is included in Appendix A.

materials in the active layer, a hybrid photovoltaic structure is formed taking the advantages of both materials [79]. Inorganic semiconducting materials, such as TiO_2, CdSe and ZnO, can be used as the electron acceptors in hybrid structures due to their relatively low electron affinity and high electron mobility [18, 80, 81]. Organic conjugated polymers, such as P3HT, MEH-PPV and PCPDTBT, can act as the electron donors due to their low band gap and high hole mobility [82-84]. However, the energy conversion efficiency of such hybrid solar cells is limited by the low exciton dissociation efficiency due to the short diffusion length of excitons and unideal band offsets at the interface [15].

Among various inorganic acceptor materials, TiO_2 nanoparticles are attractive candidates because their band gap and electronic properties can be tuned through size modification during the synthesis process to meet different requirements [85]. In the category of promising organic donor materials, thiophene based materials have shown intriguing optoelectronic application potentials, such as thin film bulk hetero-junction solar cells and organic thin-film transistors [86, 87]. Taking the advantages of both materials, novel solar cells with hybrid hetero-junction structure can be realized with practical potentials. However, like a typical "hybrid" photovoltaic structure, the low exciton separation efficiency at the interface between thiophene based organic materials and TiO_2 nanoparticles is a challenge in current research due to the short exciton diffusion length (about 10 nm) which is difficult to optimize by using physical blending fabrication technique [18, 39]. A promising solution to optimize organic/inorganic interfaces is to synthesize real hybrid molecules in which organic materials are covalently bonded with inorganic materials [88]. Thiophene based oligomers with an ordered and well defined molecular structure are ideal prototypical materials to study the properties of internal orbital alignments in hybrid molecules [89-91]. The oligothiophene molecules can be covalently grafted

onto TiO_2 surface through carboxyl anchor groups. The anchor chemistry is critical for the properties of the interface [92]. Pioneering works in this field have been reported. Theoretical investigations performed by Serban et al. suggest that carboxyl groups have an affinity to bond with TiO_2, indicating that carboxyl groups are good anchors to achieve hybridization [93]. Ding et al. studied the charge transfer efficiency of poly(thiophene-3-acetic acid)-TiO_2 hybrid materials fabricated layer by layer using carboxyl groups as anchors [94]. Their results conclude that efficient electron transportation from the organic part into the nanoparticles is achieved as suggested by the increase of photocurrent.

The orbital alignment at the internal interface in hybrid materials mostly determines the charge separation and transportation. Photoemission spectroscopy (PES) is a powerful surface and interface characterization technique which has been used for several decades to characterize the orbital alignment at inorganic/organic interfaces [19, 50, 95]. In this chapter, a methodology allowing the application of this technique to the internal interface characterization in hybrid materials is developed and discussed using oligothiophene-TiO_2 nanoparticle hybrids as an example.

3.2: Experimental

The conventional interface between two types of materials, such as Schottky barriers or semiconductor hetero-junction can be fabricated and characterized by a sequence of in-vacuum deposition steps. The deposition of one material on the substrate is followed by the deposition of another material in several steps. In-between deposition steps PES measurements (XPS and UPS) are carried out to obtain corresponding spectra. This can yield a spectral sequence which allows the determination of the orbital alignment at the interface. This interface characterization technique is well-established and has been applied to a large variety of materials ranging from

III-V semiconductors to conductive polymers and bio-molecular materials [96-99]. The challenge of the characterization on hybrid internal interfaces is that the bonded two components cannot be deposited individually while retaining the property as assembly. This prevents the density of states measurement of the individual constituent in the hybrid. Instead, PES measurement will yield a superimposed spectrum of both density of states. This prevents a straightforward determination of the orbital alignment at the internal interface in hybrids. Hence, a different approach needs to be developed and validated.

The PES based characterization methodology can circumvent this challenge through the initial characterizations of the electronic structure of the individual constituent, respectively. The constituent materials can be characterized by the PES measurements separately. The electrospray deposition technique enables direct characterization after the deposition minimizing the ambient contamination. Key properties of the constituent can be obtained. Then, the hybrids will be measured to obtain data of core levels. Figure 15 illustrates the complete experimental design flow. In the first experiment, pure TiO_2 nanoparticles were deposited on a sputter cleaned Au substrate followed by a series of PES measurements to determine the work function, VBM and species core levels. The data was used in the discussion of the electronic structure determination within the hybrid material. In the second experiment, the oligothiophene-TiO_2 nanoparticle hybrids were deposited on a sputter cleaned Au substrate as well. The core level information of the hybrids was extracted from this experiment. In the third experiment, the oligothiophene ligands were deposited in several steps and characterized by PES measurements to determine the work function, HOMO cutoff and species core levels.

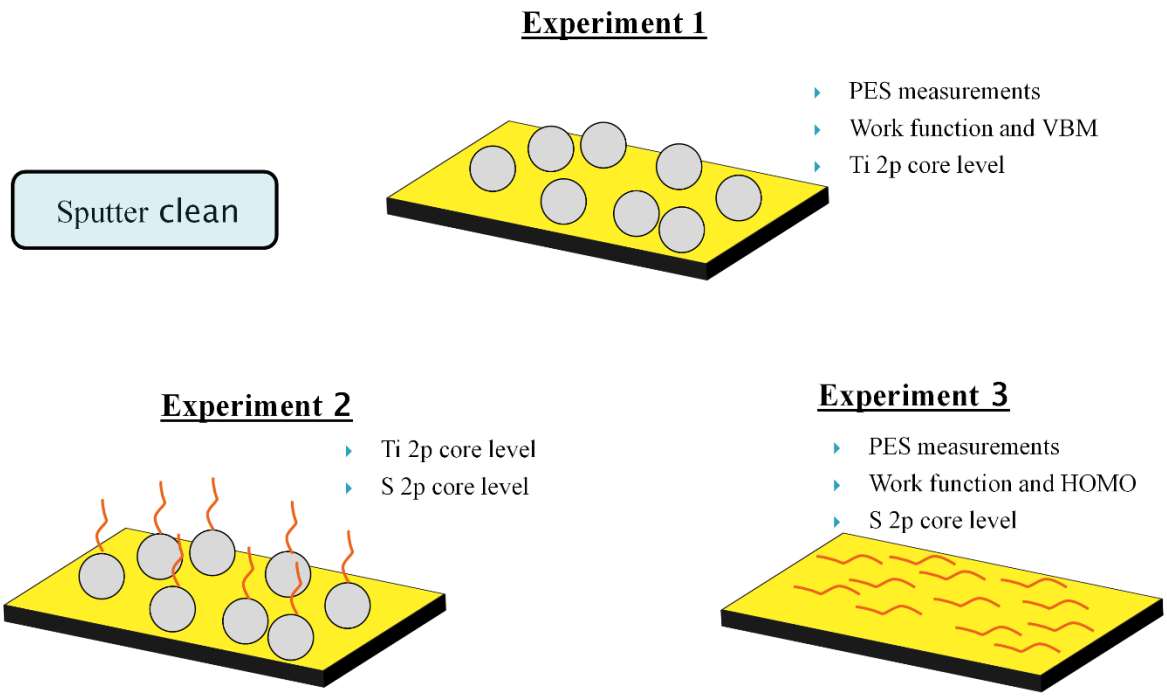

Figure 15: Schematic demonstration of the design of experiments. In the first experiment, the pure TiO_2 nanoparticles are characterized. The hybrid materials are characterized in the second experiment. The oligothiophene ligands are characterized in the third experiment.

The orbital alignment at the internal interface can be determined from the binding energy of XPS core levels in the hybrid in comparison to the binding energies measured in the pure samples because the energy difference from core levels to VBM/HOMO is a material constant. The so determined binding energy shifts of the core levels allow for the calculation of the HOMO and valence band maximum energies within the hybrid whose difference corresponds to the hole injection barrier. Since the ionization energy is a material constant as well, the internal interface dipole in hybrids can be determined accordingly using the VBM and HOMO cutoff of the hybrid constituents. The corresponding electron injection barrier energy i.e. band offset of the lowest unoccupied molecular orbitals (LUMO) and the conduction bands minimum can be

estimated by taking the HOMO-LUMO gap of the oligothiophene and the band gap of the TiO_2 into account. Therefore, the orbital alignment at the internal interface can be determined. Figure 16 illustrates this determination process from the perspective of band diagrams.

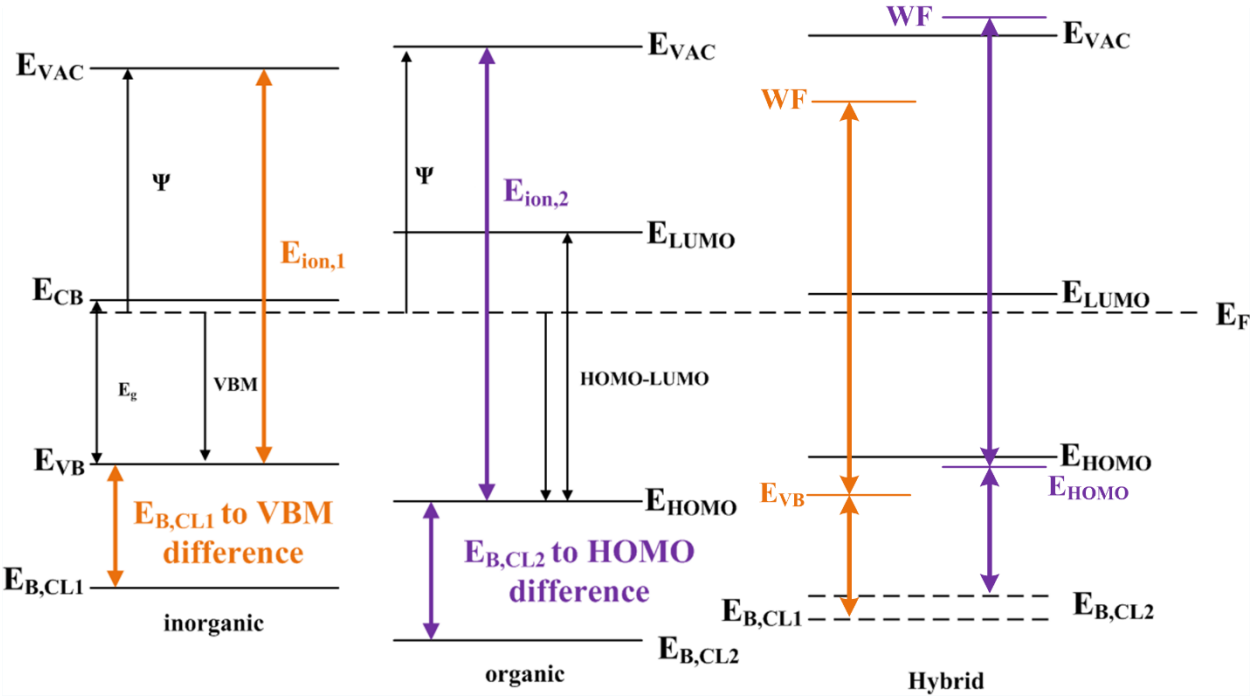

Figure 16: The electronic structure of the individual constituent in isolation and the orbital alignment at the internal interface in hybrids.

The anatase TiO_2 nanoparticles were dispersed in a solution of H_2O and ethanol at a 1:1 ratio with the concentration of 5 mg/mL. The solutions used in the experiments were sonicated and stirred vigorously to ensure that the nanoparticles were dispersed well to get rid of undesired clusters. The TiO_2 nanoparticles were synthesized with a sol made of 0.05 M titanium isopropoxide, 0.1 M HCl, and 0.01 M surfactant (Igepal CO-520) through a hydrothermal reaction at ~250 °C [100]. The oligothiophene ligands and the oligothiophene-TiO_2 nanoparticle

hybrids were dissolved in chloroform at the concentration of 1 mg/mL. The molecules used in the experiments were provided by the cooperating groups at the University of Washington.

The characterizations on the individual component were performed as follows: First, 7 mL of the solution containing TiO_2 nanoparticles was injected into the chamber and deposited on a sputter cleaned Au substrate. The measurements on this sample with XPS and UPS yielded a sequence of spectra of pure TiO_2 nanoparticles. The oligothiophene ligands were deposited with the same method on a sputtered clean Au substrate as well. The XPS and UPS measurements were performed after the step by step deposition. The reason for using several deposition steps was to achieve a maximized film thickness while preventing significant sample charging effects. The next experiment was to deposit oligothiophene-TiO_2 hybrid on a sputter cleaned Au substrate in several steps. Then the hybrid thin film was characterized by XPS and UPS step after step.

3.3: Results

The main objectives of the designed experiments are to measure the charge injection barriers and the dipole at the internal interface in the oligothiophene-TiO_2 nanoparticle hybrids.

3.3.1: Characterization of the Electronic Structure of TiO_2 Nanoparticles

The pure TiO_2 nanoparticles were sprayed into the chamber and deposited on a sputter cleaned Au substrate followed by the PES measurements to characterize the electronic structure. In the deposition 7 mL solution in total was injected into the chamber through the electrospray deposition setup. Figure 17 shows the LIXP- and UP-spectra measured before and after the TiO_2 deposition. The center panel shows two complete UP-spectra measured from the substrate (in black) and the TiO_2 nanoparticles thin film (in blue), respectively. The normalized secondary edges obtained from LIXPS measurements before and after the deposition are shown on the left

panel. The right panel shows the spectra of the magnified valence features after background subtraction.

Telling from the left panel in Figure17, the secondary edge shifts to a higher binding energy after the deposition of the TiO_2 nanoparticles resulting in the presence of a positive interface dipole between the deposited layer and the substrate. The values of work function were calculated by subtracting the cutoff binding energy from the excitation energy (21.21 eV) and taking the analyzer broadening of approx. 0.1 eV into account. Before the deposition of TiO_2 nanoparticles, the cutoff of the Au secondary edge is around 15.8 eV which gives a value of 5.5 eV for the work function of the Au substrate. After the deposition, the surface secondary edge shifts to a higher binding energy level. The corresponding work function for the TiO_2 nanoparticle is determined to be 4.46 eV. The black bottom spectrum in the center graph represents a typical UP-spectrum expected for a sputter cleaned Au substrate. The spectral features originated from the valence emissions can be identified clearly from 0 to 8 eV. After the deposition of TiO_2 nanoparticles, these features are suppressed and replaced by the features corresponding to the valence emission from the thin film of TiO_2 nanoparticles. The TiO_2 related valence emissions can be identified in the right graph of Figure 17 after background subtraction. There are two strong emission peaks, a narrow one at 8 eV and a relative broad one at 6 eV. The narrow feature at 8 eV originates from nonbonding π^* O 2p orbitals of the TiO_2 nanoparticles, while the broad one located at 6 eV is from the bonding σ orbitals [101]. It is worthy to notice that the small feature around 2.5 eV is related to oxygen vacancies at the TiO_2 surface, which are located in the band gap [102].

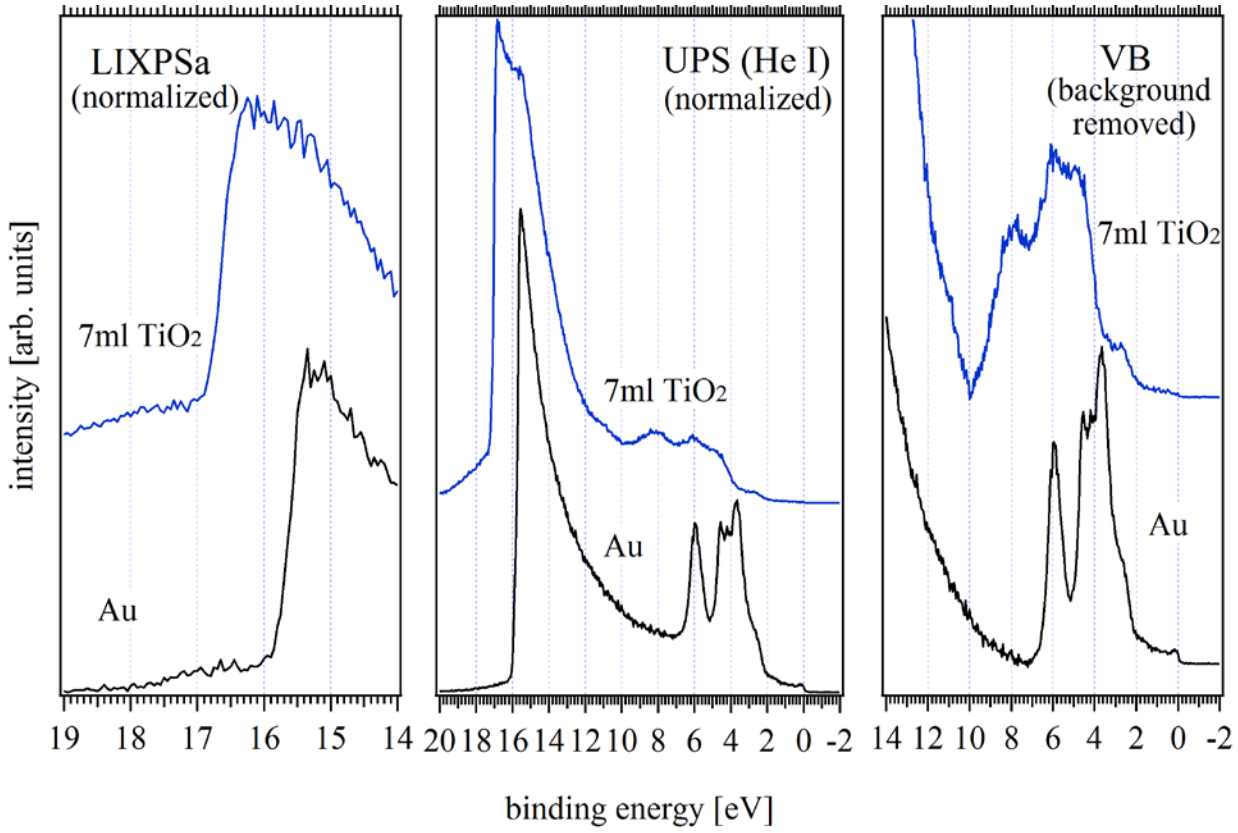

Figure 17: LIXP- and UP-spectra of the sample before and after the TiO_2 deposition. The graph in the left panel is the normalized secondary edge measured with LIXPS before UPS. The complete UP-spectra are in the center panel. The right panel shows the valence band features. (Reprinted (adapted) with permission from [103]. Copyright 2013 American Chemical Society)

The normalized secondary edges measured from the thin film of TiO_2 nanoparticles in a certain order are shown in Figure 18. The bottom LIXP-spectrum shows the initially measured secondary edge with LIXPS prior to the UPS measurement. The second spectrum shows the secondary edge measured by UPS. The third spectrum is the second LIXP-spectrum measured after the UPS measurement. These spectra are shown normalized because the UP-spectrum has a magnitudes higher intensity compared to the LIXP-spectrum. With this specific measurement order, charging artifacts as well as photochemical surface modifications potentially occurring

during the UPS measurement can be detected and evaluated. The difference between the values measured from the first LIXPS and UPS usually suggests the presence of small charging artifacts induced by UV radiation. Therefore, all work function values used in the following discussion were extracted from LIXPSa measurements, which are free from charging effects. The LIXPSa spectrum in Figure 18 reveals that the TiO_2 nanoparticle film has a work function of 4.44 eV which is consistent with a previous report by Cahen et al. based on Kelvin probe measurements [104] and previous measurements by the authors' group [20]. The second LIXPS performed after the UPS measurement indicates the work function change is permanent. It is mostly a result of the surface modification caused by photochemical reactions which involve the presence of water molecules and photons in UV range.

Figure 19 shows the corresponding O 1s and Ti 2p core level emissions obtained from XPS measurements matching the above experimental sequence. The panels show from left to right the O 1s and Ti 2p emission lines measured before and after the deposition of the TiO_2 nanoparticles. The O 1s spectrum in black only shows a weak emission, which indicates that there were some oxide related residual contaminations on the substrate surface. After the deposition of the TiO_2 nanoparticles on the substrate, a strong O 1s emission peak emerges at 530.8 eV. This emission line is related to the oxygen atoms in the TiO_2 film. The main feature relates to the O^{2-} group in the bulk. At higher binding energy level, there is a small feature can be identified. This feature is from the OH group on the surface. In the right panel of Figure 19, the black flat spectrum measured from the substrate indicates that the substrate is free of Ti atoms. After the deposition, the Ti 2p emissions in blue show a similar trend in tandem with the O 1s emissions. The appearance of these emission lines confirmed the deposition of the film. The results show that the intensity ratio between the Ti $2p_{3/2}$ and the Ti $2p_{1/2}$ is 2:1, and the binding

energy difference between the splitting states is 5.54 eV. The binding energy of the Ti $2p_{3/2}$ peak is at 459.55 eV. It should be noted that the Ti emissions related to the surface cannot be distinguished from the Ti bulk emissions in the spectrum.

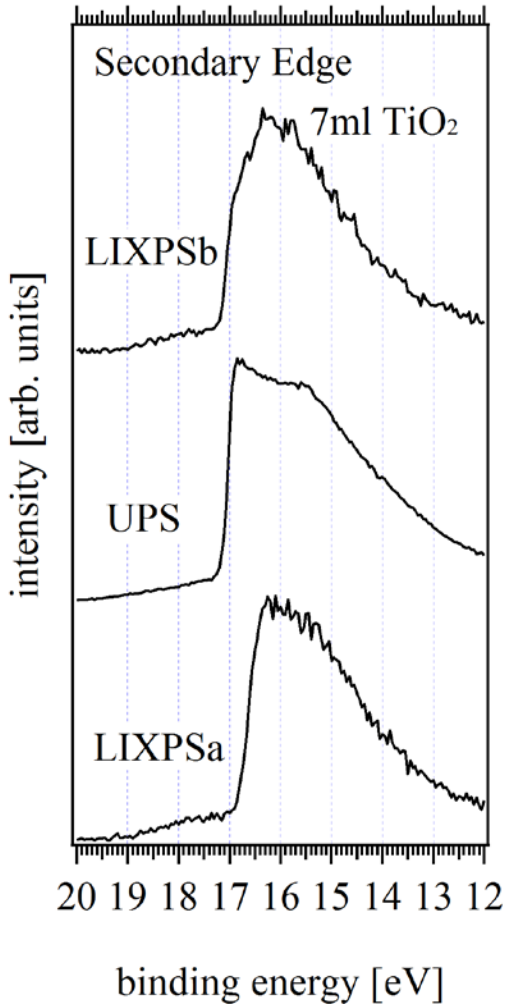

Figure 18: The normalized secondary edges measured for the thin film of TiO_2 nanoparticle with LIXPSa, UPS and LIXPSb in sequence. (Reprinted (adapted) with permission from [103]. Copyright 2013 American Chemical Society)

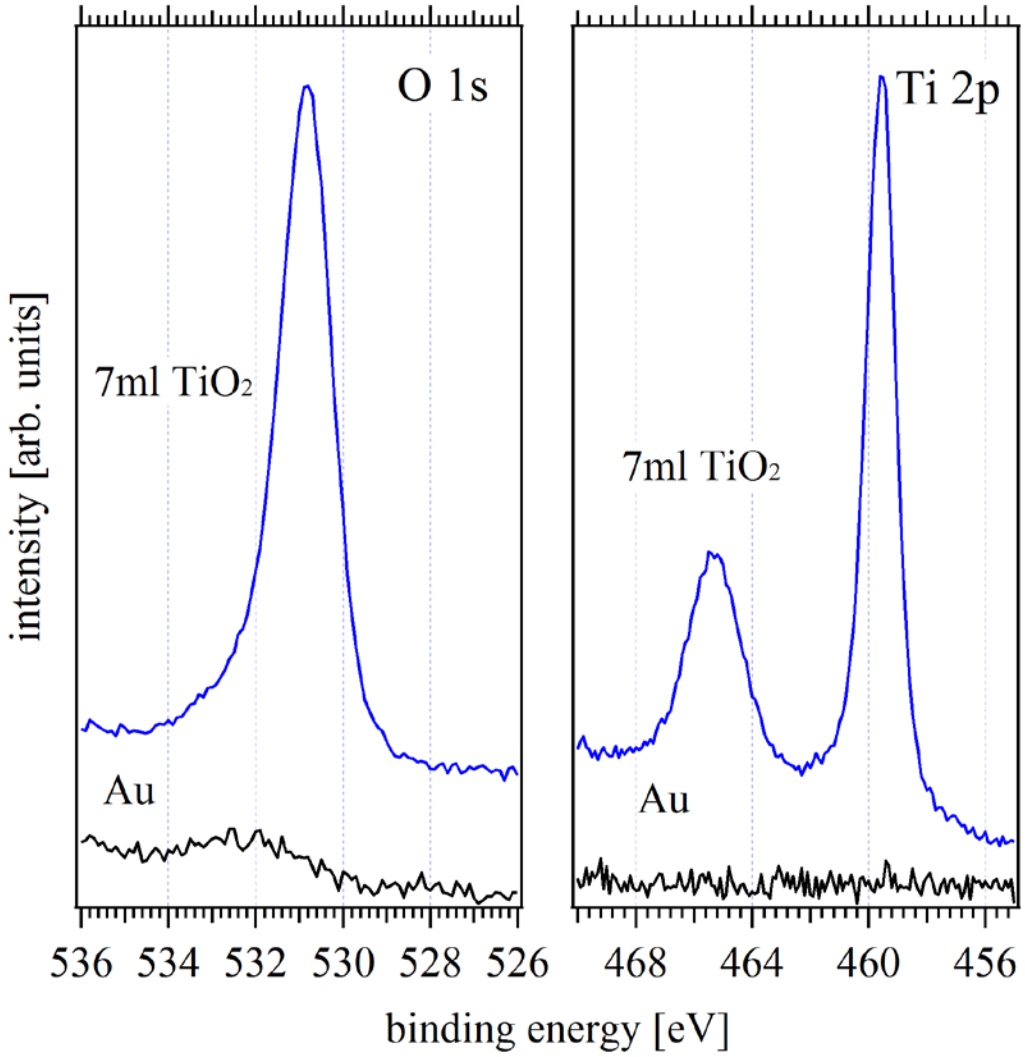

Figure 19: The XPS core level (O 1s and Ti 2p) spectra measured from the sample before and after the deposition of TiO_2 nanoparticles. (Reprinted (adapted) with permission from [103]. Copyright 2013 American Chemical Society)

3.3.2: Characterization of the Electronic Structure of Oligothiophene Ligands

In this section the oligothiophene ligands were deposited on a sputtered clean Au substrate in four steps starting at 0.02 mL by the electrospray technique. The injection volume of

each step was well controlled in order to void the influence of charging artifacts which were induced by the UV radiation during the UPS measurements. Figure 20 shows the LIXP- and UP-spectra measured before the deposition and after each deposition step during this experiment. The center panel shows a series of complete UP-spectra after normalization. The side panels show the normalized secondary edge (left) as well as the valence bands/HOMO region after background subtraction (right). The shift of the secondary edge after the first 0.02 mL deposition step indicates that there was an interface dipole at the oligothiophene/Au interface. The bottom black spectrum in the center panel shows the typical emissions expected for a sputter cleaned Au surface.

During the subsequent four-step deposition series of oligothiophene ligands, the emission features of the Au substrate are gradually attenuated and finally replaced by the emissions originated from the HOMO of the ligand molecules. This process is manifested evidently from the right panel in which the spectra were normalized and the background of each spectrum was removed. The emission features from -2 to 14 eV were magnified and shown in the right panel. As shown in the right panel, the features corresponding to the valence band emissions of the Au substrate can still be seen after the first 0.02 mL deposition step. This means that the ligands film is not thick enough to cover the emission from the Au substrate. Furthermore, these features are still identifiable after the 0.06 mL deposition in total while the features of the HOMO emissions from the ligand film are merging in the spectrum. After the third deposition step with the amount of 0.14 mL in total, the emissions from the Au substrate are suppressed and replaced by the emissions from the ligands film completely. There are two main features can be identified, a broad one around 7 eV and a small one around 3 eV.

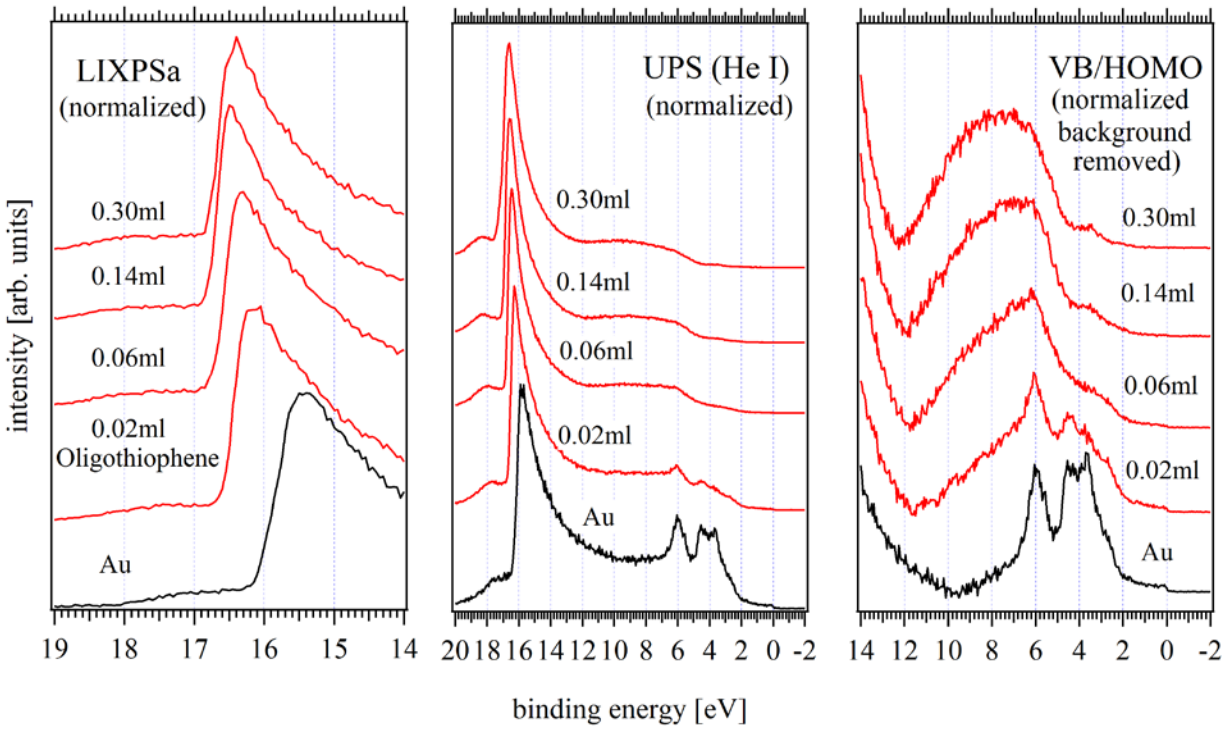

Figure 20: LIXP- and UP-spectra of each experimental step. The normalized LIXP-spectra are shown in the left panel. The complete UP-spectra are shown in the center panel. The magnified VB/HOMO regions after background subtraction are shown in the right panel. (Reprinted (adapted) with permission from [103]. Copyright 2013 American Chemical Society)

The values of determined work function for each deposition step are summarized and plotted in Figure 21. The figure also shows the corresponding work function values determined from LIXPS measurements done before (LIXPS a) and after (LIXPS b) each UPS measurement. These trilogy measurements allow the detection of charging artifacts which are induced during the UPS measurement by UV radiation. After the fifth deposition, evident charging phenomena occurred in the UPS measurement as is apparent from the large discrepancy between LIXPSa and UPS derived values. All work function values used in the following were extracted from the set of LIXPSa measurements.

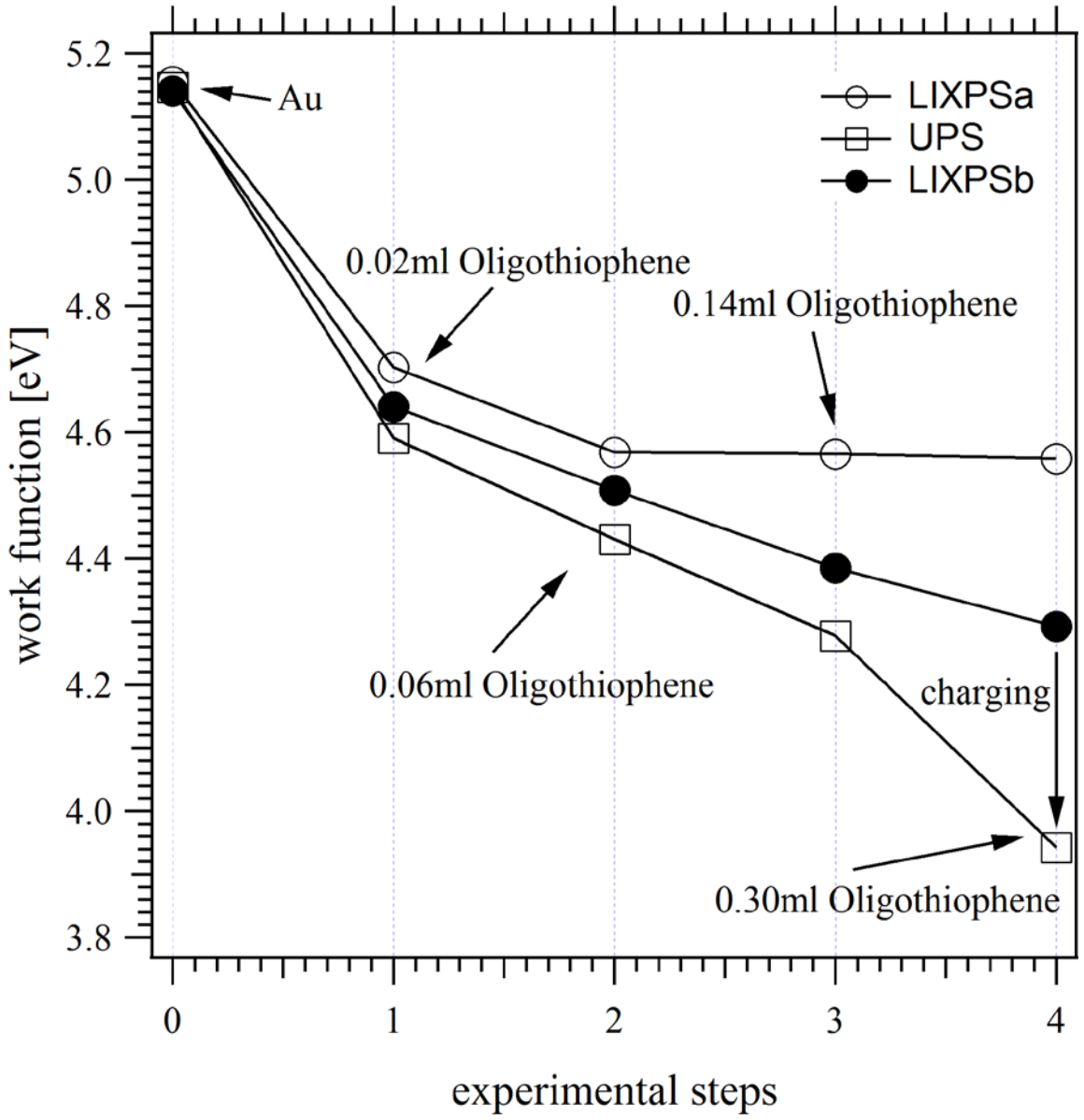

Figure 21: Work function values obtained from LIXPS and UPS measurements corresponding to the four-step deposition sequence. LIXPSa was performed before UPS and LIXPSb was after. (Reprinted (adapted) with permission from [103]. Copyright 2013 American Chemical Society)

Figure 22 shows the corresponding XPS core level lines matching the above UP-spectra sequence of each deposition step. The whole figure consists of three panels showing from left to

right, the Au substrate-related Au 4f emission line, and the ligands related C 1s and S 2p lines. The flat C 1s spectrum in black is as expected for a clean surface after sputtering. A strong C 1s emission line merges at 285 eV after the first deposition, which is originated from the carbon atoms of the oligothiophene ligands. Initially, the clean Au substrate does not show any S 2p emissions as indicated by the black spectrum in the right panel. After the first 0.02 mL deposition step, there is no obvious S 2p line shown in the spectra. The evident S 2p line can be identified after the 0.06 mL deposition step. The analyzable spectrum with reasonable noise to signal was obtained after the 0.14 mL deposition step from which the binding energy of the S 2p doublet was determined. Along with the increase of the deposition amount from 0.02 mL to 0.30 mL in total, the intensity of the Au 4f emission decreases due to the absorption of emitted electrons in the oligothiophene film.

The thickness of the oligothiophene thin film can be estimated based on the attenuation of the Au 4f line. According to the Lambert-Beer law described in the section 2.2.2, the film thickness is as a function of the electron mean free path λ which is about 50 Å in oligothiophene films [105]. Therefore, the thickness of the film after 0.14 mL deposition step was estimated to be 2 nm. In contrast, the ligands related C 1s and S 2p lines (spectra in red) show an intensity increase as the amount of oligothiophene increases accordingly. The C 1s and S 2p emission lines remain at the same binding energy throughout the deposition sequence. Hence, it can be concluded that no significant charging effects or band bending occurred at the interface to the substrate during the entire deposition series.

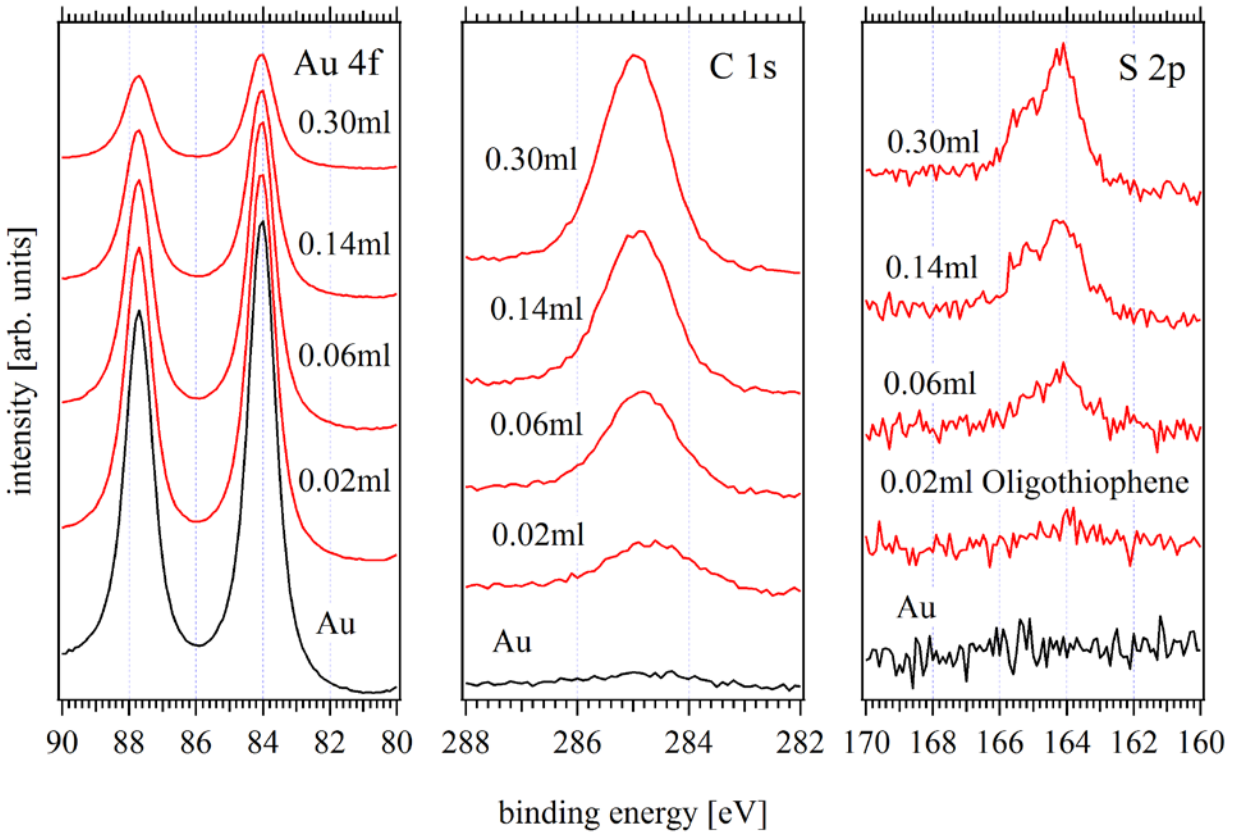

Figure 22: The core level lines (Au 4f, C 1s and S 2p) measured after each deposition step. The increasing intensities of the C 1s and S 2p are matching the amount of deposited ligands. (Reprinted (adapted) with permission from [103]. Copyright 2013 American Chemical Society)

3.3.3: Characterization of the Electronic Structure of the Oligothiophene-TiO_2 Nanoparticle Hybrids

Figure 23 shows the normalized UP-spectra measured after each deposition of the oligothiophene-TiO_2 nanoparticle hybrids on a sputtered Au substrate. The deposition started at 1 mL solution injection and ended at 12 mL in total. The bottom spectrum is the UP-spectrum of the clean substrate. The typical features from 2 to 8 eV and the Fermi level at 0 eV can be identified clearly. After the following deposition of the hybrids, the features of the valence

emissions from the Au substrate are gradually attenuated and then completely replaced by the emissions originating from the valence bands of the hybrid materials after the third deposition step (7 mL injected solution in total). The valence features of the hybrids arise from the superposition of the emissions from the valence bands of the TiO_2 nanoparticles and the HOMO of the oligothiophene ligands. The superposition makes it impossible to distinguish the two constituents from each other in the spectra, as manifested by the spectra in Figure 23. Therefore, the orbital alignment in the hybrid materials cannot be determined directly from the UP-spectra as measured. Even though the UP-spectra measured from the hybrids cannot provide direct information of the internal interface, the features from the superposed emissions can still provide valuable insights into the electronic structure of the hybrid materials as a complete configuration. This is crucial when it comes to evaluate the interface between the hybrid materials and the other materials. However, this is not the main objective of this dissertation.

The corresponding core level spectra (O 1s, Ti 2p, C 1s and S 2p from left to right) measured by XPS on the hybrid thin film are shown in Figure 24. The bottom spectra in black were obtained from the sputter cleaned Au substrate used in this experiment. The absence of strong O 1s and C 1s emissions indicates that the substrate is cleaned by Ar ion sputtering. The substrate is free of Ti, C and S and has a minor amount of residual surface contamination. As the deposition series begins, the intensities of O 1s, Ti 2p, C 1s and S 2p emissions increase with the increase of the amount of hybrid molecules as deposited. Shown from the O 1s spectrum measured after the first 1 mL deposition step, a main peak merges at 531 eV which is attributed to the O^{2-} group in the TiO_2 nanoparticles. In addition, a broad shoulder around 533 eV can be seen clearly in the following measurements. This line at higher binding energy level originates from the OH groups on the surface of the TiO_2 nanoparticles, and relates to the surface defects.

These defects are mostly composed of dangling bonds and vacancies [106]. However, the oxygen vacancy related Ti 2p emissions cannot be identified from the Ti 2p spectra in this experiment. The Ti 2p spectra as displaced in the second panel only shows one strong Ti $2p_{3/2}$ peak around 459 eV.

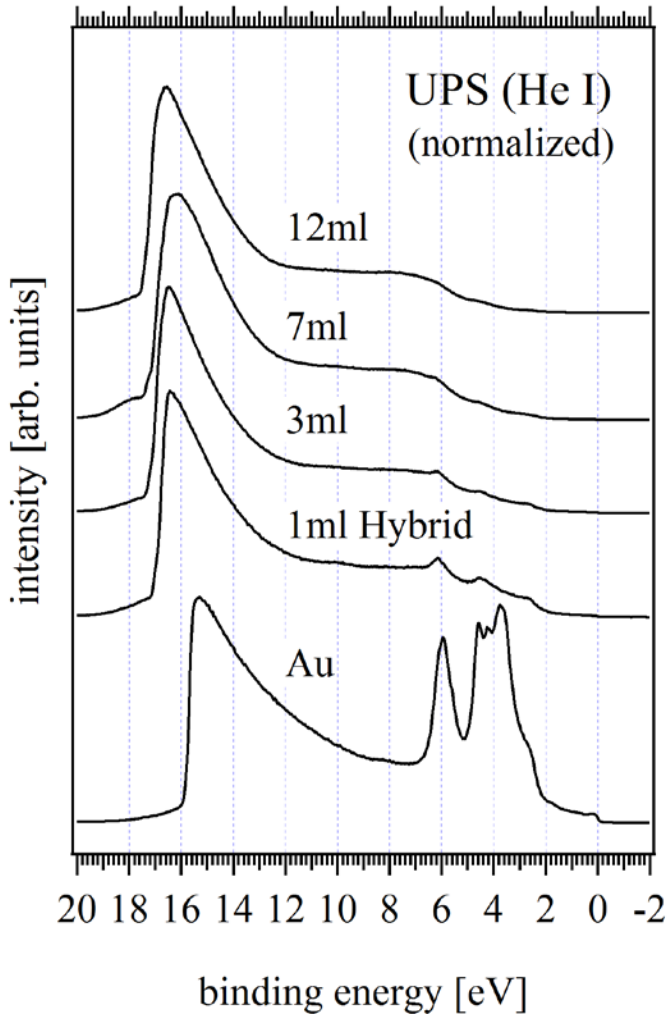

Figure 23: The UP-spectra of the hybrids measured before and after each deposition step. The hybrid molecules were deposited in four steps. (Reprinted (adapted) with permission from [103]. Copyright 2013 American Chemical Society)

The S 2p emissions in the right panel have a small signal to noise ratio since the stoichiometric ratio between S atoms and the other constituent atomic species is small. In combination with the small ionization cross section of S, an only weak signal can be measured. Thus, the lines measured after the final deposition step (12 mL) with relatively high intensity were used in the further evaluation of this interface. There are no band bending or strong charging effects are observed because no peak shifts are observed.

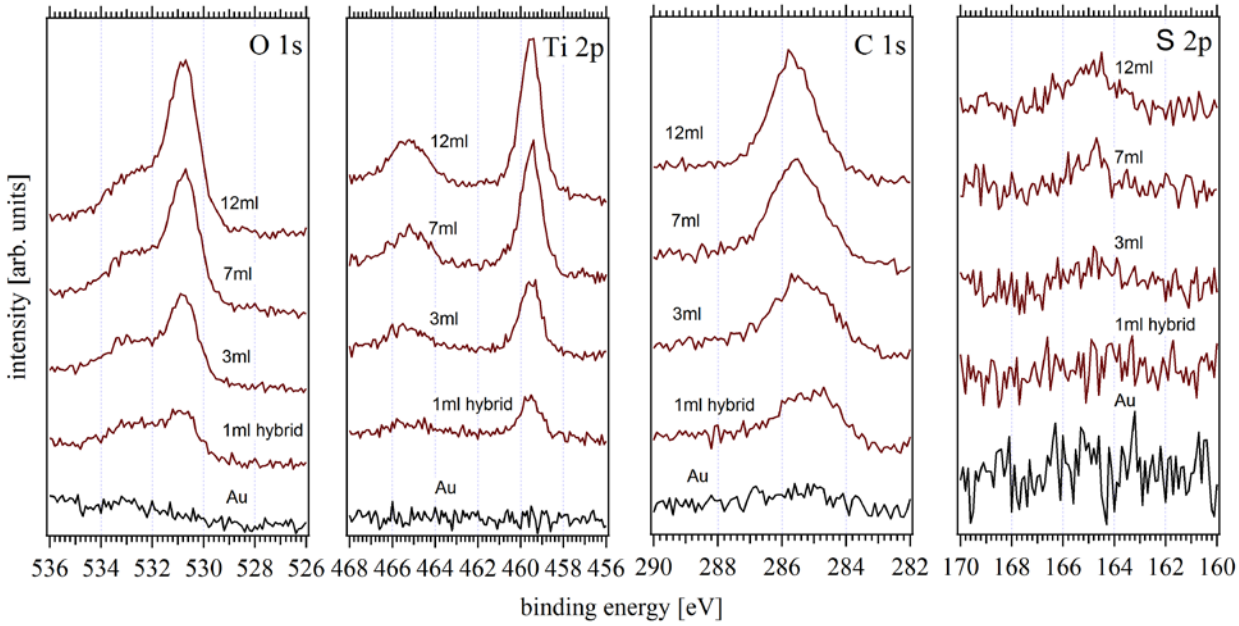

Figure 24: The core level lines of O 1s, Ti 2p, C 1s and S 2p from left to right measured by XPS for each deposition step of the oligothiophene-TiO_2 nanoparticle hybrids. (Reprinted (adapted) with permission from [103]. Copyright 2013 American Chemical Society)

3.3.4: Results of UV-vis and TEM Measurements

The results of UV-vis measurements on the TiO_2 nanoparticles and oligothiophene ligands are shown in Figure 24 which can be used to characterize their optical band/HOMO-LUMO gaps. By fitting a straight line into the absorption edge of the spectrum and determining

the intersection with X-axis, a band gap/HOMO-LUMO gap can be estimated. The estimated band gap of the TiO_2 nanoparticles is 3.45 eV which is slightly larger than a previously measured value [96]. But this deviation can be explained with the difference in nanoparticle size, since the band gap of nanoparticles strongly depends on their size. The HOMO-LUMO gap of the ligands was estimated to be 2.73 eV.

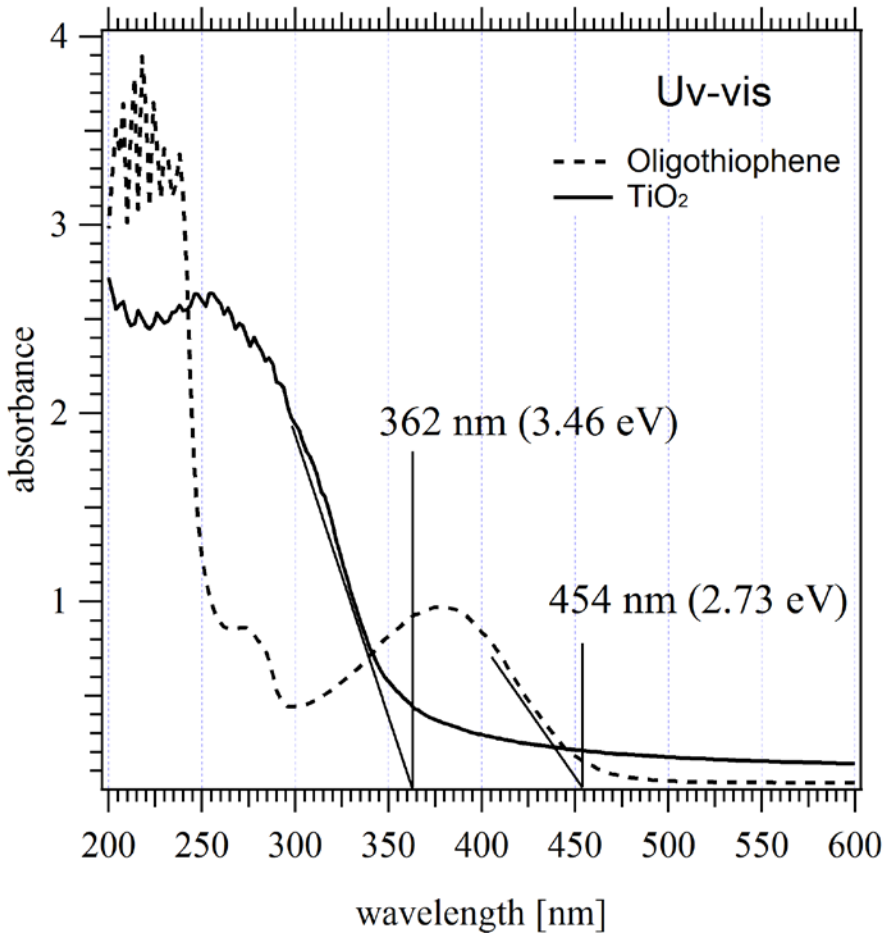

Figure 25: UV-vis absorption spectra of the TiO2 nanoparticles (solid line) and oligothiophene ligands (broken line). (Reprinted (adapted) with permission from [103]. Copyright 2013 American Chemical Society)

Figure 26 shows TEM images of the naked TiO_2 nanoparticles (A) and of the complete hybrid materials (B). Evaluation of the images yielded that the average diameter of the TiO_2 nanoparticles is about 24.9 nm while the mean size for the hybrids is about 25.1. The size distribution analysis based on the TEM images are shown in Figure 27. By randomly evaluating 30 particles from each image, the standard deviation is 2.7 nm for the naked TiO_2 nanoparticles and 2.6 nm for the hybrids. Therefore, hybridizing TiO_2 nanoparticles with oligothiophene ligands by covalent grafting does not seem to change the size distribution and shape of these nanoparticles significantly as is obvious from the similarity between the two pictures.

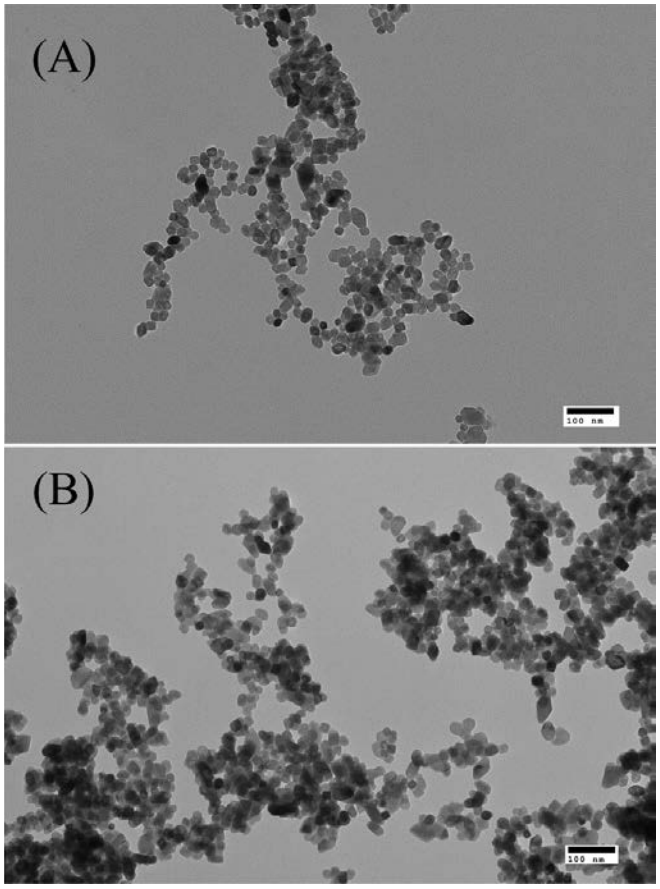

Figure 26: Transmission electron microscopy (TEM) images of pure TiO_2 nanoparticles (A) and oligothiophene-TiO_2 nanoparticle hybrids (B).

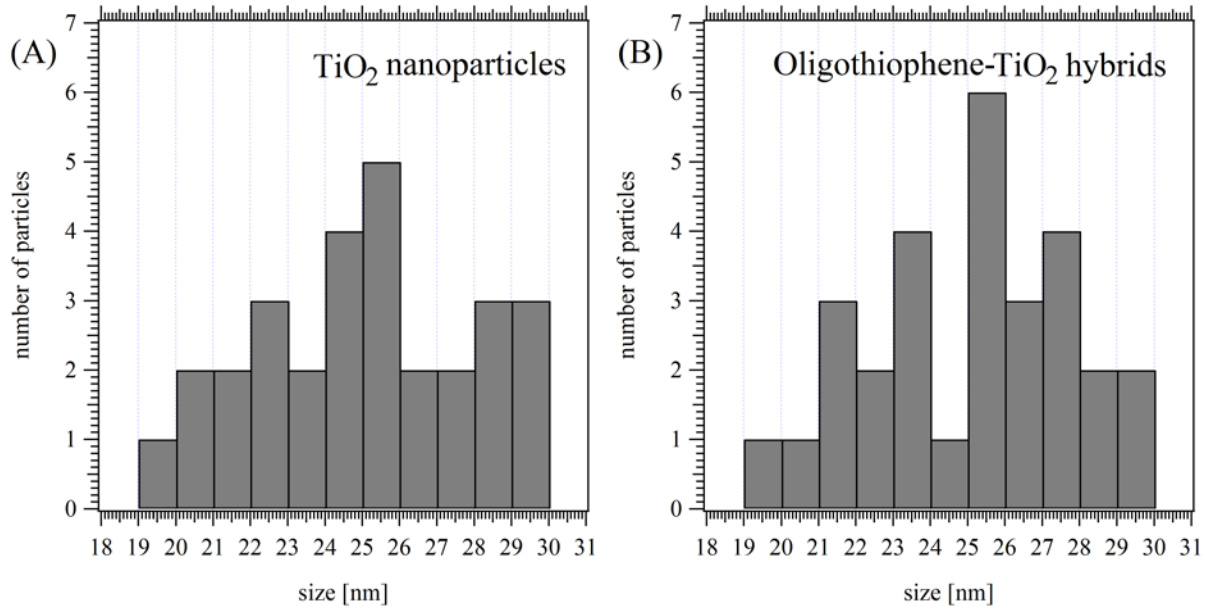

Figure 27: Analysis of size distribution of the naked TiO2 nanoparticles and the hybrids based on the TEM images.

3.4: Discussion

3.4.1: Determination of the Ionization Energy of the Pure TiO_2 Nanoparticles and the Oligothiophene Ligands

The discussion of the orbital alignment at the internal interface in the hybrid material requires the knowledge of the ionization energy of the two constituents. Work function and VBM/HOMO cutoffs are the two essential factors associated to the ionization energy which is referred as the difference between these two values. Figure 28 illustrates how to determine of the ionization energy for both constituents. The bottom panel is for the TiO_2 nanoparticles and the top panel is for oligothiophene ligands. The VBM of the TiO_2 nanoparticles was determined by the UPS measurements yielding a value of 3.50 eV. The LIXP-spectrum measured before the

UPS measurement was used to determine the work function. The axis unit of the secondary edge was converted from binding energy into kinetic energy by taking the energy of excited photons into account. The secondary edge cutoff was measured by fitting a straight line down to the axis and reading the axis intersection. Accordingly, the work function of the TiO_2 nanoparticles was determined to be 4.44 eV. Based on the obtained VBM and work function, the ionization energy of the TiO_2 nanoparticles was calculated to be 7.94 eV, as shown in the bottom panel in Figure 28. By applying the same determination process, the HOMO cutoff and the work function of the oligothiophene ligands were determined by the UPS measurement and the LIXPSa measurement. By utilizing the obtained results, the ionization energy of the oligothiophene ligands was determined as 6.60 eV.

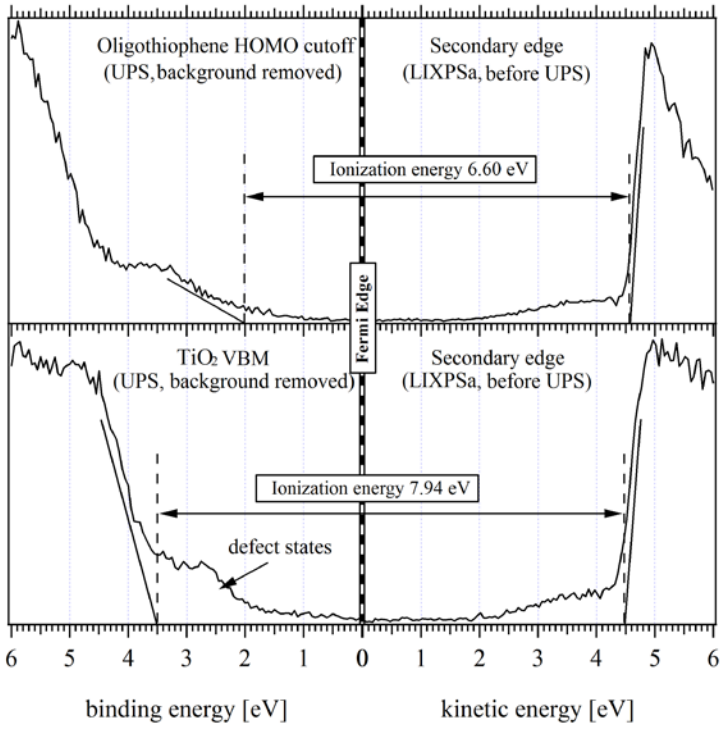

Figure 28: Determination of the ionization energy for the pure TiO_2 nanoparticles and the oligothiophene ligands. (Reprinted (adapted) with permission from [103]. Copyright 2013 American Chemical Society)

3.4.2: Determination of the Energy Difference between Core Levels and VBM/HOMO Cutoff

The hole injection barrier at the internal interface within the hybrid cannot be directly determined due to the superposition of the valence band emissions from TiO_2 and the HOMO emissions from oligothiophene ligands as discussed in the above section. This challenge can be circumvented through the use of core level emission lines in combination with the energy difference between core level and VBM or HOMO. The energy difference between the core level binding energy and the VBM/HOMO onset is a material constant and size dependent in nanoparticles. Figure 29 shows the Ti $2p_{(3/2)}$ core level line and the valence region. The Ti $2p_{(3/2)}$ core level line was fitted to yield a binding energy of 459.55 eV. As for the VBM, the value of 3.50 eV was obtained. By taking these two numbers, the energy difference was calculated to be 456.05 eV.

The defect states on the surface of the TiO_2 nanoparticles, as marked in the spectrum, were excluded from this calculation since they represent localized states within the band gap (see Figure 29). A similar procedure is applied to the ligands when it comes to determining the energy difference between the S 2p line and the HOMO cutoff, as shown in Figure 30. Because of the small ionization cross section of S atoms, the S 2p emission has a low signal to noise ratio as measured. This can be partially alleviated through the performance of a peak fit. The S 2p was fitted into a doublet peak following the rule of orbital splitting. It allowed the determination of the energy difference to be 162.01 eV. The accuracy of these values is approximately ±0.1 eV due to the resolution of XPS measurement.

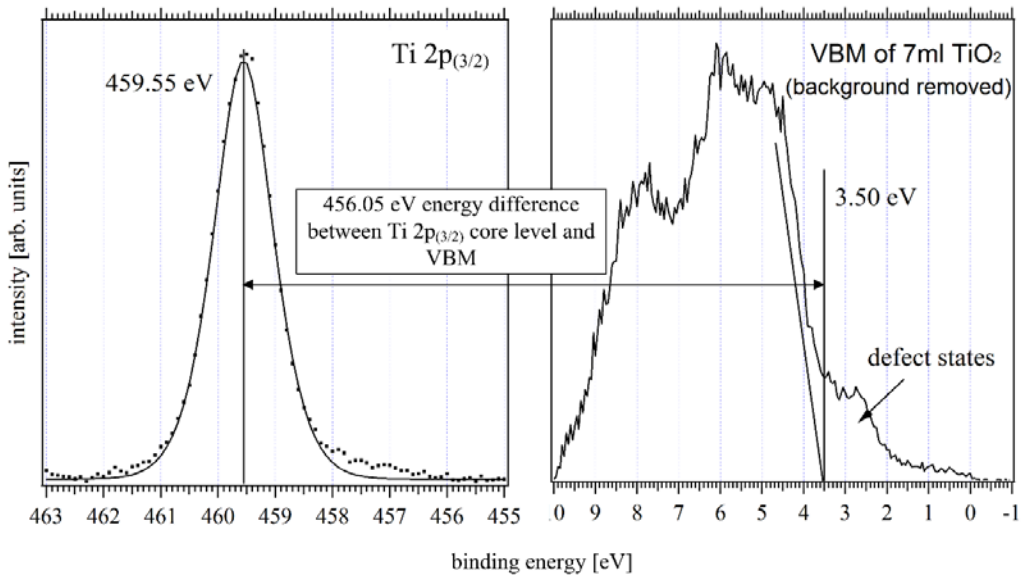

Figure 29: Determination of the energy difference between the Ti $2p_{(3/2)}$ core level and VBM. (Reprinted (adapted) with permission from [103]. Copyright 2013 American Chemical Society)

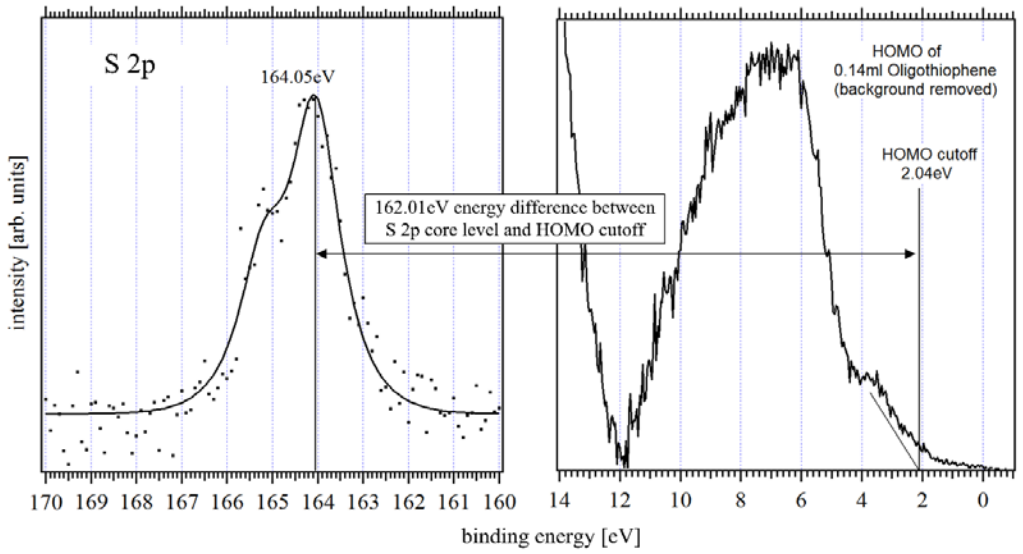

Figure 30: Determination of the energy difference between the S 2p and HOMO cutoff. (Reprinted (adapted) with permission from [103]. Copyright 2013 American Chemical Society)

3.4.3: Determination and Interpretation the Orbital Alignment at the Internal Interface in the Hybrid

The hole injection barrier at the internal interface can be determined by using the core level binding energies of the Ti $2p_{(3/2)}$ peak and the S 2p peak measured from the hybrid. By using the energy difference determined in section 3.4.2 and the Ti $2p_{(3/2)}$ binding energy measured in section 3.3.3, the VBM of the TiO_2 nanoparticles in the hybrid was determined to be 3.48 eV. This value is the same as the VBM of the pure TiO_2 nanoparticles film (3.50 eV) within the error margin. The HOMO cutoff of the oligothiophene ligands anchored on the surface of TiO_2 nanoparticles was determined to be 2.75 eV by subtracting the core level to HOMO cutoff energy difference (162.01 eV) from the S 2p binding energy (164.76 eV) measured in section 3.3.3. In comparison to the pure ligands, the S 2p of the hybrid is located at the higher binding energy level. This indicates that a dipole originating from the covalent attachment of the ligands shifted their energy levels to a lower energy level compared to the pure material.

Figure 31 shows the orbital alignment at the oligothiophene/TiO_2 interface within the hybrid materials. The hole injection barrier Φ_h was determined to be 0.73 eV from the offset between the VBM of the TiO_2 nanoparticles and the HOMO cutoff of the oligothiophene ligands. The electron injection barrier Φ_e was estimated to be 0 eV by subtracting the hole injection barrier and the VBM of the TiO_2 nanoparticles from the HOMO-LUMO gap of the oligothiophene ligands. It suggests that there is no significant barrier to electron transfer across this internal interface. The internal interface dipole eD was determined from the difference between the work function of the TiO_2 nanoparticles and the oligothiophene ligands. The work function of each constituent was obtained by subtracting the VBM/HOMO cutoff from the

ionization energy. The calculation yielded a result of 4.46 eV for the nanoparticles and 3.85 eV for the ligands. Therefore, the so-determined interface dipole has a value of 0.61 eV.

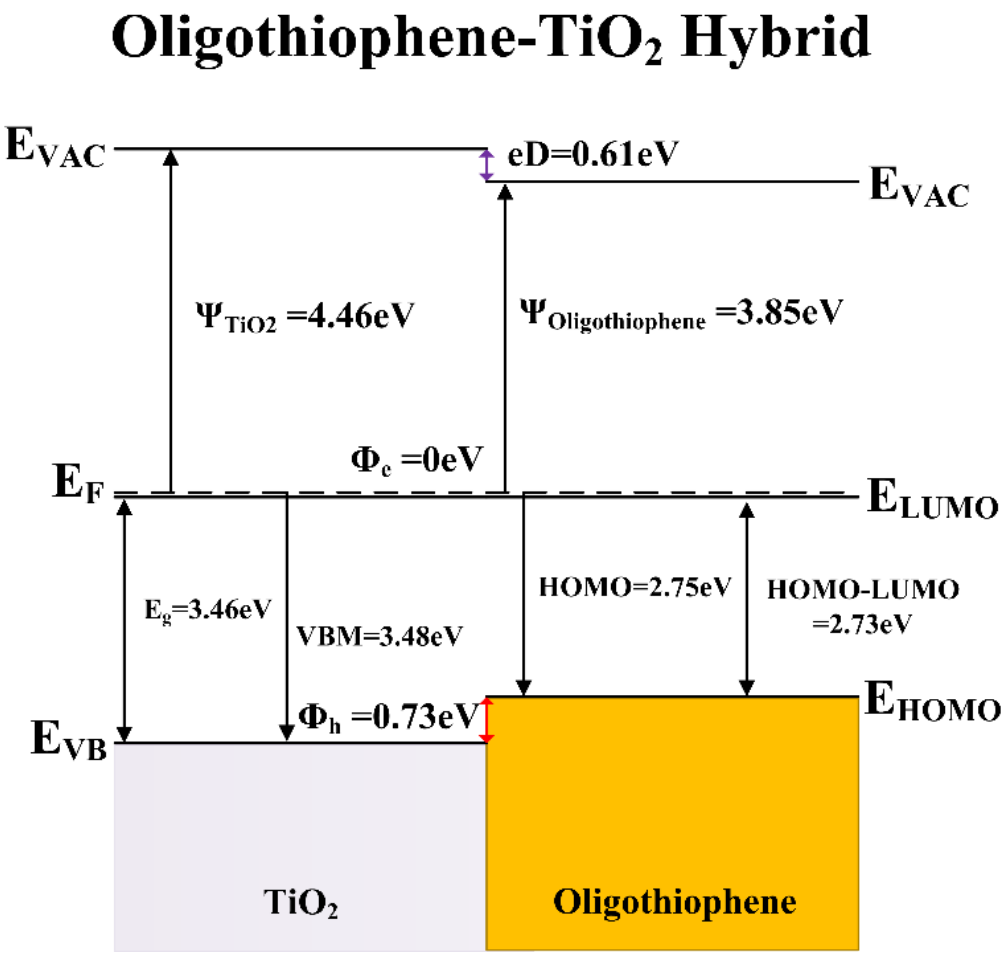

Figure 31: Schematic of the orbital alignment at the internal interface in the oligothiophene-TiO_2 (covalently bonded) nanoparticle hybrids. (Reprinted (adapted) with permission from [103]. Copyright 2013 American Chemical Society)

The obtained results show that the Fermi level appears to be located at the edge of the CB/LUMO in the hybrid. It is well established that surface defects especially oxygen vacancies result in n type of doping to the surface of TiO_2. It gives rise to a surface potential which has strong influences on the charge distribution near the surface. In materials within nano-scale, this

effect is further enhanced due to the large surface to volume ratio. As a result, a highly doped environment near the surface is generated while the nanoparticles become degenerated [107, 108]. This may explain why the Fermi level is slightly above the conduction bands in the presented results. This interpretation is supported by Liu et al. who observed degeneracy on the surface of TiO_2 nanoparticles in their research [102]. Similar phenomena are also observed in other oxide based materials in which surface defects play a significant role in their electronic structures. As for ZnO, Göpel and Lampe concluded that surface defect density can increase the surface conductivity dramatically [109]. Carreras et al. confirmed that defects can cause degeneracy in Zn doped ITO films [110]. Similarly, it was found that defects created by sputtering can also cause surface degeneracy [111].

The presented orbital alignment shows an internal interface dipole caused by covalent bonding. Similar effects in different hybrid systems were also observed and reported by other research groups. Liang et al. synthesized a hybrid material with a structure of PPV-CdSe using a layer-by-layer approach which enabled covalent crosslinking between PPV and CdSe. In their results, the C 1s emission from the amide group in the hybrid shifted to higher binding energy, which suggested that the PPV ligands were covalently bonded with the CdSe nanoparticles [112]. The PPV-CdSe hybrid system is comparable to the oligothiophene-TiO_2 system because the PPV ligands act as electron donors and the CdSe nanoparticles act as electron acceptors. Thus, the shift of the C 1s line in their experiments is consistent with the shift of S 2p line observed in this dissertation. In another research group, Xiong et al. also reported a shift of the HOMO for polyaniline in PANI-TiO_2 hybrids. In their work, it was observed that the PANI tends to oxidize at a lower potential as a result of the decrease in the energy of its HOMO since the PANI ligands acted as electron donors and the TiO_2 nanoparticles as acceptors [113].

In order to understand the interaction between the TiO_2 nanoparticles and the oligothiophene ligands through covalently bonding, Hard Soft Acid Base (HSAB) principle must be introduced and discussed [114]. According to this principle, a hard acid intends to bond with a hard base through ionic bonds while a soft acid prefers to bond with a soft base through covalent bonds. TiO_2 nanoparticles, consisting of metal ions and oxygen ions, are categorized as a typical Lewis acid capable of accepting electrons. Oligothiophene ligands can be classified as a Lewis base donating electrons to the Lewis acid in the reaction. In this case, the ligands donate electrons to the nanoparticles during the hybridizing reaction. As for a Lewis base molecule, donating electrons lowers the oxidation potential, shifting the HOMO to a lower energy state. This is in agreement with the behavior of the oligothiophene ligands as observed in this dissertation.

More specifically, the dipole observed at the internal interface within the hybrid is a direct result of the covalent bonding at the interface between a Ti+ vacancy and the deprotonated hydroxyl group O- of the carboxylic acid terminus of the oligothiophene. The electronegativity difference between Ti (1.54) and O (3.44) suggests that this hybridizing reaction results in an electron transfer from the carboxylic group to the Ti+ defective site in the nanoparticle surface. The net result of this process is a lowering of the electronic system on the oligothiophene side and an increase of the energy on the nanoparticle side (see Figure 32). This process is further amplified since the carboxyl group draws some density of electrons from the thiophene rings, resulting in a molecular dipole pointing from the thiophene rings towards the carboxyl group [115]. This further enhances the electron transfer from the carboxyl group into the TiO_2 nanoparticles. However, the VBM of the TiO_2 nanoparticles stays at the same energy level after the hybridizing reaction. This unpredicted result is associated with the particular characteristic of

the presented hybrid material. The anchoring S atoms have a similar electronegativity as O atoms. When they replace O atoms to bond with Ti atoms on the surface, the energy level of the bonded Ti is mostly to be altered within the measurement resolution.

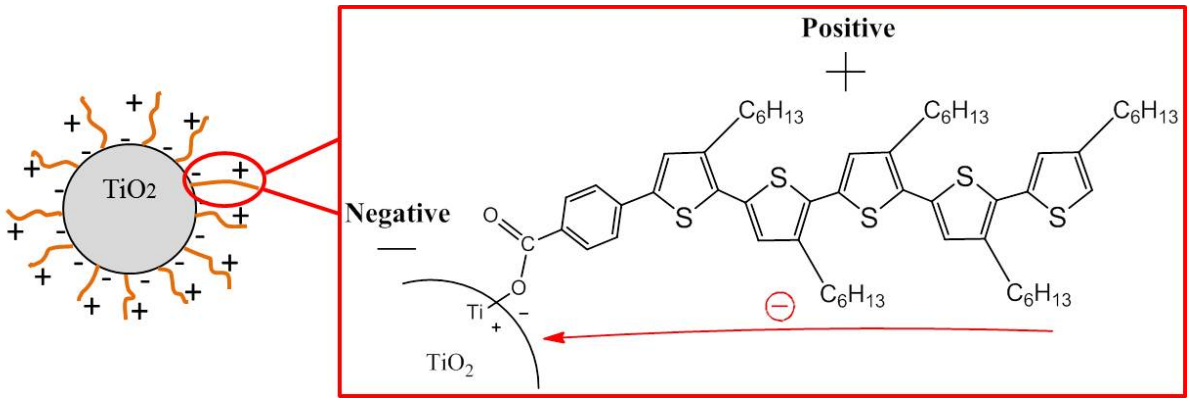

Figure 32: Schematics of the oligothiophene-TiO_2 nanoparticle hybrids and the internal interface dipole. (Reprinted (adapted) with permission from [103]. Copyright 2013 American Chemical Society)

CHAPTER 4: ORBITAL ALIGNMENTS AT THE INTERNAL INTERFACE OF THE ARYLTHIOL-FUNCTIONIZED CADMIUM SELENIDE HYBRIDS AND THE PHYSISORBED INTERFACE

In this chapter, the orbital alignment at the internal interface of arylthiol functionized Cadmium Selenide (ArS-CdSe) hybrid materials was studied through the PES based characterization protocol. A physisorbed interface between the arylthiol (ArSH) ligands and the CdSe nanoparticles was also investigated for comparison. This interface was created by multi-step in-vacuum thin film deposition procedure enabling surface characterization after each deposition step. All materials were deposited using an electrospray deposition setup outfitted to a multifunctional high vacuum system in which XPS and UPS measurements can be performed immediately after the deposition without exposure to the ambient atmosphere. Transmission electron microscopy (TEM) was used to confirm the morphology and particle size of the deposited materials. Ultraviolet-visible (UV-vis) spectroscopy was used to estimate the optical band gap of the CdSe nanoparticles and the HOMO-LUMO gap of the ArSH ligands. The experiments allowed the conclusion that hybridization through covalent bonds attributes to an orbital realignment between the CdSe nanoparticles and the ArSH ligands within the hybrid in comparison to the physisorbed interface.

4.1: Introduction

Cadmium selenide (CdSe) nanoparticles are one of the most promising candidates for novel hybrid photovoltaic devices and light-emitting diodes (LEDs). It possesses a unique electronic structure and can have various absorption regions [45, 116-118]. Current investigated inorganic/organic hybrid devices consist of inorganic nanocrystalline materials and conductive organic polymers that are fabricated by physical blending methods [119, 120]. These types of devices, however, have relatively low light conversion efficiency in comparison to organic-organic based devices and conventional thin films based devices [121, 122]. One of the major constraints is the properties of organic capping ligands. These ligands, such as tri-n-octylphosphine oxide (TOPO) and pyridine are bonded to the surface of CdSe nanoparticles [123, 124]. The presence of such organic capping ligands is required in the synthesis process of these nanoparticles in order to control the growth rate and passivate the surface to minimize surface defects caused by dangling bonds. Furthermore, by capping CdSe nanoparticles with organic ligands, a miscibility and solution processability can be obtained to meet the requirement of low cost and fast printing deposition techniques. Nevertheless, the mobility of electrons in traditional capping ligands is so low that it inhibits the charge transfer across the interface [118]. The physisorbed interface impedes exciton dissociation efficiency due to the short diffusion length of excitons and unfavorable hetero-junction band offsets [125].

To date, direct attachment of π-conjugated capping ligands with better electron mobility and suitable band structure onto CdSe nanoparticles is motivated. The current research focuses on π-conjugated thiol molecules which have proven to be a suitable capping material with good PL quenching and photoelectric properties attributing the existence of aromatic π-electrons [126]. Furthermore, thiol groups are seen commonly in conductive polymers, such as P3HT [51].

Studies also show good results creating inorganic-polymer hybrid nanoparticles with sulfur as anchors that attach to the surface of CdSe nanoparticles [127]. Therefore, novel hybrid structures with better performance capping materials can be developed and studied. The properties of the hetero-junction within the novel hybrid materials dominate the excitons-dissociation and charge-transfer process. It is thus crucial to understand the orbital alignment at the internal interface. The capping material studied in this chapter is arylthiol (ArSH) which has good charge transport properties, simple chemical structure and a thiol-anchor group. They are grafted onto the surface of CdSe nanoparticles through one pot synthesis method.

In this chapter, the orbital alignment at the ArSH/CdSe interface with and without covalent bonding was characterized and discussed. X-ray photoemission spectroscopy (XPS) measurements were performed to determine the core-level binding energies of different species in sample molecules. Ultraviolet photoemission spectroscopy (UPS) measurements were carried out to obtain the VB/HOMO emissions. The secondary electron cutoff measured by the low intensity X-ray photoemission spectroscopy (LIXPS) yielded the true work function of the sample without the influence of charging or other surface modification artifacts. However, like a typical hybrid material, the superposition of photoemission from inorganic nanoparticles with those from organic ligands gives rise to a challenge to obtain the orbital line-up directly. The characterization protocol developed in chapter 3 was applied to investigate the internal interface within the ArS-CdSe hybrid [103]. The results show that hybridization contributes to the shift of the electronic system for both hybrid constituents resulting in different electronic structures in comparison to the electronic structure at the physisorbed interface.

4.2: Experimental

Glass slides coated with 100 nm Au thin films on top of a Ti film were purchased from EMF Corp. (Itchaca, NY) and used as substrates in the experiment of creating the physisorbed interface. The Au substrate was sputter cleaned with Ar+ ions (SPECS IQE 11/35 ion source) at 5 keV for approximately 40 minutes prior to depositions. Highly ordered pyrolytic graphite (HOPG) substrates were used in the characterization of the ArS-CdSe hybrid materials as well as the ArSH ligands. Several top layers of HOPG were removed in the glovebox in order to create a pristine surface. Electrical contact between the substrate surface and sample holder was ensured to prevent surface charging.

As discussed in the previous chapter, characterization of internal interface within hybrid materials requires the information of each constituent. However, pure CdSe nanoparticles barely have dissolubility in any solvent and tend to be oxidized easily. As a result, it is difficult to make CdSe thin films directly out of pure CdSe nanoparticles. The CdSe nanoparticles used in this dissertation were capped with pyridine ligands. The pyridine molecules capped around the CdSe nanoparticles are unstable under a ultra-high vacuum condition which can provide ligand-free CdSe thin film for characterization after the deposition in vacuum [128]. Since the CdSe is already in vacuum after the deposition, the oxidation problem can be solved. The pyridine capped CdSe nanoparticles, ArSH ligands and ArS-CdSe hybrid material were dissolved in toluene at a concentration of 1 mg/mL. The synthesis of the ArSH ligands and the hybridization of the ArS-CdSe hybrid material were accomplished by Dr. Luscombe's group at the University of Washington. More details can be found in the previous publication [129]. The solutions of the materials under investigation were injected into the deposition chamber at a rate of 4 mL/h. A

high bias voltage (-2000 V) was applied between the syringe needle tip and the targeting substrate as required to perform electrospray deposition.

The characterization of the internal interface and the physisorbed interface was counted on three main experiments. In the first experiment, a physisorbed interface between the ArSH ligands and the CdSe nanoparticles was created through multi-step in-vacuum depositions. Initially, 1.2 mL solution containing pyridine-capped CdSe nanoparticles was injected into the chamber to create a pure CdSe nanoparticle thin film on a clean Au substrate. Followed by a series of PES measurements, the electronic information of the CdSe nanoparticles was obtained. Subsequently, ArSH ligands were deposited onto the surface of the CdSe film in several steps by the same method. The sample surface was characterized after each deposition step. The second experiment was carried out to study the ArS-CdSe hybrid materials which were deposited onto a HOPG substrate. The valence bands and core level emissions were investigated by PES after the deposition. In the third experiment, the ArSH ligands were deposited on a HOPG substrate layer by layer in several steps followed by PES measurements after each step.

After each deposition, the sample was transferred from the deposition chamber to the analyzing chamber for characterization with low intensity XPS (LIXPS) (Mg Kα, 1253.6 eV, standby mode: 0.1 mA emission current), UPS (He I, 21.2182 eV), and XPS (Mg Kα, 1253.6 eV, 20 mA emission current) in sequence. In LIXPS measurements, a magnitude lower photon flux is used to prevent sample charging artifacts allowing to obtain the true work function of the sample. In order to separate sample spectra from the analyzer spectral a -10 V bias voltage was applied to the sample. A SPECS Phoibos 100 hemispherical analyzer was used for the analysis of photoelectrons and calibrated to yield a standard Cu $2p_{(3/2)}$ line at 932.66 eV and a Cu $3p_{(3/2)}$ line at 75.13 eV.

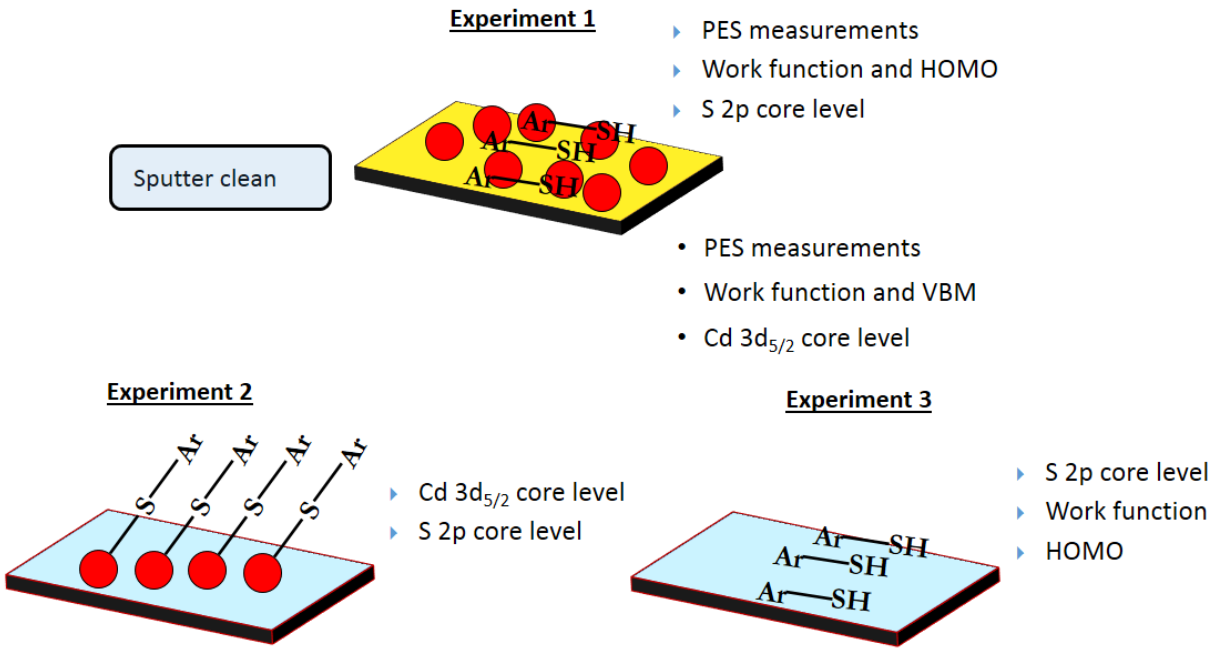

Figure 33: Schematic illustration of experimental design to determine the orbital alignment at the internal interface in ArS-CdSe hybrids and the physisorbed ArS/CdSe interface.

In addition to the PES experiments, the morphology and the particle size of the pyr-CdSe nanoparticles and the ArS-CdSe hybrid materials were confirmed by TEM. The TEM images were taken with a FEI Morgagni electron microscope operating under a 60 kV accelerating voltage. The UV-vis measurements were carried out on a Thuramed T60 UV-vis spectrometer in the estimation of the optical band gap of the CdSe nanoparticles and the HOMO-LUMO gap of the ArSH ligands. The data obtained from the PES and UV-vis measurements were further analyzed using the Igor Pro software.

4.3: Results

The experiments described above are designed to measure the charge injection barriers and the dipoles at the internal interface within the ArS-CdSe hybrid materials as well as the ArSH/CdSe physisorbed interface. The electronic structure characterization of the CdSe nanoparticles, the ArSH ligands and the ArS-CdSe hybrid materials are shown in the following sections, respectively.

4.3.1: Characterization of the Electronic Structure of the CdSe Nanoparticles and the ArSH/CdSe Physisorbed Interface

In this section, an ArSH/CdSe physisorbed interface was created by depositing a thin film of ArSH ligands in four steps on top of an initially deposited CdSe thin film. Figure 34 shows the LIXP- and UP-spectra of the sample before the deposition and after each deposition step during this experiment. The center panel shows the complete UP-spectra, and the side panels show the normalized secondary edge (left) measured by LIXPS and the valence bands/HOMO region after background subtraction (right). The bottom spectra in blue are expected for a clean Au surface after *in-situ* sputtering for 40 min. Clear features originating from the valence bands can be identified clearly from 2 to 8 eV. The Fermi edge is also shown at 0 eV. After deposition of the CdSe nanoparticles, these features are suppressed and replaced by those from the valence bands of the CdSe nanoparticles. In the consecutive four-step experiments, the CdSe features are suppressed and replaced by the emissions from the HOMO of the deposited ArSH ligands.

The secondary edge measured by LIXPSa contains important information about the sample work function. The work function was obtained by subtracting the binding energy of the secondary edge cutoff from the excitation energy of incident photons (21.21 eV). The 0.1 eV analyzer broadening factor was also considered in the determination process. As after the

deposition of CdSe nanoparticles, the secondary cutoff was measured to be at 17.2 eV which corresponds to a work function of 4.1 eV. The work function of the ArSH ligands on top of the CdSe film was determined to be 3.7 eV, accordingly.

The full UP-spectra provide a direct view of valence bands features. As the amount of the ArSH ligands on top of the CdSe film increases, the UP-spectra evolve accordingly as illustrated in the center panel of Figure 34. Broadening of the secondary region was observed after the 0.30 mL deposition step, shown from the top spectrum in the center panel. This indicates that the presence of charging artifacts has non-neglectable influences on the measured spectra. The HOMO/VB emission evolves along with the deposition steps as expected. After the first 0.02 mL ligands deposition, a clear feature around 3.6 eV arises, and the main feature around 7 eV shifts to a higher binding energy level. The presence of charging artifacts observed after the last deposition step (0.30 mL) significantly impacts the HOMO/VB regions. As seen from the top spectrum in the right panel, the feature around 3.5 eV and the main feature around 7.5 eV become indistinguishable compared to the spectrum obtained from the previous 0.14 mL deposition due to the broadening effects caused by the charging artifacts. Thus, the data used in the following discussion were derived from the measurement after the 0.14 mL deposition which was free of charging artifacts. The valence band maximum (VBM) of the CdSe nanoparticles and the HOMO cutoff of ArSH ligands were obtained through the determination of the emission onset of the UP-spectra. The VBM of the CdSe nanoparticle thin film was determined to be 2.1 eV, and the HOMO cutoff of the ArSH ligands was 2.8 eV.

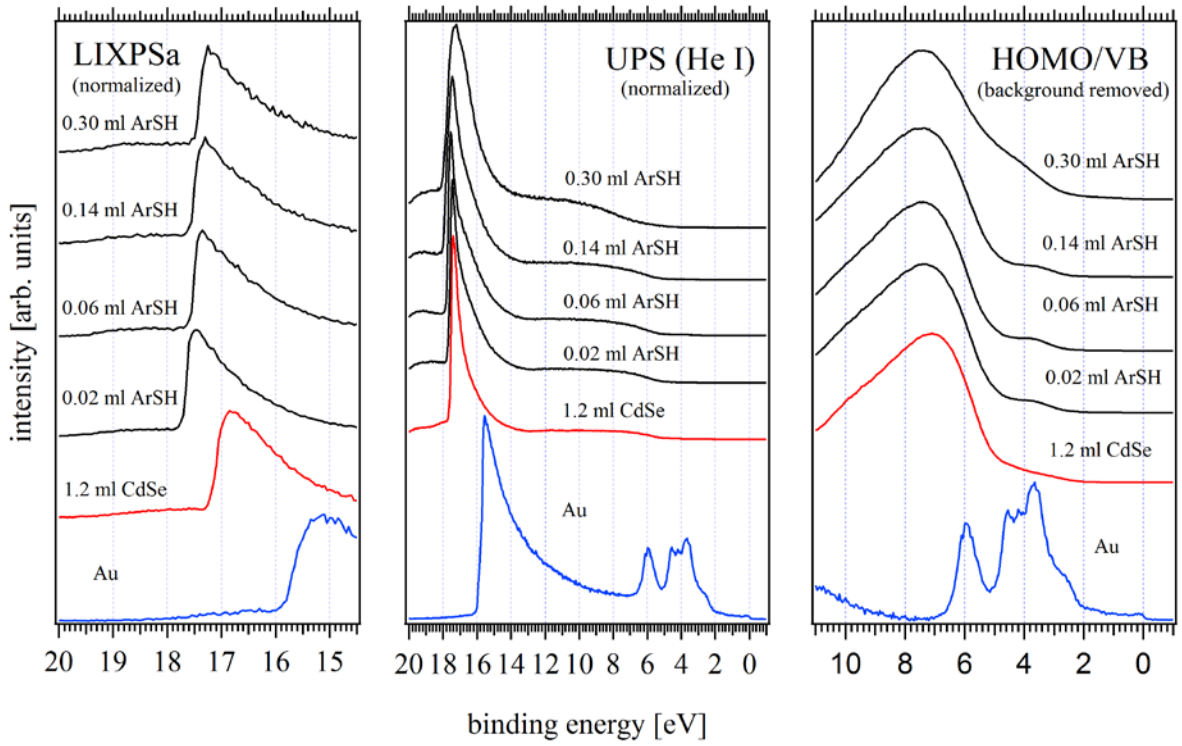

Figure 34: LIXP- and UP-spectra measured after each experimental step. The bottom spectra in blue were measured on a sputter cleaned Au substrate. The spectra in red were obtained from the CdSe thin film after 1.2 mL deposition step. The spectra in black were obtained from a series of ArSH ligands deposition.

The Cd 3d and Se 3d core level lines measured after each experimental step are shown in Figure 35. The bottom spectra in blue correspond to the Au substrate before the sequential deposition started. The absence of Cd 3d and Se 3d lines validates that the substrate is Cd and Se free initially. After the deposition of 1.2 mL CdSe nanoparticles, strong Cd 3d and Se 3d lines appear in the spectra as a result of the formation of the CdSe thin film on the substrate. The binding energy of the Cd 3d line was measured and used to determine the electronic structure for the hybrid materials in the discussion section. The subsequent spectra were obtained from the

measurement of the deposition series of the ArSH ligands. As shown in Figure 35, the Cd 3d and Se 3d lines attenuate gradually as the amount of the ArSH ligands increases. This indicates that a physisorbed interface between the CdSe nanoparticles and ArSH ligands has been created.

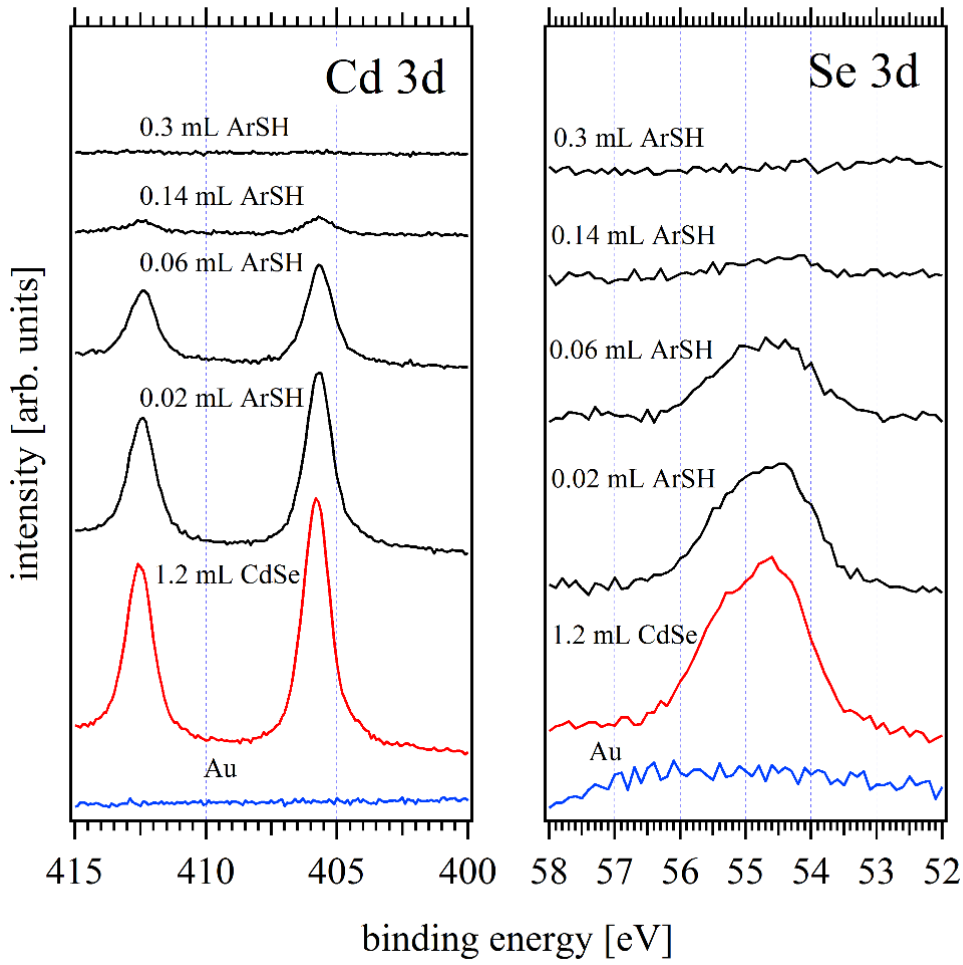

Figure 35: XPS spectra of Cd 3d and Se 3d core level emissions measured before and after each deposition step. The blue spectra was measured before the deposition from a clean Au substrate. The red spectra were obtained after the first deposition of 1.2 mL CdSe nanoparticles. The black spectra were measured after each deposition step of the ArSH ligands.

4.3.2: Characterization of the Electronic Structure of the ArSH Ligands

In order to characterize the electronic structure of the ArSH ligands, a HOPG substrate with a pristine surface was prepared and characterized before the deposition. Figure 36 shows the LIXP- and UP-spectra measured before and after each deposition step in this experiment. The left panel shows the normalized secondary edge measured by LIXPS during the experiment. The center panel shows the full UP-spectra obtained from each step. The panel on right side shows the magnified UP-spectra near the Fermi level after normalizing and background subtraction. The typical emissions expected for a pristine HOPG surface prepared in the glove box are shown in green. The signature emission of HOPG around 13.5 eV can be seen clearly from the full UP-spectrum. The valence band structure also can be seen clearly from 0 to 12 eV in the panel on right side. These features are suppressed and finally replaced by the features related to the HOMO emissions of the ArSH molecule after the first 0.02 mL deposition.

To be more specific, there are two main features of the ArSH HOMO. One is at 3.5 eV, and the other one is at 7.5 eV. After the last deposition step, a shift and broadening of the secondary edge were observed as shown from the top spectrum in the center panel of Figure 36, indicating the appearance of charging artifacts encountered during UV radiation exposure. The charging artifacts gave rise to a shift and broadening of the HOMO region as well, which can be seen clearly from the top spectrum in the right panel of Figure 36. Therefore, the data measured from the 0.08 mL experimental step was used in the further analysis. The work function and HOMO cutoff of the ArSH ligands on the HOPG substrate were determined to be 4.3 eV and 2.2 eV, respectively.

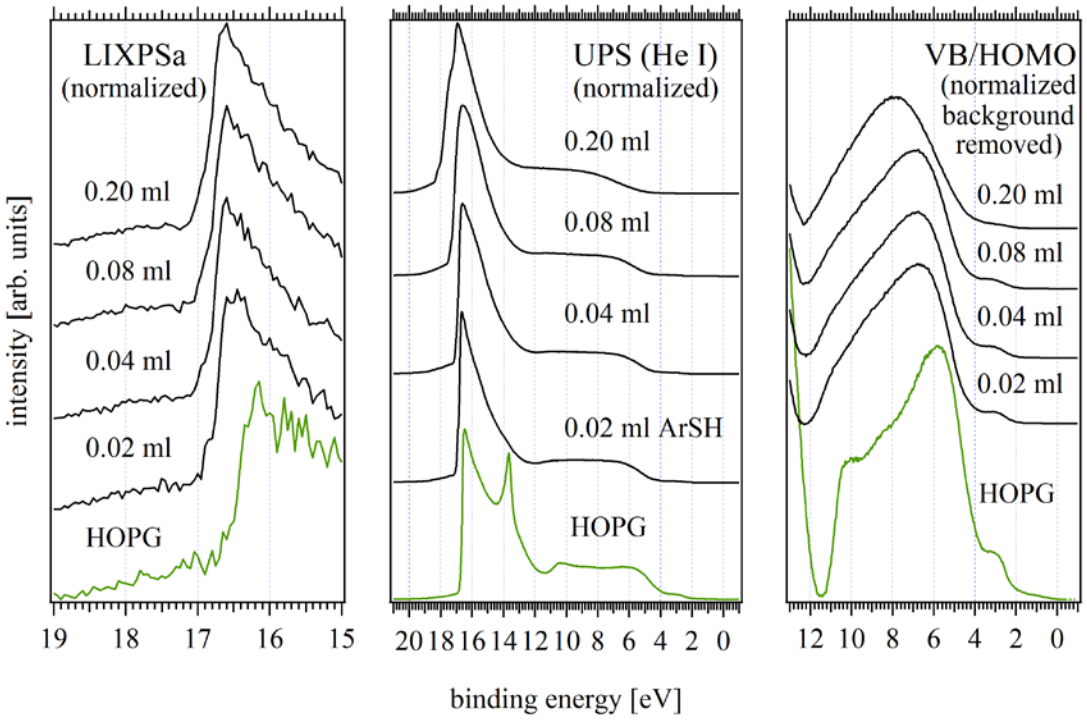

Figure 36: LIXP- and UP-spectra of each experimental step as the deposition of the ArSH ligands on top of a pristine HOPG surface. The deposition started at 0.02 mL and ended at 0.20 mL in total.

Figure 37 shows XPS core level lines matching the above UP-spectra sequence of each experimental step. The O 1s, C 1s, and S 2p lines are shown from left to right. Initially, S 2p emissions are absent in the spectrum measured on the HOPG substrate. This indicates that there is no sulfur on the surface before the deposition started. A small O 1s peak can be seen due to the existence of an insignificant amount of contaminants on the surface. A strong C 1s emission line is located at 284.5 eV as expected for a HOPG substrate. The intensity of the C 1s decreases in the deposition series as a result of the absorption of the electrons emitted from the HOPG in the of ArSH film. Meanwhile, the ligands layer related O 1s and S 2p lines show an increasing

intensity as more ligands were deposited on the surface. Since the sample surface suffered severe charging effects after the last deposition step, the binding energy of S 2p core level line measured from 0.08 mL step was used in the further discussion.

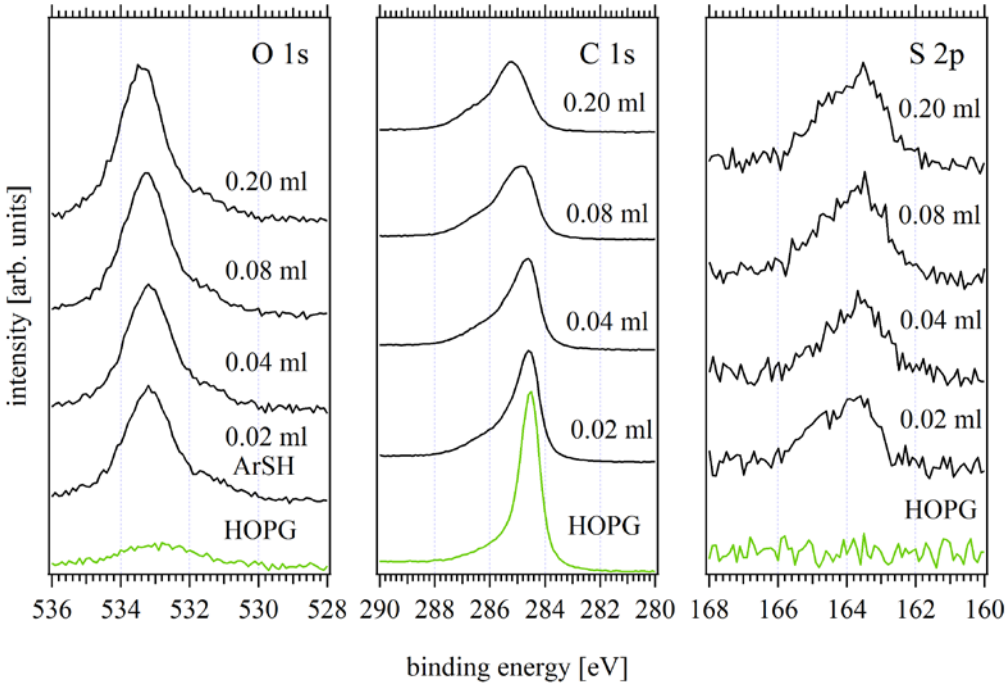

Figure 37: XPS spectra of O 1s, C 1s and S 2p core level lines measured for each experimental step in the ArSH ligands characterization experiment.

4.3.3: Characterization of the ArS-CdSe Hybrid Materials

Figure 38 shows the UP-spectra measured to characterize the ArS-CdSe hybrid materials. The hybrid was deposited on an HOPG substrate in seven steps. The bottom spectrum in green is a typical UP-spectrum of HOPG surface with signature emissions, which are gradually attenuated and then completely disappear after the third step where the emissions from the hybrid materials are dominant. The measured hybrid emissions are composed of photoelectrons from

both constituents. The interface dipole and the band offsets at the internal interface within the hybrid materials cannot be directly determined from the UP-spectra as measured. The species core level emissions of the hybrid materials are needed to solve this problem.

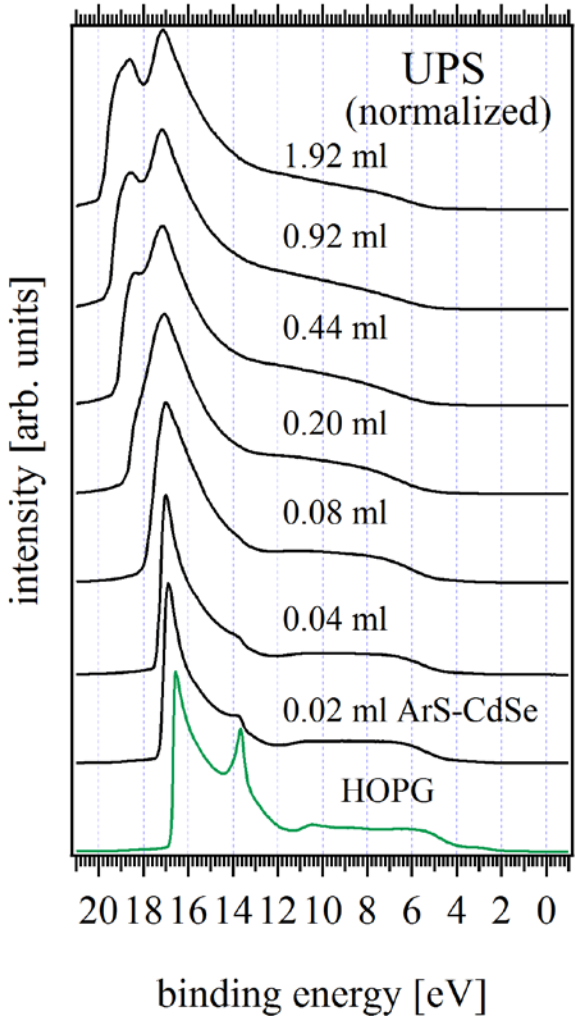

Figure 38: UP-spectra of each deposition step of the ArS-CdSe hybrid materials. The deposition started with injecting 0.02 mL solution and ended at 1.92 mL solution in total. The features related to HOPG emissions are disappeared after the 0.08 mL step.

Besides the UP-spectra measured before and after each step, the corresponding O 1s, Cd 3d, C 1s and S 2p core level lines were also measured by XPS as shown in Figure 39 from left to right. The green spectra in each panel are corresponding to the core level emissions measured from a pristine HOPG substrate. A small O 1s peak can be seen. This is most likely related to residual contamination on the HOPG surface. A similar contamination related O 1s emission was also observed in the experiment described in section 4.3.2. The surface of the HOPG substrate is Cd and S free, as indicated by the absence of Cd 3d and S 2p emission lines. Also for a typical HOPG substrate, a strong C 1s emission can be seen around 284.5 eV.

As the deposition series began, the O 1s, Cd 3d and S 2p emissions evolved as a function of the deposited amount. No significant changes of the O 1s were observed until the fourth deposition was carried out (in total 0.20 mL solution was injected). The Cd 3d emissions were barely seen in the first two depositions. In the following deposition steps, the intensity of Cd 3d was increasing. The strong C 1s emission from the HOPG substrate at 284.5 eV can be identified in all experimental steps. After the third deposition (0.08 mL in total), a peak at 285.8 eV was observed. This peak is associated with the carbon atoms in the hybrid materials. As the injected solution reached 0.20 mL in total, it became dominant in the C 1s spectra. The S 2p emissions have a small signal to noise ratio since the stoichiometric ratio between S atoms and the other constituent atomic species is small as well as the cross section of S atoms is small. This explains why the S 2p peak is still barely seen when 0.20 mL solution was injected. A relatively strong S 2p peak was obtained after the last deposition step, and its binding energy was used in the further evaluation of this interface.

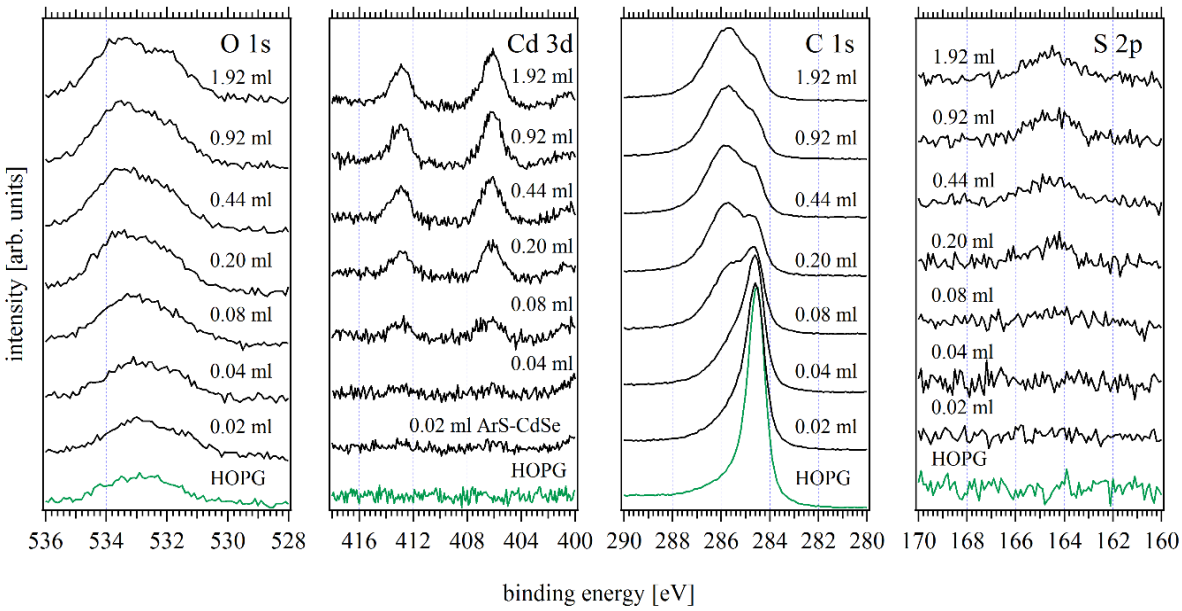

Figure 39: The XPS core level lines (O 1s, Cd 3d, C 1s and S 2p from left to right) measured from each deposition step of the ArS-CdSe hybrid materials. The green spectra were obtained from a pristine HOPG substrate.

4.3.4: TEM Images of the Pyr-CdSe Nanoparticles and the ArS-CdSe Hybrids

The properties of nanoparticles, including the electronic structure, highly depend on their size and shape due to quantum confinement effects [130, 131]. Figure 40 shows the TEM images of the ArS-CdSe hybrid materials on the left side and the pyridine capped CdSe nanoparticles on the right side. The average size of pyridine capped CdSe nanoparticles is around 3.1 nm with a well-defined spherical shape and a standard deviation of 0.2 nm by randomly counting 20 particles. The ArS-CdSe hybrid materials, as shown on the left side in Figure 40, also have a diameter of approximately 3.2 nm with a standard deviation of 0.3 nm. The similar particle size indicates that the CdSe nanoparticles will have consistent properties as a constituent of the hybrid materials. The exciton binding energy in CdSe nanoparticles is dependent on the particle

size. Since the quantum confinement dominates nanoparticle properties, the exciton binding energy has to be taken into account when it comes to determine the band gap of the CdSe nanoparticles. The exciton binding energy in CdSe nanoparticles with a particle size around 3 nm is 0.4 eV [132].

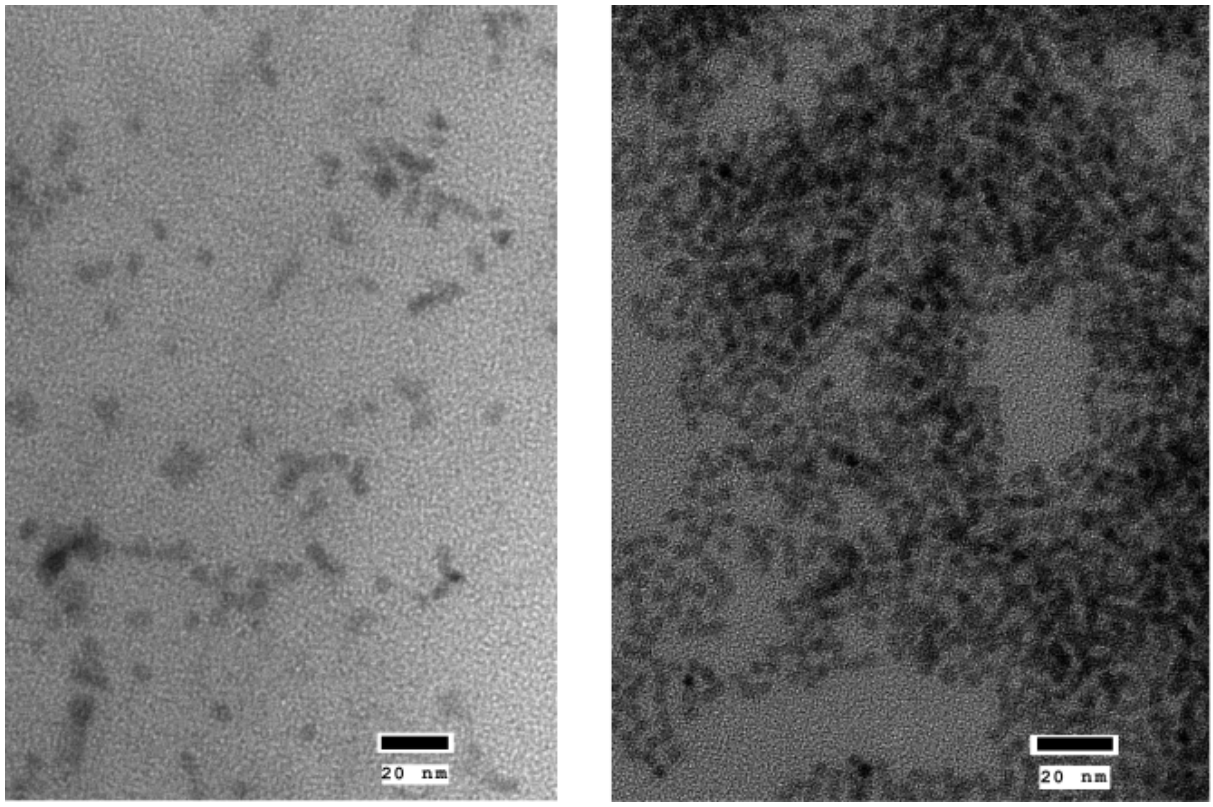

Figure 40: TEM images of the pyridine capped CdSe nanoparticles (right) and the ArS-CdSe hybrid materials.

4.4: Discussion

In the following section, the orbital alignment at the ArSH/CdSe physisorbed interface was determined and compared to the line-up at the internal interface within the hybrid materials.

4.4.1: Determination and Interpretation of the Orbital Alignment at the Physisorbed ArSH/CdSe Interface

The summarized orbital alignment at the ArSH/CdSe physisorbed interface is depicted in Figure 41. The optical band gap of the CdSe nanoparticles (2.1 eV) and the HOMO-LUMO gap of the ArSH ligands (4.2 eV) were estimated from UV-vis measurements. The exciton binding energy of 0.4 eV was taken into account to determine the true band gap of the CdSe nanoparticles which is 2.5 eV. As for CdSe nanoparticles, the density of states (DOS) tail in the conduction bands is close to the Fermi level according to the theoretical calculations by Pokrant and Whaley [133]. Our experimental results are in agreement with their calculations showing a highly degenerate surface of the CdSe nanoparticles. The Fermi level is located at the edge of the conduction bands. The hole injection barrier Φ_h was determined by the offset between the VBM of the CdSe nanoparticles and the HOMO cutoff of the ArSH ligands, yielding a value of 0.7 eV. The electron injection barrier Φe was determined to be 1.0 eV by subtracting the hole injection barrier (0.7 eV) and the band gap of CdSe nanoparticles (2.5 eV) from the HOMO-LUMO gap of the ArSH ligands (4.2 eV). The interface dipole eD was determined by taking the work function of the CdSe nanoparticles (Ψ_{CdSe} = 4.1 eV) and comparing it to the work function of the ArSH ligands, which yielded eD = 0.4 eV.

The mechanism behind the formation of this interface dipole relates to the charge donation from the ArSH ligands into the CdSe nanoparticles across the interface when the ArSH ligands make contact with the CdSe nanoparticles. Albero et al. reported that aromatic thiol derivatives have inner-molecule dipole moment. It points towards the sulfur atom resulting in an unbalanced electron density in the molecule due to the highly oxide tendency of the sulfur [134]. There is a similar dipole moment within the ArSH ligands due to the strong oxidation property of

the sulfur atom on the edge. The sulfur atom draws electrons from the rest of the molecule towards it. This mechanism can further enhance the charge transfer across the interface when the ligands made contact with the CdSe film through the sulfur atoms.

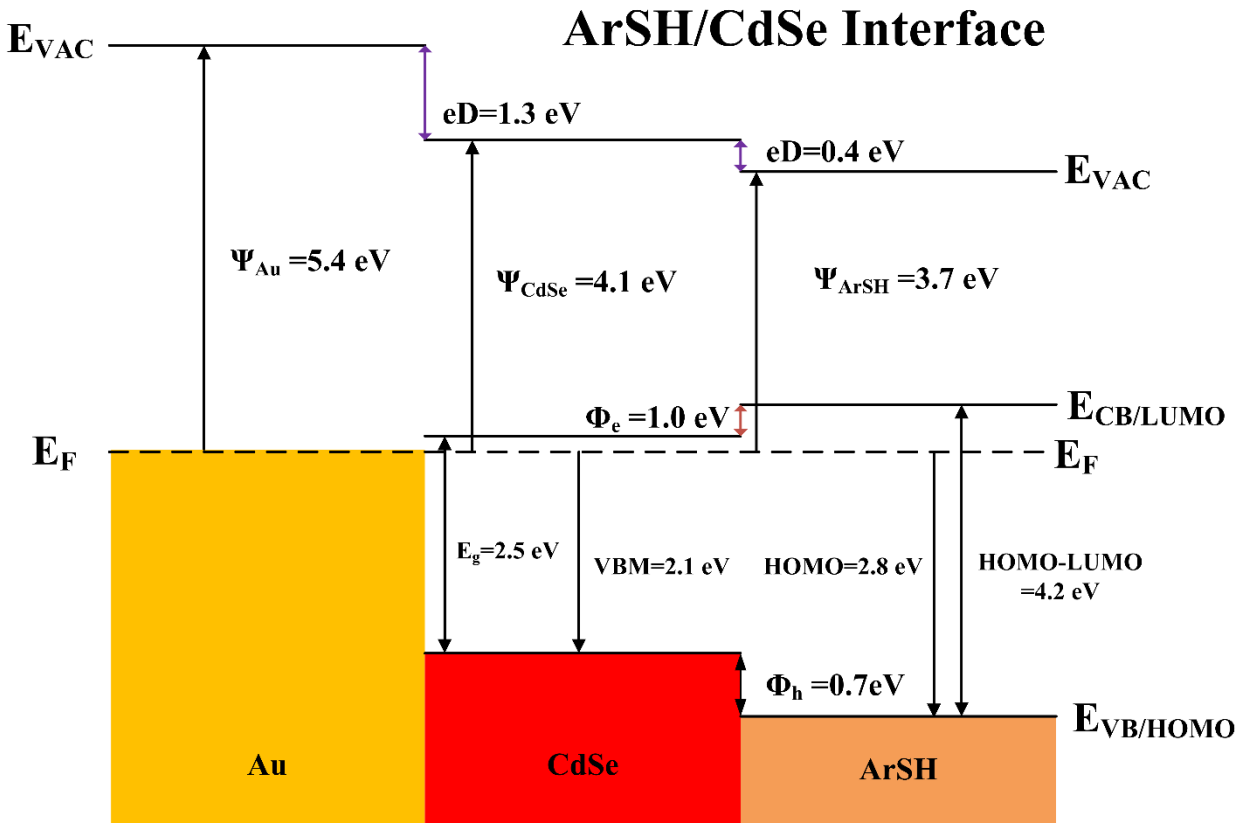

Figure 41: The schematic of the orbital alignment at ArSH/CdSe physisorbed interface.

4.4.2: Determination and Interpretation of the Orbital Alignment at the Internal Interface within the ArS-CdSe Hybrid Materials

Determination of the orbital alignment at the internal interface within the ArS-CdSe hybrid materials requires knowledge of the ionization energy of its two constituents. The

ionization energy is defined as the energy gap from the VBM/HOMO cutoff to the vacuum level. Figure 42 (A) shows the ionization energy determination for the CdSe nanoparticles. The values of the VBM and work function were obtained from the experiment described in section 4.3.1. By adding them together, the ionization energy of the CdSe nanoparticles was calculated to be 6.2 eV. Figure 42 (B) shows the magnified HOMO emission region (left) and the secondary edge of ArSH ligands (right) obtained from the experiment performed in section 4.3.2. The ionization energy of the ArSH ligands was determined to be 6.5 eV.

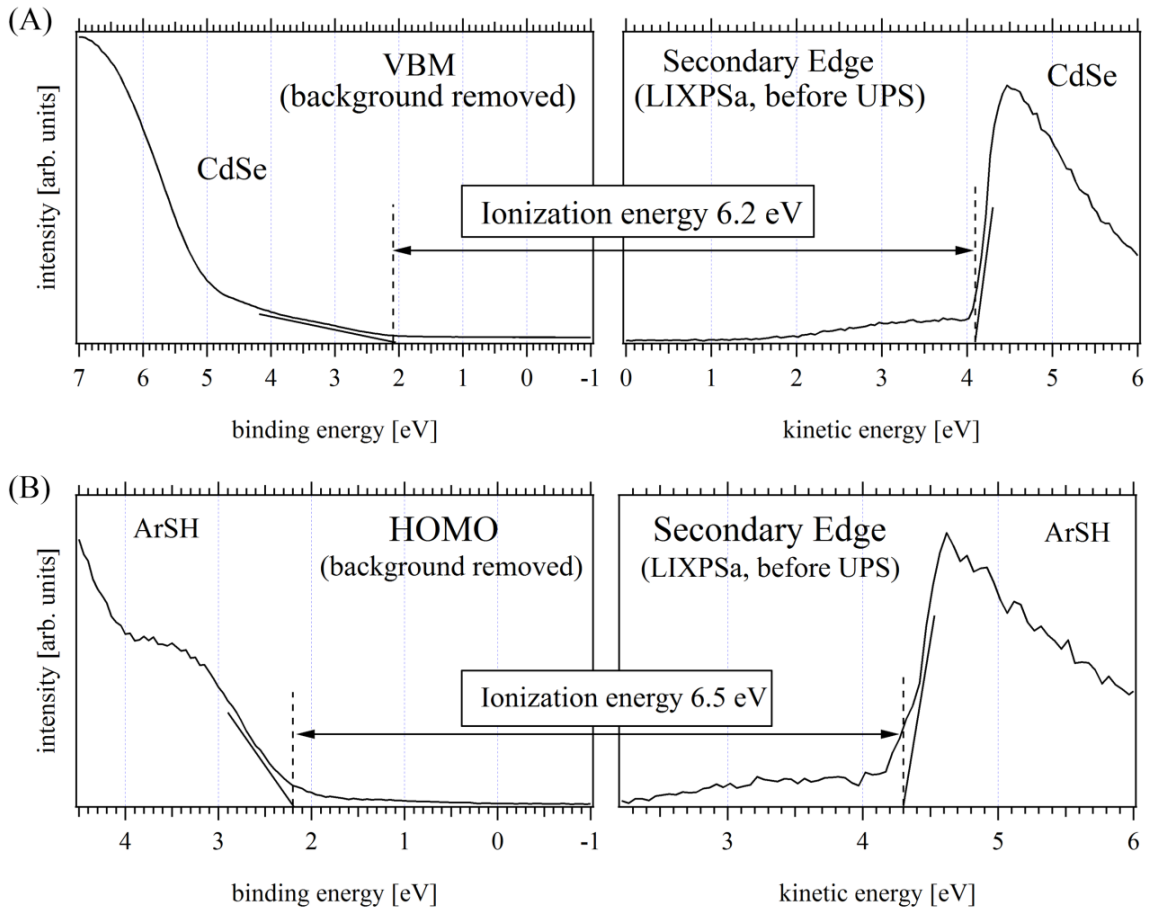

Figure 42: Ionization energy determination of the CdSe nanoparticles (A) and the ArSH ligands (B). The magnified VB/HOMO regions were obtained from the UPS measurement while the secondary edge was measured by LIXPSa.

In order to define the orbital alignment at the internal interface within the ArS-CdSe hybrid materials, the VBM and the work function of the CdSe constituent are required. For a given material the energy difference from the species core level to the VBM is a material constant. Based on this principle the VBM of the CdSe constituent can be determined by subtracting the Cd $3d_{5/2}$ to VBM energy difference from the binding energy of the Cd $3d_{5/2}$ core level line measured from the hybrid materials in section 4.3.3. The left graph of Figure 43 (A) shows the Cd $3d_{5/2}$ core level which was measured from the experiment described in section 4.3.1, yielding a binding energy of 405.8 eV. By subtracting the VBM of 2.1 eV, the energy difference from the Cd $3d_{5/2}$ to the VBM was determined to be 403.7 eV. The binding energy of the Cd $3d_{5/2}$ of the ArS-CdSe hybrid materials was measured to be 406.2 eV in section 4.3.3. By subtracting the energy difference 403.7 eV from the Cd $3d_{5/2}$ binding energy of 406.2 eV, the VBM of the CdSe constituent within the hybrid materials was calculated to be 2.5 eV.

In comparison to the pure CdSe nanoparticles, the binding energy of the Cd $3d_{5/2}$ measured from the ArS-CdSe hybrid materials shifts to a higher position by 0.4 eV (from 405.8 eV to 406.2 eV). As mentioned above, the pyridine capped CdSe nanoparticles were used to characterize the electronic structure of pure CdSe nanoparticles. The pyridine shells around the CdSe nanoparticles were peeled off leaving pure CdSe nanoparticles behind on the substrate when they were exposed to ultra-high vacuum after the deposition. Taylor et al. reported that nearly 70% of the CdSe nanoparticle surface is composed of Cd atoms and the other 30% is Se atoms [135]. Therefore, after in-vacuum deposition, the surface of the pure CdSe nanoparticles is rich of Cd atoms with dangling bonds which were previously bonded to pyridine molecules through nitrogen atoms. The Cd atoms with unoccupied dangling bonds are located at relative low binding energy level in XPS spectra. After hybridizing the CdSe nanoparticles with the

ArSH ligands, the Cd atoms on the surface were covalently bonded with the ArSH ligands through sulfur atoms. As a result, the dangling bonds on the surface of CdSe nanoparticles were saturated through the hybridizing process resulting in the shift of Cd $3d_{5/2}$ to a higher binding energy as observed in the XPS spectra.

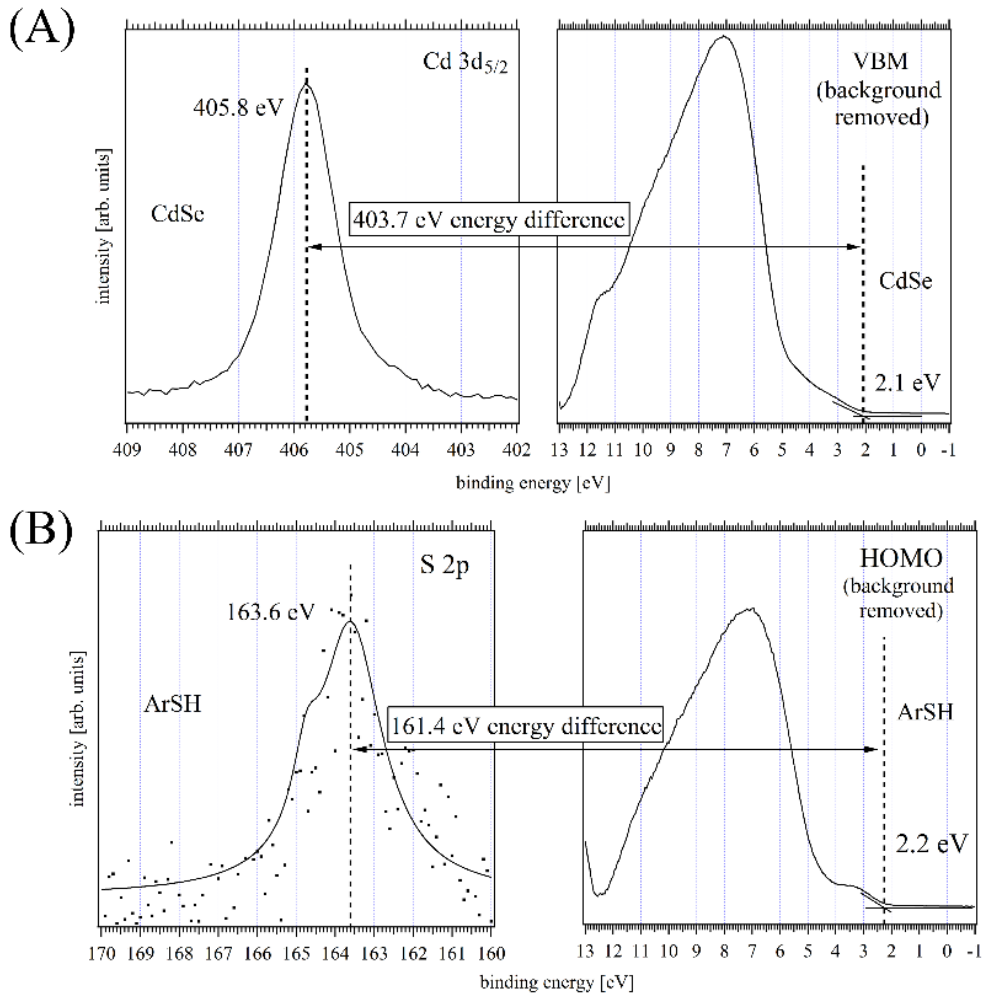

Figure 43: (A) Determination of the energy difference between the Cd 3d5/2 core level and the VBM of clean CdSe nanoparticles. The binding energy of Cd 3d5/2 is 405.8 eV and the VBM is 2.1 eV. The energy difference was determined to be 403.7 eV. (B) Determination of the energy difference between the S 2p core level and the HOMO cutoff of ArSH ligands. The binding energy of S 2p is 163.6 eV and the HOMO cutoff is 2.2 eV. The energy difference was determined to be 161.4 eV.

In order to determine the HOMO cutoff of the ArSH constituent in the hybrid materials, the energy difference from the S 2p line to the HOMO cutoff is needed. Figure 43 (B) shows how to determine it from the XP- and UP-spectrum measured from the ArSH ligands. The S 2p doublet was fitted to be at 163.6 eV and the HOMO cutoff was determined to be 2.2 eV. By subtracting 2.2 eV from 163.6 eV, it yielded an energy difference of 161.4 eV. The binding energy of the S 2p measured from the hybrid materials was 164.4 eV. By subtracting the energy difference of 161.4 eV from the binding energy of the S 2p line in the hybrid, the HOMO cutoff of the ArSH constituent was determined to be 3.0 eV.

By summarizing the results above, Figure 44 was depicted, showing the orbital alignment at the internal interface in the ArS-CdSe hybrid materials. The orbital alignment shows a smaller hole injection barrier of 0.5 eV compared to the barrier at the physisorbed interface which is 0.7 eV. A 0.2 eV interface dipole is observed as a result of the electronic system shift for both of the constituents. The mechanism behind the electronic system shift of the CdSe constituent was discussed above. In order to understand the basic mechanism behind the electronic system shift on the ArSH side, the hard-soft-acid-base (HSAB) concept needs to be discussed [114]. The hard-soft-acid-base (HSAB) is a universal law to describe reactions between organic materials and inorganic materials. In this concept, the interaction between the metal atoms and the surrounding ligands involves an electron transfer process in which the metal acts as an electron acceptor (Lewis acid) and the ligand acts as an electron donor (Lewis base). The surrounding ligands donate electrons to the unoccupied orbitals of the metal atoms. Therefore, the soft ArSH ligands bond to the surface of the soft CdSe nanoparticles filling the Cd orbitals covalently, which results in the shift of the S 2p core level to a higher binding energy. This theory is also

confirmed by Liu et al. and supported by the electronic system shift of the ArSH constituent observed in the presenting experiments [126].

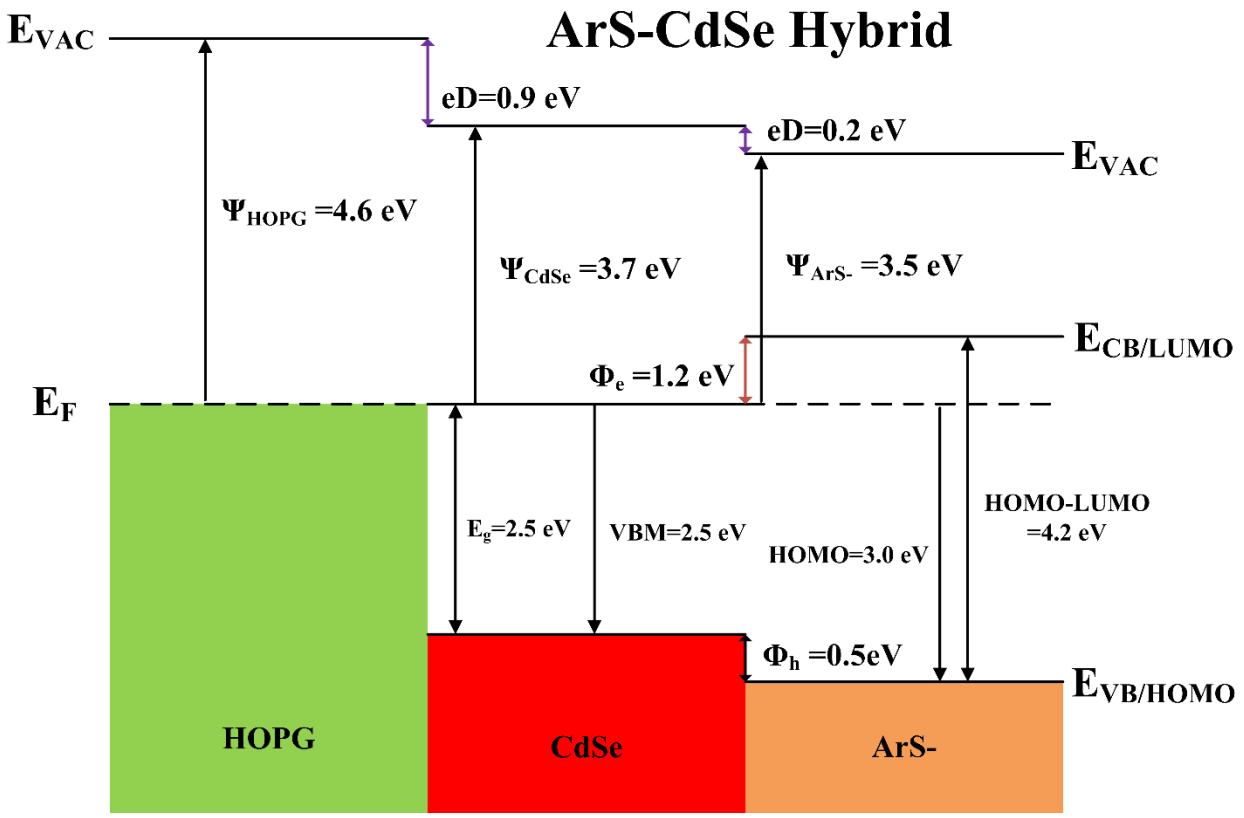

Figure 44: The schematic depiction of the orbital alignment at the internal interface within the ArS-CdSe hybrid materials. An internal interface eD was observed with a value of 0.2 eV. The electron injection barrier is 1.2 eV while the hole injection barrier is 0.5 eV.

It is worthy to notice that the covalent bonds play an important role in modifying the orbital alignment at the internal interface. The sulfur atom attracts electrons from the Cadmium atom when they make contact forming a covalent bond due to the oxidization property of sulfur atoms as shown in Figure 45. As a result of the electron density redistribution at the interface, an inner-molecule field can be built up. With the new built up field, the electron transfer at the

interface can be enhanced. Furthermore, when light generated excitons diffuse to the internal interface, with shorter diffusion length compared to the physical blending, the net result can facilitate the dissociation of the excitons. This mechanism is crucial for the improvement of hybrid photovoltaic devices. After the dissociation, electrons can transport into the CdSe nanoparticles easily due to the large electron injection barrier at the interface which can also prevent charge-recombination.

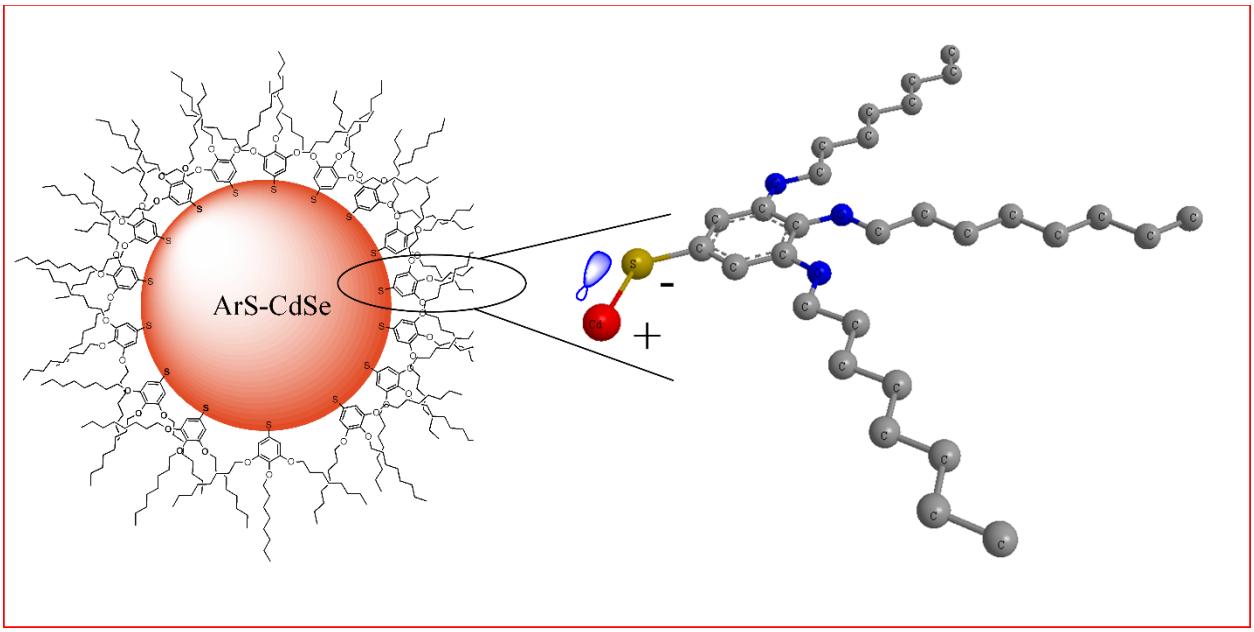

Figure 45: The schematic of the ArS-CdSe hybrid materials. The covalent bond between sulfur atom and Cadmium atom has significant influences on the orbital alignment at the interface.

CHAPTER 5: CONCLUSIONS AND OUTLOOK

The work presented in this dissertation successfully employed PES measurements to characterize the orbital alignment at the internal interface within hybrid materials. The investigation showed that hybridizing organic ligands to inorganic nanoparticles through covalent bonding has significant impacts on the electronic structure of the interface.

The study aimed at developing a PES based characterization protocol that allows for the determination of the orbital alignment at the hybrid internal interface. The research interest on hybrid materials is motivated by the low efficiency of hetero-junction solar cells which is believed to be caused by inefficient charge-dissociation at the interface between inorganic nanoparticles and conjugated polymers. A promising approach to solve this problem is the synthesis of a hybrid material in which the organic material is hybridized with the inorganic nanoparticles by covalent bonding. The key to developing an ideal hybrid material with an improved efficiency is to find constituents with matching electronic structures to facilitate charge dissociation and transportation at the interface after the hybridization. A PES base characterization protocol is needed to determine the orbital alignment at the hybrid internal interface.

In the first part, a prototypical hybrid material synthesized by hybridizing TiO_2 nanoparticles with oligothiophene ligands was investigated. Since photon excited emissions from both constituents are superimposed to yield hybrid-unique emission features in UP-spectra, it is impossible to determine the orbital alignment at the internal interface directly. The proposed

characterization protocol circumvents this challenge by characterizing the isolated constituents first and comparing the obtained binding energies of the core level emissions to those measured from the hybrid. The comparison allows for the direct quantification of the charge injection barriers and the dipole potential at the internal interface. It was found that the electronic system of the oligothiophene shifted to lower energy level relative the TiO_2 system after the hybridization. An internal interface dipole potential of 0.61 eV was observed as a result of the covalent bonding. The resulting orbital alignment features a significant hole injection barrier of 0.73 eV and only an insignificant electron injection barrier of 0 eV. This internal interface appears unideal for the purpose of improving exciton dissociation. Even though electrons can transfer easily across the interface, a significant rectifying electron injection barrier is needed to prevent the electrons from returning and recombining with the holes on the ligands side. This points out that this interface needs to be redesigned with an interface dipole capable of shifting the electronic system of ligands to a higher energy level thereby producing favorable band offsets.

The second part involved determining and discussing the orbital alignment at the internal interface within the ArS-CdSe hybrid materials. In addition to that, a physisorbed ArSH/CdSe interface was created by multi-step deposition technique and characterized to compare with the internal interface. As for the physisorbed interface, charge transfer across the interface was observed as indicated by the appearance of a dipole potential. The polarity of this dipole demonstrates that the ArSH ligands donate electrons to the CdSe nanoparticles when they make contact with each other. A large electron injection barrier of 1.0 eV was found at the interface which can block electrons from returning to the ArSH ligands and recombining with holes. It was observed that a hole injection barrier of 0.7 eV existed at the interface. However, the

polarity of this barrier does not favor the hole transfer from the CdSe nanoparticles to the ArSH ligands.

The orbital alignment at the internal interface within the ArS-CdSe hybrid materials demonstrates that hybridizing the ArSH ligands with the CdSe nanoparticles by covalent bonding realigns the interface line-up. It was found that the electronic system of the CdSe nanoparticle shifted down by 0.4 eV. This is attributed to the saturation of the unoccupied bonds of the Cd atoms on the surface due to the formation of Cd-S bonds. Meanwhile, the electronic system of the ArSH ligands shifted down by 0.2 eV as a result of the electron donation into the nanoparticles. Compared to the physisorbed interface, a smaller interface dipole of 0.2 eV was found. The injection barrier at this interface was found to be 1.2 eV which was 0.2 eV larger than that at the physisorbed interface while a smaller hole injection (0.5 eV) was found at the internal interface.

The conducted experiments have proved the feasibility and practicability of the proposed PES based characterization protocol. Once sophisticated hybrid materials are available, the protocol can provide detailed information regarding to the orbital alignment which can be ultimately used to improve the synthetic strategy and guide the selection of constituent materials increasing overall efficiency.

REFERENCES

1. Jacobson, M.Z. and M.A. Delucchi, *A path to sustainable energy by 2030.* Scientific American, 2009. **301**(5): p. 58-65.

2. Feynman, R.P., *The pleasure of finding things out: The best short works of Richard P. Feynman*. 2005: Basic Books.

3. Serrano, E., G. Rus, and J. Garcia-Martinez, *Nanotechnology for sustainable energy.* Renewable and Sustainable Energy Reviews, 2009. **13**(9): p. 2373-2384.

4. Edelstein, A.S. and R. Cammaratra, *Nanomaterials: synthesis, properties and applications*. 1998: CRC Press.

5. Zhang, Q., et al., *Nanomaterials for energy conversion and storage.* Chemical Society Reviews, 2013.

6. Zhong, M., et al., *Improving the performance of CdS/P3HT hybrid inverted solar cells by interfacial modification.* Solar Energy Materials and Solar Cells, 2012. **96**(0): p. 160-165.

7. Sai, N., K. Leung, and J.R. Chelikowsky, *Hybrid density functional study of oligothiophene/ZnO interface for photovoltaics.* Physical Review B, 2011. **83**(12): p. 121309.

8. Guo, T.-F., et al., *Effects of film treatment on the performance of poly (3-hexylthiophene)/soluble fullerene-based organic solar cells.* Thin Solid Films, 2008. **516**(10): p. 3138-3142.

9. Yella, A., et al., *Porphyrin-sensitized solar cells with cobalt (II/III)–based redox electrolyte exceed 12 percent efficiency.* Science, 2011. **334**(6056): p. 629-634.

10. Sun, B., E. Marx, and N.C. Greenham, *Photovoltaic devices using blends of branched CdSe nanoparticles and conjugated polymers.* Nano Letters, 2003. **3**(7): p. 961-963.

11. Puzder, A., et al., *The effect of organic ligand binding on the growth of CdSe nanoparticles probed by ab initio calculations.* Nano Letters, 2004. **4**(12): p. 2361-2365.

12. Zhou, Y., et al., *Efficiency enhancement for bulk-heterojunction hybrid solar cells based on acid treated CdSe quantum dots and low bandgap polymer PCPDTBT.* Solar Energy Materials and Solar Cells, 2011. **95**(4): p. 1232-1237.

13. Simon, J. and J.-J. Andre, *Molecular semiconductors: photoelectrical properties and solar cells.* NASA STI/Recon Technical Report A, 1985. **86**: p. 21312.

14. Gregg, B.A., *Excitonic Solar Cells.* The Journal of Physical Chemistry B, 2003. **107**(20): p. 4688-4698.

15. Scharber, M.C., et al., *Design Rules for Donors in Bulk-Heterojunction Solar Cells—Towards 10 % Energy-Conversion Efficiency.* Advanced Materials, 2006. **18**(6): p. 789-794.

16. Zhou, Y., M. Eck, and M. Kruger, *Bulk-heterojunction hybrid solar cells based on colloidal nanocrystals and conjugated polymers.* Energy & Environmental Science, 2010. **3**(12): p. 1851-1864.

17. Wang, F., et al., *Spectroscopic Identification of Tri-n-octylphosphine Oxide (TOPO) Impurities and Elucidation of Their Roles in Cadmium Selenide Quantum-Wire Growth.* Journal Of The American Chemical Society, 2009. **131**(13): p. 4983-4994.

18. Bouclé, J., et al., *Hybrid Solar Cells from a Blend of Poly(3-hexylthiophene) and Ligand-Capped TiO2 Nanorods.* Advanced Functional Materials, 2008. **18**(4): p. 622-633.

19. Beerbom, M.M., R. Gargagliano, and R. Schlaf, *Determination of the electronic structure of self-assembled L-cysteine/Au interfaces using photoemission spectroscopy.* Langmuir, 2005. **21**(8): p. 3551-3558.

20. Gutmann, S., et al., *Electronic structure of indium tin oxide/nanocrystalline TiO2 interfaces as used in dye-sensitized solar cell devices.* Journal Of Applied Physics, 2011. **109**(11): p. 113719.

21. Dam, N., et al., *Charge Injection Barriers at a Ribonucleic Acid/Inorganic Material Contact Determined by Photoemission Spectroscopy.* The Journal of Physical Chemistry B, 2004. **109**(2): p. 748-756.

22. Lyon, J.E., et al., *Photoemission study of the poly(3-hexylthiophene)/Au interface.* Applied Physics Letters, 2006. **88**(22).

23. Leutwyler, W.K., S.L. Bürgi, and H. Burgl, *Semiconductor clusters, nanocrystals, and quantum dots.* Science, 1996. **271**: p. 933.

24. Rogach, A.L., D.V. Talapin, and H. Weller, *Semiconductor Nanoparticles*, in *Colloids and Colloid Assemblies*. 2004, Wiley-VCH Verlag GmbH & Co. KGaA. p. 52-95.

25. Monson, T.C., et al., *A simple low-cost synthesis of brookite TiO2 nanoparticles.* Journal of Materials Research, 2013. **28**(03): p. 348-353.

26. Lu, X.H., *Efficient Electroless nickel planting from highly active Ni-B nanoparticles for electric circuit pattern.* J. Mater. Chem. C, 2013.

27. Yuan, F., et al., *Synthesis of poly (butyl acrylate)—laponite nanocomposite nanoparticles for improving the impact strength of poly (lactic acid).* Journal of Applied Polymer Science, 2013.

28. Zhang, J., et al., *A Heat-Resistant Silica Nanoparticle Enhanced Polysulfonamide Nonwoven Separator for High-Performance Lithium Ion Battery.* Journal of The Electrochemical Society, 2013. **160**(6): p. A769-A774.

29. Grätzel, M., *Dye-sensitized solar cells.* Journal of Photochemistry and Photobiology C: Photochemistry Reviews, 2003. **4**(2): p. 145-153.

30. Loef, R., et al., *Study of Electronic Defects in CdSe Quantum Dots and Their Involvement in Quantum Dot Solar Cells.* Nano Letters, 2009. **9**(2): p. 856-859.

31. Chandiran, A.K., et al., *Evaluating the Critical Thickness of TiO2 Layer on Insulating Mesoporous Templates for Efficient Current Collection in Dye-Sensitized Solar Cells.* Advanced Functional Materials, 2013.

32. Fukumoto, T., et al., *Effect of Interfacial Engineering in Solid-State Nanostructured Sb2S3 Heterojunction Solar Cells (Adv. Energy Mater. 1/2013).* Advanced Energy Materials, 2013. **3**(1): p. 28-28.

33. Chang, A.Y., et al., *Charge Carrier Dynamics of Vapor-Deposited Small-Molecule/Fullerene Organic Solar Cells.* Journal of the American Chemical Society, 2013.

34. Kyaw, A.K.K., et al., *Improved Light Harvesting and Improved Efficiency by Insertion of an Optical Spacer (ZnO) in Solution-Processed Small-Molecule Solar Cells.* Nano letters, 2013. **13**(8): p. 3796-3801.

35. He, M., et al., *All-conjugated poly (3-alkylthiophene) diblock copolymer-based bulk heterojunction solar cells with controlled molecular organization and nanoscale morphology.* Energy & Environmental Science, 2011. **4**(8): p. 2894-2902.

36. He, M., et al., *Thermopower enhancement in conducting polymer nanocomposites via carrier energy scattering at the organic–inorganic semiconductor interface.* Energy & Environmental Science, 2012. **5**(8): p. 8351-8358.

37. He, M., et al., *Graphene-based transparent flexible electrodes for polymer solar cells.* Journal Of Materials Chemistry, 2012. **22**(46): p. 24254-24264.

38. Saunders, B.R. and M.L. Turner, *Nanoparticle–polymer photovoltaic cells.* Advances In Colloid and Interface Science, 2008. **138**(1): p. 1-23.

39. Huynh, W.U., et al., *Controlling the Morphology of Nanocrystal–Polymer Composites for Solar Cells.* Advanced Functional Materials, 2003. **13**(1): p. 73-79.

40. Selvan, J.A.A., et al. *Evaluation of Ar-diluted silane PECVD for thin film Si: H based solar cells*. 2004. San Francisco, CA, United States: Materials Research Society, Warrendale, PA 15086, United States.

41. Waldrop, J.R. and R.W. Grant, *Semiconductor Heterojunction Interfaces: Nontransitivity of Energy-band Discontiuities.* Physical Review Letters, 1979. **43**(22): p. 1686.

42. Moulé, A.J., et al., *Hybrid solar cells: basic principles and the role of ligands.* Journal Of Materials Chemistry, 2012. **22**(6): p. 2351-2368.

43. Nizamoglu, S., X.W. Sun, and H.V. Demir, *Observation of efficient transfer from Mott–Wannier to Frenkel excitons in a hybrid semiconductor quantum dot/polymer composite at room temperature.* Applied Physics Letters, 2010. **97**(26): p. 263106-263106-3.

44. Birman, J.L. and N.Q. Huong, *Wannier–Frenkel hybrid exciton in organic–semiconductor quantum dot heterostructures.* Journal Of Luminescence, 2007. **125**(1): p. 196-200.

45. Dayal, S., et al., *Photovoltaic Devices with a Low Band Gap Polymer and CdSe Nanostructures Exceeding 3% Efficiency.* Nano Letters, 2009. **10**(1): p. 239-242.

46. Neouze, M.-A. and U. Schubert, *Surface Modification and Functionalization of Metal and Metal Oxide Nanoparticles by Organic Ligands.* Monatshefte für Chemie / Chemical Monthly, 2008. **139**(3): p. 183-195.

47. Schroeder, P.G., et al., *Investigation of band bending and charging phenomena in frontier orbital alignment measurements of para-quaterphenyl thin films grown on highly oriented pyrolytic graphite and SnS2.* Surface Science, 2000. **459**(3): p. 349-364.

48. Sze, S.M. and K.K. Ng, *Physics of semiconductor devices*. 2006: Wiley. com.

49. Anderson, R., *Experiments on Ge-GaAs heterojunctions.* Solid-state Electronics, 1962. **5**(5): p. 341-351.

50. Dam, N., et al., *Photoelectron spectroscopic investigation of in-vacuum-prepared luminescent polymer thin films directly from solution.* Journal Of Applied Physics, 2005. **97**(2).

51. Cascio, A.J., et al., *Investigation of a polythiophene interface using photoemission spectroscopy in combination with electrospray thin-film deposition.* Applied Physics Letters, 2006. **88**(6).

52. Bard, A.J., et al., *The concept of Fermi level pinning at semiconductor/liquid junctions. Consequences for energy conversion efficiency and selection of useful solution redox couples in solar devices.* Journal Of The American Chemical Society, 1980. **102**(11): p. 3671-3677.

53. Salaneck, W.R., et al., *The electronic structure of polymer–metal interfaces studied by ultraviolet photoelectron spectroscopy.* Materials Science and Engineering: R: Reports, 2001. **34**(3): p. 121-146.

54. Ito, S., et al., *Fabrication of thin film dye sensitized solar cells with solar to electric power conversion efficiency over 10%.* Thin Solid Films, 2008. **516**(14): p. 4613-4619.

55. Makinen, A., et al., *Photoemission study of frontier orbital alignment at a metal–organic interface as a function of conjugation length of oligothiophene derivatives.* Applied Physics Letters, 2001. **78**(5): p. 670-672.

56. Lagel, B., et al., *Investigation of the poly [2-methoxy-5-(2'-ethyl-hexyloxy)-1, 4-phenylene vinylene]/indium tin oxide interface using photoemission spectroscopy.* Journal of applied physics, 2005. **98**(2): p. 023512-023512-7.

57. Magulick, J., et al., *Ionization energy and electronic structure of polycytidine.* The Journal of Physical Chemistry B, 2006. **110**(6): p. 2692-2699.

58. Cascio, A., et al., *Investigation of a polythiophene interface using photoemission spectroscopy in combination with electrospray thin-film deposition.* Applied physics letters, 2006. **88**(6): p. 062104-062104-3.

59. Lyon, J., et al., *Photoemission study of the poly (3-hexylthiophene)/Au interface.* Applied physics letters, 2006. **88**(22): p. 222109-222109-3.

60. Tani, Y., S. Kobayashi, and H. Kawazoe, *Ion Beam Deposition of Quantum Dots from Colloidal Solution.* Japanese Journal of Applied Physics, 2008. **47**: p. 2977.

61. Morozov, V.N. and T.Y. Morozova, *Electrospray deposition as a method to fabricate functionally active protein films.* Analytical chemistry, 1999. **71**(7): p. 1415-1420.

62. Cole, R.B., *Electrospray Mass Spectrometry—Fundamentals, Instrumentation and Application*. 1997: John Wiley: New York.

63. Dam, N., et al., *Photoelectron spectroscopic investigation of in-vacuum-prepared luminescent polymer thin films directly from solution.* Journal of applied physics, 2005. **97**(2): p. 024909-024909-7.

64. Taylor, G., *Disintegration of water drops in an electric field.* Proceedings of the Royal Society of London. Series A. Mathematical and Physical Sciences, 1964. **280**(1382): p. 383-397.

65. Hertz, H., *Untersuchungen über die Ausbreitung der elektrischen Kraft*. Vol. 2. 1894: JA Barth.

66. Einstein, A., *Generation and conversion of light with regard to a heuristic point of view.* Ann Phys, 1905. **17**: p. 132-148.

67. Nordling, C., E. Sokolowski, and K. Siegbahn, *Precision method for obtaining absolute values of atomic binding energies.* Physical Review, 1957. **105**(5): p. 1676.

68. Scofield, J., *Hartree-Slater subshell photoionization cross-sections at 1254 and 1487 eV.* Journal of Electron Spectroscopy and Related Phenomena, 1976. **8**(2): p. 129-137.

69. Hűfner, S., *Photoelectron Spectroscopy: principles and applications*. 2003: Springer.

70. Zangwill, A., *Physics at surfaces*. 1988: Cambridge University Press.

71. Erdem, B., et al., *XPS and FTIR surface characterization of TiO2 particles used in polymer encapsulation.* Langmuir, 2001. **17**(9): p. 2664-2669.

72. Briggs, D. and J.T. Grant, *Surface analysis by Auger and X-ray photoelectron spectroscopy*. 2003: IM Publications Chichester, UK.

73. Gutmann, S., et al., *Effect of ultraviolet and x-ray radiation on the work function of TiO2 surfaces.* Journal Of Applied Physics, 2010. **107**(10).

74. Gutmann, S., et al., *Effect of ultraviolet and x-ray radiation on the work function of TiO[sub 2] surfaces.* Journal Of Applied Physics, 2010. **107**(10): p. 103705.

75. Beerbom, M., et al., *Direct comparison of photoemission spectroscopy and in situ Kelvin probe work function measurements on indium tin oxide films.* Journal of electron spectroscopy and related phenomena, 2006. **152**(1): p. 12-17.

76. Yanagida, S., et al., *Polythiophene-sensitized TiO2 solar cells.* Journal of Photochemistry and Photobiology A: Chemistry, 2004. **166**(1-3): p. 75-80.

77. Kim, Y.-G., et al., *Efficient Light Harvesting Polymers for Nanocrystalline TiO2 Photovoltaic Cells†.* Nano Letters, 2003. **3**(4): p. 523-525.

78. Yu, G., et al., *Polymer Photovoltaic Cells: Enhanced Efficiencies via a Network of Internal Donor-Acceptor Heterojunctions.* Science, 1995. **270**(5243): p. 1789-1791.

79. Magdalena, S., *Hybrid conjugated polymer/semiconductor photovoltaic cells.* Synthetic Metals, 2010. **160**(1–2): p. 1-15.

80. Qian, L., et al., *Hybrid polymer-CdSe solar cells with a ZnO nanoparticle buffer layer for improved efficiency and lifetime.* Journal Of Materials Chemistry, 2011. **21**(11): p. 3814-3817.

81. Law, M., et al., *Nanowire dye-sensitized solar cells.* Nat Mater, 2005. **4**(6): p. 455-459.

82. Aygül, U., et al., *Electronic Properties of Interfaces between PCPDTBT and Prototypical Electrodes Studied by Photoemission Spectroscopy.* Chemphyschem, 2011. **12**(12): p. 2345-2351.

83. Liu, J., et al., *Employing End-Functional Polythiophene To Control the Morphology of Nanocrystal−Polymer Composites in Hybrid Solar Cells.* Journal Of The American Chemical Society, 2004. **126**(21): p. 6550-6551.

84. Sariciftci, N.S., et al., *Photoinduced Electron Transfer from a Conducting Polymer to Buckminsterfullerene.* Science, 1992. **258**(5087): p. 1474-1476.

85. Bouclé, J. and J. Ackermann, *Solid-state dye-sensitized and bulk heterojunction solar cells using TiO2 and ZnO nanostructures: recent progress and new concepts at the borderline.* Polymer International, 2011: p. n/a-n/a.

86. Ong, B.S., et al., *Thiophene Polymer Semiconductors for Organic Thin-Film Transistors.* Chemistry – A European Journal, 2008. **14**(16): p. 4766-4778.

87. Kim, Y., et al., *A strong regioregularity effect in self-organizing conjugated polymer films and high-efficiency polythiophene:fullerene solar cells.* Nat Mater, 2006. **5**(3): p. 197-203.

88. Xiong, H.M., et al., *Bonding Polyether onto ZnO Nanoparticles: An Effective Method for Preparing Polymer Nanocomposites with Tunable Luminescence and Stable Conductivity.* Advanced Functional Materials, 2005. **15**(11): p. 1751-1756.

89. Duhm, S., et al., *Orientation-dependent ionization energies and interface dipoles in ordered molecular assemblies.* Nat Mater, 2008. **7**(4): p. 326-332.

90. Garcia, R., et al., *Size and Shape Controlled Growth of Molecular Nanostructures on Silicon Oxide Templates.* Nano Letters, 2004. **4**(6): p. 1115-1119.

91. Blumstengel, S., et al., *Interface formation and electronic structure of alpha-sexithiophene on ZnO.* Applied Physics Letters, 2008. **92**(19): p. 193303.

92. Wang, S., et al., *"Anchor effect" in poly(styrene maleic anhydride)/TiO2 nanocomposites.* Journal Of Materials Science Letters, 1999. **18**(24): p. 2009-2012.

93. Serban, B., et al. *New ligand selection rule for quantum dot functionalization.* in *Semiconductor Conference, 2009. CAS 2009. International*. 2009.

94. Ding, H., M. Kumar Ram, and C. Nicolini, *Construction of organic-inorganic hybrid ultrathin films self-assembled from poly(thiophene-3-acetic acid) and TiO2.* Journal Of Materials Chemistry, 2002. **12**(12).

95. Grant, R.W., J.R. Waldrop, and E.A. Kraut, *Observation of the Orientation Dependence of Interface Dipole Energies in Ge-GaAs.* Physical Review Letters, 1978. **40**(10): p. 656-659.

96. Lyon, J.E., et al., *Electronic structure of the indium tin oxide/nanocrystalline anatase (TiO2)/ruthenium-dye interfaces in dye-sensitized solar cells.* Journal Of Applied Physics, 2008. **104**(7).

97. Cascio, A.J., et al., *Investigation of a polythiophene interface using photoemission spectroscopy in combination with electrospray thin-film deposition*. Vol. 88. 2006: AIP. 062104.

98. Kahn, A., N. Koch, and W. Gao, *Electronic structure and electrical properties of interfaces between metals and π-conjugated molecular films.* Journal of Polymer Science Part B: Polymer Physics, 2003. **41**(21): p. 2529-2548.

99. Magulick, J., M.M. Beerbom, and R. Schlaf, *Comparison of Ribonucleic Acid Homopolymer Ionization Energies and Charge Injection Barriers.* The Journal of Physical Chemistry B, 2006. **110**(32): p. 15973-15981.

100. Park, K., et al., *Charge Transport Properties in TiO2 Network with Different Particle Sizes for Dye Sensitized Solar Cells.* ACS Applied Materials & Interfaces, 2013.

101. Sanjines, R., et al., *Electronic structure of anatase TiO[sub 2] oxide.* Journal Of Applied Physics, 1994. **75**(6): p. 2945-2951.

102. Liu, G., et al., *XPS and UPS Characterization of the TiO2/ZnPcGly Heterointerface: Alignment of Energy Levels.* The Journal of Physical Chemistry B, 2002. **106**(23): p. 5814-5819.

103. Li, Z., et al., *Measurement of the Internal Orbital Alignment of Oligothiophene-TiO2 Nanoparticle Hybrids.* The Journal of Physical Chemistry C, 2013.

104. Cahen, D., et al., *Nature of Photovoltaic Action in Dye-Sensitized Solar Cells.* The Journal of Physical Chemistry B, 2000. **104**(9): p. 2053-2059.

105. Schön, J., C. Kloc, and B. Batlogg, *Charge transport in oligothiophene single crystals.* Synthetic metals, 2000. **115**(1): p. 75-78.

106. Thompson, T.L. and J.T. Yates Jr, *TiO2-based photocatalysis: Surface defects, oxygen and charge transfer.* Topics in Catalysis, 2005. **35**(3-4): p. 197-210.

107. Cho, E., et al., *First-principles study of point defects in rutile TiO_{2−x}.* Physical Review B, 2006. **73**(19): p. 193202.

108. Na-Phattalung, S., et al., *First-principles study of native defects in anatase TiO_{2}.* Physical Review B, 2006. **73**(12): p. 125205.

109. Göpel, W. and U. Lampe, *Influence of defects on the electronic structure of zinc oxide surfaces.* Physical Review B, 1980. **22**(12): p. 6447-6462.

110. Carreras, P., et al., *The electronic structure of co-sputtered zinc indium tin oxide thin films.* Journal Of Applied Physics, 2011. **110**(7): p. 073711.

111. Klein, A., et al., *Surface potentials of magnetron sputtered transparent conducting oxides.* Thin Solid Films, 2009. **518**(4): p. 1197-1203.

112. Liang, Z., et al., *Covalent Layer-by-Layer Assembly of Conjugated Polymers and CdSe Nanoparticles: Multilayer Structure and Photovoltaic Properties.* Advanced Functional Materials, 2006. **16**(4): p. 542-548.

113. Xiong, S., et al., *Covalently Bonded Polyaniline−TiO2 Hybrids: A Facile Approach to Highly Stable Anodic Electrochromic Materials with Low Oxidation Potentials.* Chemistry Of Materials, 2009. **22**(1): p. 255-260.

114. Pearson, R.G., *Hard and Soft Acids and Bases.* Journal Of The American Chemical Society, 1963. **85**(22): p. 3533-3539.

115. Temprado, M., et al., *Experimental and Computational Thermochemistry of 2- and 3-Thiophenecarboxylic Acids.* The Journal of Physical Chemistry A, 2002. **106**(46): p. 11173-11180.

116. Lokteva, I., et al., *Surface Treatment of CdSe Nanoparticles for Application in Hybrid Solar Cells: The Effect of Multiple Ligand Exchange with Pyridine.* Journal of Physical Chemistry C, 2010. **114**(29): p. 12784-12791.

117. Coe, S., et al., *Electroluminescence from single monolayers of nanocrystals in molecular organic devices.* Nature, 2002. **420**(6917): p. 800-803.

118. Greenham, N.C., X. Peng, and A.P. Alivisatos, *Charge separation and transport in conjugated-polymer/semiconductor-nanocrystal composites studied by photoluminescence quenching and photoconductivity.* Physical Review B, 1996. **54**(24): p. 17628-17637.

119. Persano, A., et al., *Charge carrier transport in thin films of colloidal CdSe quantum rods.* Journal Of Applied Physics, 2008. **104**(7).

120. Yi, Y., et al., *Orbital alignment at poly 2-methoxy-5-(2(')-ethylhexyloxy)-p-phenylene vinylene interfaces.* Journal Of Applied Physics, 2007. **102**(2).

121. Helgesen, M., R. Sondergaard, and F.C. Krebs, *Advanced materials and processes for polymer solar cell devices.* Journal Of Materials Chemistry, 2010. **20**(1): p. 36-60.

122. Liang, Y.Y., et al., *For the Bright Future-Bulk Heterojunction Polymer Solar Cells with Power Conversion Efficiency of 7.4%.* Advanced Materials, 2010. **22**(20): p. E135-+.

123. Ginger, D.S. and N.C. Greenham, *Charge injection and transport in films of CdSe nanocrystals.* Journal Of Applied Physics, 2000. **87**(3): p. 1361-1368.

124. Araci, Z.O., et al., *Potential-Modulated Attenuated Total Reflectance Characterization of Charge Injection Processes in Monolayer-Tethered CdSe Nanocrystals.* Journal of Physical Chemistry Letters, 2010. **1**(12): p. 1900-1905.

125. Gommans, H., et al., *Exciton Diffusion Length and Lifetime in Subphthalocyanine Films.* The Journal of Physical Chemistry C, 2009. **113**(7): p. 2974-2979.

126. Liu, I.S., et al., *Enhancing photoluminescence quenching and photoelectric properties of CdSe quantum dots with hole accepting ligands.* Journal Of Materials Chemistry, 2008. **18**(6): p. 675-682.

127. Ogurtsov, N.A., et al., *Synthesis and Properties of Hybrid Poly(3-Methylthiophene)-CdSe Nanocomposite and Estimation of Its Photovoltaic Ability.* Molecular Crystals and Liquid Crystals, 2011. **536**(1): p. 33/[265]-40/[272].

128. Katari, J.E.B., V.L. Colvin, and A.P. Alivisatos, *X-ray Photoelectron Spectroscopy of CdSe Nanocrystals with Applications to Studies of the Nanocrystal Surface.* The Journal of Physical Chemistry, 1994. **98**(15): p. 4109-4117.

129. Mazzio, K.A., et al., *A one pot organic/CdSe nanoparticle hybrid material synthesis with in situ [small pi]-conjugated ligand functionalization.* Chemical Communications, 2013. **49**(13): p. 1321-1323.

130. Takagahara, T. and K. Takeda, *Theory of the quantum confinement effect on excitons in quantum dots of indirect-gap materials.* Physical Review B, 1992. **46**(23): p. 15578-15581.

131. Chamarro, M., et al., *Enhancement of electron-hole exchange interaction in CdSe nanocrystals: A quantum confinement effect.* Physical Review B, 1996. **53**(3): p. 1336-1342.

132. Meulenberg, R.W., et al., *Determination of the exciton binding energy in CdSe quantum dots.* ACS nano, 2009. **3**(2): p. 325-330.

133. Pokrant, S. and K.B. Whaley, *Tight-binding studies of surface effects on electronic structure of CdSe nanocrystals: the role of organic ligands, surface reconstruction, and inorganic capping shells.* The European Physical Journal D - Atomic, Molecular, Optical and Plasma Physics, 1999. **6**(2): p. 255-267.

134. Albero, J., et al., *Interfacial charge transfer dynamics in CdSe/dipole molecules coated quantum dot polymer blends.* Physical Chemistry Chemical Physics, 2010. **12**(40): p. 13047-13051.

135. Taylor, J., T. Kippeny, and S.J. Rosenthal, *Surface Stoichiometry of CdSe Nanocrystals Determined by Rutherford Backscattering Spectroscopy.* Journal Of Cluster Science, 2001. **12**(4): p. 571-582.

APPENDICES

Appendix A: Copyright Permission to Use Published Paper for Chapter 3